UNIVERSITY OF CALIFORNIA
RIVERSIDE

Characterization and Design of Ignition and Energy Release Pathways in Energetic Nanocomposites

A Dissertation submitted in partial satisfaction
of the requirements for the degree of

Doctor of Philosophy

in

Materials Science and Engineering

by

Zaira Alibay

March 2022

Dissertation Committee:
Dr. Michael R. Zachariah, Chairperson
Dr. Alexander A. Balandin
Dr. Reza Abbaschian

The Dissertation of Zaira Alibay is approved:

_____

_____

_____

Committee Chairperson

University of California, Riverside

Acknowledgements

I want to thank my advisor, Professor Zachariah, for giving me the opportunity to perform cutting edge research under his supervision. I am grateful for the gained experience, confidence and knowledge under his guidance. I would also like to thank Professor Alexander A. Balandin and Professor Reza Abbaschian for serving on my dissertation committee. The work presented in this dissertation was in part collective effort and there are several individuals I was fortunate to collaborate with during my studies. First and foremost, it is the present and former members of the Zachariah Group. I'd like to thank Dr. Dylan J. Kline, who helped me integrate into the lab, Dr. Miles Rehwoldt, Dr. Kevin Yang, Dr. Lucas Algrim, Dr. Haiyang Wang, Pankaj Ghildiyal, Feiyu Xu, Prithwish Biswas, Yujie Wang, Erik Hagen, Keren Shi, Kimberly Uhls, Mahbub Chowdhury, Mohammad Ilani. I thank all my collaborators which include Dr. Min Zhou, Daniel H. Olsen from Georgia Institute of Technology, Dr. Steven S. Son and Dr. Metin Ornek from Purdue University, and Dr. Timothy H. Weihs, Dr. Shane Q. Arlington, Dr. Kerri-lee Chintersingh from John Hopkins University.

I am grateful to Dr. Mikhaylo Balinskyy and Dr. Igor Barsukov, whose expert knowledge, and enthusiasm guided me in the right directions, while exploring microwave antenna engineering.

This research efforts have been funded by Defense Threat Reduction Agency and Airforce Office of Scientific Research as part of the Multidisciplinary University Research Initiative

(MURI) program on piezoenergetic materials. I am grateful for support from the Winston Chung Global Energy Center for usage of the OPTRIS PI160 Infrared Camera. This work has appeared in previously published articles and has been reprinted with permission from Chemical Engineering Journal (Copyright Elsevier), ACS Applied Nano Materials (Copyright American Chemical Society) and Combustion and Flame (Copyright Elsevier).

I had the pleasure of meeting and growing with a lot of individuals during my time at UCR. This list includes Dr. Elaine D. Haberer, Dr. Tam-Triet Ngo-Duc, Dr. Joshua M. Plank, Dr. Joseph Cheeney, Dr. Fariborz Kargar, Dr. Ruben Salgado, Dr. Ece Coleman, Dr. Sahar Naghibi, Dr. Tammy Huang, Zahra Barani, Luz Cruz, Morgan Dundon, Steven Herrera and Stephen Hseih. Thank you for all your support, my friends.

A special thanks to a person who opened the doors of science to me during my college years - Dr. Wynter J. Duncanson.

I am so grateful to my husband and my best friend Ruben for always being there and having unconditional faith in me. Words can’t describe how much you mean to me.

To my father for teaching me the importance of hard work and honesty. To my mother for exemplifying kindness and patience. To Alma, Gauhar, Muratali and Karakoz for being constant inspiration to their little sister.

ABSTRACT OF THE DISSERTATION

Characterization and Design of Ignition and Energy Release Pathways in Energetic Nanocomposites

by

Zaira Alibay

Doctor of Philosophy, Graduate Program in Materials Science and Engineering
University of California, Riverside, March 2022
Dr. Michael R. Zachariah, Chairperson

Solid propellants are a class of energetic (combustible) materials that undergo a rapid exothermic chemistry when an activation barrier is overcome. Applications for such energetic materials can be found in space exploration technologies, automobile airbags, material synthesis, ordinance and rare-earth mining. To broaden their applications and capability, various studies have been conducted to safely and controllably release their stored potential energy. These studies have mainly focused on manufacturing techniques to tailor the properties of energetic materials to release their stored potential energy in a predictable fashion. Other studies have focused on the use of electromagnetic stimulation in ultraviolet (UV), visible (vis) and near-infrared (NIR) regions to control ignition and combustion of propellants in-operando; however, the UV-NIR electromagnetic stimulation was observed to be limited to surface level absorption due to the inherent high photon attenuations of the solid propellants. In contrast to UV-NIR electromagnetic radiation,

microwave radiation has shown to display rapid, selective and volumetric heating to control and modulate energy release pathways in solid propellants.

In this work, we first explore mechanisms that control the ignition of energetic materials at microwave frequencies. High-speed color camera imaging, infrared pyrometry, temperature jump (T-jump) ignition and differential scanning colorimetry methods are used to understand the mechanisms driving ignition in 3D printed nanoscale titanium (nTi)/ polyvinylidene fluoride (PVDF) films. This work is further expanded to engineer material systems with controllable ignition under stimulation at 2.45 GHz, where manganese oxide (MnO_x) was studied as an oxidizing microwave agent. Beyond research on microwave ignition, the effect of microwave heating during in-operando combustion of reactive materials is investigated. First, heat transfer mechanisms influencing the combustion of energetic materials were experimentally studied via microscope imaging and pyrometry tools. Subsequently, infrared thermometry and color ratio pyrometry were employed to study microwave heating rate, flame front and propagation velocity of gasless Al-Zr-C composites. The research explores mechanisms that drive and impede response of solid propellants to microwave energy prior to ignition as well as throughout rapid energy release.

Table of Contents

List of Figures

List of Tables

1 Introduction

From the discovery of fire to the burning of fossil fuels, the benchmarks of human evolution and technological advancement are strongly tied to the control and mastery of combustion. Combustion is conventionally defined as the conversion of the stored chemical energy into useful energy via redox reaction between a fuel (combustible material) and an oxidant. Combustible materials are classified based on the phase of the material (gas, liquid and solid), fuel flow states (laminar and turbulent) and homogeneity of the mixture, where premixed reactants are defined as homogeneous and reactants only mixing during the combustion are stated heterogeneous [1]. This research focuses on solid energetic materials, which are a subclass of solid combustible materials that undergo rapid exothermic chemistry when an activation barrier is overcome. Applications of solid energetic materials include space exploration technologies, automobile airbags, material synthesis to ordinance and mining industries.

1.1 Introduction to Solid Energetic Materials

Solid energetic materials are classified into propellants, pyrotechnics and explosives. Explosives are distinguished from pyrotechnics and propellants by their propagation rate, where the latter two energetics combust in a deflagration regime at subsonic speeds. For explosive energetics a combustion wave propagates at supersonic rates which is accompanied by rapid pressure and a rise in temperature. De-facto characterization parameters such as combustion velocity, pressurization rate, adiabatic

flame temperature, ignition temperature and ignition delay times are used to illustrate the performance of solid energetic materials [2]. Solid energetic materials can also be categorized as homogeneous, where a fuel and an oxidizer are situated within the same molecule, or heterogenous energetics where constituents are physically integrated into a mixture. Homogeneous compounds are classically CHNO (carbon, hydrogen, nitrogen and oxygen) molecules that have reaction enthalpies restricted by the formation enthalpy of their final combustion products, CO_2 and H_2O [3]. Molecular scale mixing of a fuel and an oxidizer in monomolecular compounds minimizes losses due to diffusion and limits their reaction rate to the chemical kinetics of the compound's decomposition. Despite these advantages, energy density in monomolecular substances is inferior to the volumetric and gravimetric energies stored in metal fuels, such as Al, B, Mg and Ti. Exploitation of the stored potential energy in metals via their oxidation could open new avenues of designing more advanced solid energetic materials.

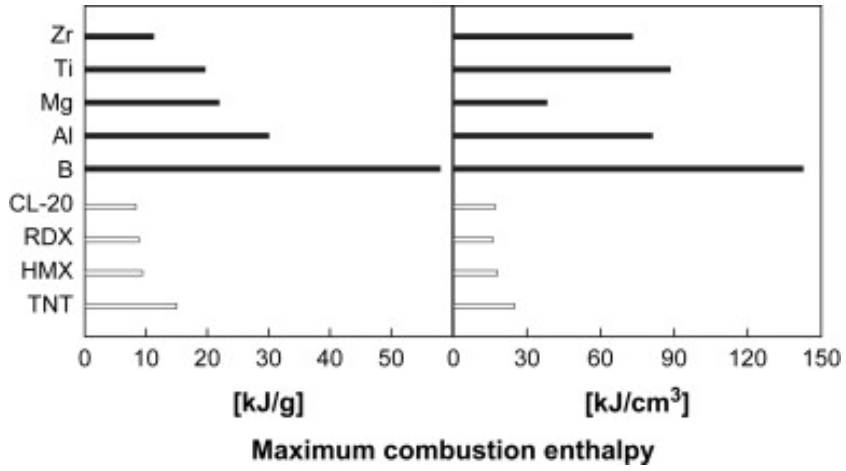

Figure 1-1. *Energy density chart of monomolecular compounds and metal fuels. Reprinted from Metal-based reactive nanomaterials, 35, Dreizin E., Page 142., Copyright (2009), with permission from Elsevier.*

A class of solid energetic materials that liberate energy via redox reaction in short timescales when an activation barrier is overcome as shown in Equation 1-1:

$$M_F + M_oO \rightarrow M_FO + M_o + \Delta H \uparrow \quad (1\text{-}1)$$

where M_F is a metal fuel, M_oO is a metal oxide and ΔH is the combustion enthalpy. Although the relationship has been traditionally defined as a reaction between metals and metal oxides such as Fe_2O_3, CuO, MoO_3, and MnO_2, it has been broadened to include non-metal-based oxidizers, such as fluoropolymers and metallic salts, that allow the formation of more stable reaction post-products [4]. Large diffusion distances between micron scale fuels and oxides in thermites (illustrated in Figure 1-2), as opposed to atomic scale diffusion of the monomolecular compounds, lead to slow reaction kinetics and high

ignition thresholds despite higher energy densities [5,6]. As a result, heterogeneous micron scale energetics had been limited in their use in propellants and pyrotechnics. One approach of decreasing the diffusion distance has focused on the reduction of fuel and oxidizer dimensions at the nanoscale. High surface area (10 – 50 m^2/g) and intimate mixing of 1-100 nm sized particles has shown increased reactivities and reduced ignition thresholds [5–7]. At the nanoscale, these particles offer the remarkable characteristic of high degree of tunability, where constituent dimensions, oxidant selection, stoichiometry, and assembly impact the resultant reactivity.

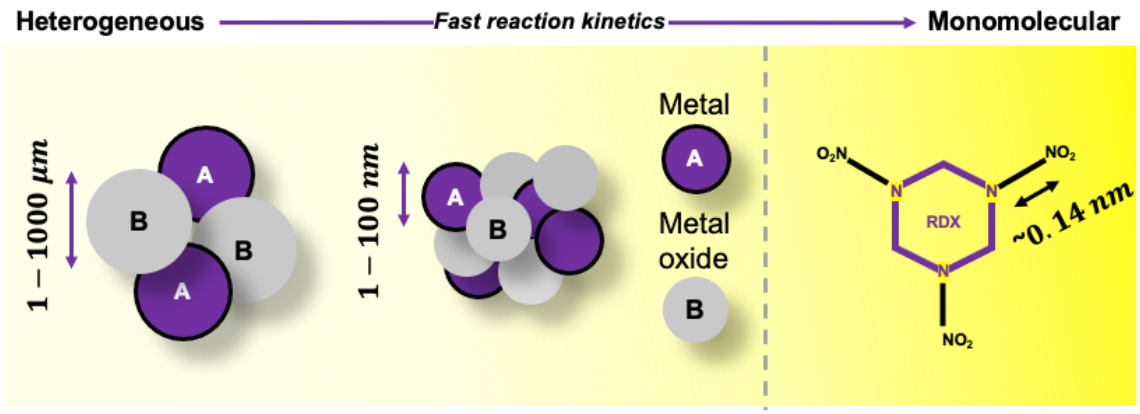

Figure 1-2. *Illustration of heterogeneous and monomolecular compounds and characteristic diffusion lengths of each material.*

1.2 Mechanisms Driving Ignition and Combustion of Nanoscale Heterogeneous Energetics

Ignition is defined as a point where heat gain due to a reaction dominates energy losses and sustained combustion is achieved. Parameters such as ignition temperature and time to ignition are ordinarily used to characterize the ignition event. The deconvolution of ignition mechanisms of nanothermites is a complex process and largely depends on the selected fuel and oxidizer behavior under elevated temperatures. Ignition and combustion mechanisms of aluminum (Al) have been extensively studied due to its abundance, relative inexpensiveness, and high energy density [3,8]. The scaling down of Al from micron to nanoscale resulted in the decrease in the ignition temperature from ~2000°C to ~660°C, respectively. Both temperatures closely correlate with melting points, where for microparticles (>100 μm) the ignition follows the melting temperature of the native oxide shell (Al_2O_3) [9,10], while the nanoscale Al (nAl,) ignition event closely followed the melting of the metal core [11,12]. The ignition of nanoscale Al (nAl) has been closely studied over decades and two main mechanisms have been offered: melt-dispersion and diffusion driven mechanism. The melt - dispersion mechanism proposes that the metal core of Al nanoparticle melts and expands leading to pressure exertion on the surrounding Al_2O_3 shell. This in turn breaches the alumina shell followed by an ejection of molten aluminum droplets and their direct oxidation with oxygen [13,14]. In the proposed diffusion driven mechanism, a number of studies have showed that before the metal core melts at 660°C, an Al_2O_3 shell undergoes phase transition, which leads to density changes in the shell and eventual exposure of the metal core [15]. Subsequently, the outward diffusion of Al ions

through the available pores and the inward diffusion of oxygen anions triggers the ignition of the metal fuel [16]. It is important to note that the minimum threshold of ignition in nAl has been established to be restricted by the diffusion rate of aluminum cations. Primary oxidation mechanisms under ambient conditions change with a choice of metal fuels and their respective thermophysical properties. As such for nano titanium (nTi) with a melting temperature of its metal core at 1668ºC, the oxidation is driven by a short-circuit diffusion of oxygen anions via a native oxide shell (TiO_2) that also undergoes crystallization in a temperature range of 240–350°C [17,18]. Aside from the selection of the metal fuel, the choice of the oxidizing agent can dramatically influence the ignition process in nanothermites [19]. Oxidizers are nominally categorized based on their phase: gas generating versus condensed phase. For condensed phase oxidizers such as Bi_2O_3 and perovskites, the reactive oxygen partaking in the reaction is from oxygen atoms bound to the lattice sites of the metal oxide. In Bi_2O_3 high oxygen ion mobility [20,21] and a high oxygen release temperature of 1300ºC results in condensed phase dominated reaction. As a result, an increase in O_2 pressure does not influence the ignition temperature of nAl/Bi_2O_3 thermites [19]. However, in gas generating oxidizers like CuO and I_2O_5 the release of gaseous oxygen closely follows the ignition event and a decrease in the O_2 pressure is followed by higher ignition thresholds [22]. Interestingly, the critical reaction rate for nAl oxidation is constant independent of the oxidizer selection and the time to ignition. The ignition temperatures for different nAl/metal oxide systems are simply a reflection of required alignment to achieve the characteristic critical reaction rate of nAl [19].

1.3 Outstanding Challenges in Solid Propellant Design

The primary function of a propellant is to provide a forward force that moves a load via conversion of stored potential energy to kinetic energy. Chemical propulsion systems either function via liquid or solid phase propulsion fuels. Liquid phase rocket propellants face difficulties due to elevated storage risks associated with high flammability and sensitivity to ambient conditions [23]. In response to these risks, more complicated rocket motor designs are required that incorporate cooling systems to avoid overheating and extra pumps and valves to allow mixing of the fuel and oxidizer to handle and store these fuels onboard rockets. The difficulties presented by liquid phase fuels lead to search for alternative designs which utilized solid propellants that possessed the following advantages: a) a modest design of the rocket stemming since the fuel and oxidizer are in the premixed state and b) a higher flammability threshold which allowed for an extended storage stability and safety from unintended ignition [24]. Nonetheless, there are still outstanding challenges associated with solid propellant design such as: a) an inability to throttle as the propellant combusts at constant rate, b) a failure to pause/restart as once ignited the solid propellant is consumed to completion and c) a low specific impulse compared to liquid fuels. Although these limitations impede the implementation of the solid propellants in high-precision orbit insertion applications, the advantages and simplicity allow active use of solid propellants in the rocket boosters, where throttling inability can be neglected without compromising the function of the propellant.

1.4 Advancements and Approaches to Design of Solid Energetic Materials

Various avenues have been explored to address the modulation behavior of solid propellants such as implementing pintles and switching to hybrid fuel systems and laser assisted augmentation. Pintle nozzles work by modifying the chamber pressure via alterations to the exit nozzle's cross-sectional area [25,26]. The change in chamber pressure leads to the modulation of the propagation rate as explained by Equation 1-2 [27]:

$$\dot{r} = aP_c^n \tag{1-2}$$

where $\dot{r}$ is the propagation rate, a is a propellant's propagation rate coefficient, n is the burn rate exponent and P_c^n is the chamber pressure in the motor. The decrease in chamber pressure via retraction of the pintle from the chamber throat will decrease the propagation rate of the propellant, while the insertion of the pintle into the nozzle will increase the chamber pressure and lead to the acceleration of the burn rate. Despite the theoretical feasibility of this approach, the design complexity and addition of extra mechanical weight due to operation of the pintles precludes their implementation as solid propulsion. Alternatively, hybrid fuels provide a middle ground between traditional liquid fuels and solid propellants, where a solid fuel combusts via a diffusion flame with an injected liquid or gaseous phase oxidizer [28]. The throttling of the propellant is achieved through regulation of the oxidizer injection rate, when turned off or on allows pause and restart of the motor. However, the same approach limits the output burn rate of the propellant, as the

higher propagation rates can only be achieved by the addition of the oxidizer injection ports via an increase of the surface area available for combustion [24,28–30]. In the scenario of laser-controlled propulsion systems, the throttling in the motor was modulated via variation in the applied laser intensity, where on demand start/pause of solid propellants was achieved with ammonium perchlorate (AP)/hydroxyl terminated poly butadiene (HTPB) propellants [31]. Additionally, carbon black was added to the solid propellants to increase their sensitivity to applied laser powers [31–33]. These findings were largely explored in a near-infrared and infrared wavelength region, where solid energetic materials experience large photon attenuations leading to mainly surface absorption [10–12]. One could explore a microwave region to bypass the shallow transmission effects, where strategically placed microwave sensitizers within the volume of the material could facilitate dynamic modulation of thrust in solid energetic materials.

1.5 Microwave Radiation Overview

Microwave energy is a non-ionizing radiation source mostly characterized in the wavelength range from 0.001 to 1 m, corresponding to a 1.24 μeV - 1.24 meV energy domain. Complex dielectric permittivity ε and complex magnetic permeability μ properties intrinsic to materials at specified frequencies and temperatures dictate their behavior under microwave stimulation as demonstrated in Equations 1-3 and 1-4 [34].

$$\varepsilon = \varepsilon' - j\varepsilon'' \quad (1\text{-}3)$$

$$\mu = \mu' - j\mu'' \quad (1\text{-}4)$$

A material's polarization and absorption ability in response to the incident electric field is described by the dielectric constant (ε'), where a null value represents a highly reflective material and high ε' values characterize microwave absorptive materials. While the dielectric loss factor (ε'') describes the ability of absorbed energy to dissipate as heat due to the electric field component electromagnetic wave. Both parameters vary with temperature and incident frequency, where metals at elevated temperatures tend to possess lower microwave absorption rates. The ratio of the dielectric constant to dielectric loss factor is a loss tangent ($\tan\theta = \frac{\varepsilon'}{\varepsilon''}$) and reveals the influence of both complex permittivity values. For non-magnetic materials, complex dielectric values (ε' and ε'') are critical in the deconvolution of a material's microwave susceptibility. For magnetic materials, the real part of the magnetic permeability explains the extent of magnetization, while the imaginary part of the permeability depicts the degree of dissipation of the stored energy [35]. Most solid energetic materials of interest are non-magnetic in nature, thus complex dielectric permittivity parameters are of greater importance when considering their microwave susceptibility.

Metals have been mostly regarded as microwave reflectors due to a narrow skin depth that limits penetration of the incident waves into the conductor's volume. Additionally, as the metal size reduces below the skin depth, one must also consider the microwave susceptibility of a naturally forming passivating shell of a reactive metal core as it

influences the sensitivity of the material to microwave energy. Biswas et al demonstrated that a thin microwave absorbing passivating layer can increase metal nanoparticles' absorption rate by 5 orders of magnitude as compared to bare metal nanoparticles [36].

1.6 Modulation of Ignition and Combustion via Microwave Energy

Following the discovery of the influence of the native passivating shell, nanoscale Al and Ti were studied for microwave ignition with a localized microwave source due to their dielectric properties on microwave absorptivity. The findings showed that nTi can be ignited under microwave stimulation, whereas nAl is insensitive to applied microwave energies after minutes of irradiation [37]. In the case of nAl, both the metal core and the dielectric Al_2O3 shell are impervious to incident microwave energies and no heating occurs []. However, it has been demonstrated that the addition of microwave susceptors to nAl based thermites could lead to ignition under microwave stimulation. Aluminum (37 μm particles) based thermite with Fe_3O_4 was ignited under localized microwave source with a peak electric field intensity of 2 MV/m [38], where the magnetic field absorption of the magnetite before Curie temperature and electric field heating above Curie temperature lead to thermal runaway and an ignition event. The incorporation of rGO (reduced graphene oxide) at 30 wt.% in nAl/Fe_2O_3 thermites demonstrated that the time to ignition under microwave stimulation can be reduced from 4.34 s to 0.43 s, where without susceptor incorporation nAl/Fe_2O_3 thermites did not show consistent ignition [39]. For monomolecular energetics, the addition of carbon nanotubes and graphene flakes increased the heating under microwave stimulation in otherwise insensitive HMX (High melting

nitroamine explosive) and TNT (Trinitrotoluene) pellets [40,41], although the heating was not sufficient to induce ignition, where 40 seconds irradiation led to melting of TNT under [41]. Despite the enhanced microwave susceptibility of energetic materials with the addition of sensitizers, the occupied parasitic volume reduced the energetic performance of these materials [42]. Sippel et al also studied the effect of electromagnetic stimulation at 2.46 GHz on combusting energetic materials where an application of microwave energy showed an enhancement in the propagation rate of the Al/AP, AP/HTPB and Al/AP/$NaNO_3$ solid propellants via several pathways such as the ionization of gaseous species and heating of the condensed phase products [43]. These initial findings could be further explored to understand the mechanisms driving ignition in energetic composites via microwave energy.

1.7 Dissertation Research Objectives

The studies undertaken in this dissertation look to build upon the knowledge of some of the prior works mentioned in this introductory section and explore new avenues to broaden our understanding of fundamental processes which may have been overlooked or not well studied. Rapid, selective and volumetric heating capabilities of microwave radiation offer opportunities to control and modulate energy release pathways in solid propellants via electromagnetic stimulation at microwave frequencies. The following goals have been set to advance the established objective:

- Explore the governing mechanisms behind microwave ignition of solid energetic materials. Effects such as reaction kinetics, applied microwave intensity,

microwave susceptor absorptivity and heat losses were studied via T-jump ignition, infrared thermometry, high-speed color camera imaging and modeling. Based on the findings, our goal is to engineer material systems with controllable ignition under microwave irradiation at 2.45 GHz.

- Design and engineer instrumentation for ignition and combustion augmentation studies under electromagnetic stimulation at 2.45 GHz which are suitable for solid energetic material applications.
- Study the effect of microwave heating on augmentation of combustion in energetic materials. Understand the effects of microwave heating on flame front, propagation velocity and reaction behavior of solid energetic materials.

1.8 References

[1] K.W. Ragland, K.M. Bryden, Combustion Engineering, 2nd ed., Taylor & Francis Group, 2011.

[2] S. Kabra, S. Gharde, P.M. Gore, S. Jain, V.H. Khire, B. Kandasubramanian, Recent trends in nanothermites: Fabrication, characteristics and applications, Nano Express. 1 (2020) 032001. https://doi.org/10.1088/2632-959x/abbce7.

[3] E.L. Dreizin, Metal-based reactive nanomaterials, Prog. Energy Combust. Sci. 35 (2009) 141–167. https://doi.org/10.1016/j.pecs.2008.09.001.

[4] L. Wang, Z. Munir, Y. Maximov, Review of Thermite Reactions: their utilization in the synthesis and processing of materials, J. Mater. Sci. 28 (1993) 3693–3708.

[5] R.W. Armstrong, B. Baschung, D.W. Booth, M. Samirant, Enhanced propellant combustion with nanoparticles, Nano Lett. 3 (2003) 253–255. https://doi.org/10.1021/nl025905k.

[6] M.L. Pantoya, J.J. Granier, Combustion behavior of highly energetic thermites: Nano versus micron composites, Propellants, Explos. Pyrotech. 30 (2005) 53–62. https://doi.org/10.1002/prep.200400085.

[7] M.R. Weismiller, J.Y. Malchi, J.G. Lee, R.A. Yetter, T.J. Foley, Effects of fuel and oxidizer particle dimensions on the propagation of aluminum containing thermites, Proc. Combust. Inst. 33 (2011) 1989–1996. https://doi.org/10.1016/j.proci.2010.06.104.

[8] N.H. Yen, L.Y. Wang, Reactive metals in explosives, Propellants, Explos. Pyrotech. 37 (2012) 143–155. https://doi.org/10.1002/prep.200900050.

[9] A.G. Merzhanov, M. Region, Aluminum Ignition, Combust. Flame. 29 (1977) 1–14. https://doi.org/10.1016/s0886-7798(99)90022-6.

[10] Y. Huang, G.A. Risha, V. Yang, R.A. Yetter, Effect of particle size on combustion of aluminum particle dust in air, Combust. Flame. 156 (2009) 5–13. https://doi.org/10.1016/j.combustflame.2008.07.018.

[11] C.J. Bulian, T.T. Kerr, J.A. Puszynski, 31st International Pyrotechnics Seminar, in: Fort Collins, CO, 2004: p. 327.

[12] G. Jian, N.W. Piekiel, M.R. Zachariah, Time-resolved mass spectrometry of nano-Al and nano-Al/CuO thermite under rapid heating: A mechanistic study, J. Phys. Chem. C. 116 (2012) 26881–26887. https://doi.org/10.1021/jp306717m.

[13] V.I. Levitas, M.L. Pantoya, B. Dikici, Melt dispersion versus diffusive oxidation mechanism for aluminum nanoparticles: Critical experiments and controlling parameters, Appl. Phys. Lett. 92 (2008) 1–4. https://doi.org/10.1063/1.2824392.

[14] V.I. Levitas, B.W. Asay, S.F. Son, M. Pantoya, Mechanochemical mechanism for fast reaction of metastable intermolecular composites based on dispersion of liquid metal, J. Appl. Phys. 101 (2007). https://doi.org/10.1063/1.2720182.

[15] M.A. Trunov, M. Schoenitz, E.L. Dreizin, Effect of polymorphic phase transformations in alumina layer on ignition of aluminium particles, Combust. Theory Model. 10 (2006) 603–623. https://doi.org/10.1080/13647830600578506.

[16] A. Rai, K. Park, L. Zhou, M.R. Zachariah, Understanding the mechanism of aluminium nanoparticle oxidation, Combust. Theory Model. 10 (2006) 843–859. https://doi.org/10.1080/13647830600800686.

[17] N. V. Muravyev, K.A. Monogarov, A.N. Zhigach, M.L. Kuskov, I. V. Fomenkov, A.N. Pivkina, Exploring enhanced reactivity of nanosized titanium toward oxidation, Combust. Flame. 191 (2018) 109–115. https://doi.org/10.1016/j.combustflame.2018.01.011.

[18] M.C. Rehwoldt, Y. Yang, H. Wang, S. Holdren, M.R. Zachariah, Ignition of Nanoscale Titanium/Potassium Perchlorate Pyrotechnic Powder: Reaction Mechanism Study, J. Phys. Chem. C. 122 (2018) 10792–10800. https://doi.org/10.1021/acs.jpcc.8b03164.

[19] W. Zhou, J.B. DeLisio, X. Wang, G.C. Egan, M.R. Zachariah, Evaluating free vs bound oxygen on ignition of nano-aluminum based energetics leads to a critical reaction rate criterion, J. Appl. Phys. 118 (2015). https://doi.org/10.1063/1.4930889.

[20] E.D. Wachsman, S. Boyapati, M.J. Kaufman, N. Jiang, Modeling of ordered structures of phase-stabilized cubic bismuth oxides, J. Am. Ceram. Soc. 83 (2000) 1964–1968. https://doi.org/10.1111/j.1151-2916.2000.tb01498.x.

[21] R. Punn, A.M. Feteira, D.C. Sinclair, C. Greaves, Enhanced oxide ion conductivity in stabilized δ-Bi2O 3, J. Am. Chem. Soc. 128 (2006) 15386–15387. https://doi.org/10.1021/ja065961d.

[22] G. Jian, S. Chowdhury, K. Sullivan, M.R. Zachariah, Nanothermite reactions: Is gas phase oxygen generation from the oxygen carrier an essential prerequisite to ignition?, Combust. Flame. 160 (2013) 432–437. https://doi.org/10.1016/j.combustflame.2012.09.009.

[23] J. Ashish, G. Swaroop, K. Balasubramanian, Effect of Ammonium Perchlorate Particle Size on Flow, Ballistic, and Mechanical Properties of Composite Propellant,

Elsevier Inc., 2018. https://doi.org/10.1016/B978-0-12-813908-0.00008-3.

[24] L.T. De Luca, T. Shimada, V.P. Sinditskii, M. Calabro, Chemical Rocket Propulsion: A Comprehensive Survey of Energetic Materials, 2017.

[25] R. Smith-kent, H.-T. Loh, P. Chwalowski, Analytical Contouring of Pintle Nozzle Exit Cone Using Computational Fluid Dynamics, in: 31 St AIAA/ASME/SAE/ASEE Jt. Propuls. Conf. Exhib., 1995: pp. 1–13.

[26] J.H. Lee, Y.C. Kim, S.H. Park, S.J. Oh, S.T. Lim, J.Y. Oh, J.W. Won, H. Ko, A study on the performance characteristics of blunt body pintle nozzle, 49th AIAA/ASME/SAE/ASEE Jt. Propuls. Conf. 1 PartF (2013) 1–7. https://doi.org/10.2514/6.2013-4080.

[27] J. Napior, V. Garmy, Controllable Solid Propulsion for Launch Vehicle and Spacecraft Application, (2006) 1–13. https://doi.org/10.2514/6.iac-06-c4.2.04.

[28] D. Altman, Overview and History of Hybrid Rocket Propulsion, in: Fundam. Hybrid Rocket Combust. Propuls., 2007: pp. 1–36. https://doi.org/10.2514/5.9781600866876.0001.0036.

[29] O. Frota, M. Ford, Review on hybrid propellants, in: Eur. Sp. Agency, (Special Publ. ESA SP, 2004: pp. 205–214.

[30] B. Cantwell, A. Karabeyoglu, D. Altman, Recent advances in hybrid propulsion, Int. J. Energ. Mater. Chem. Propuls. 9 (2010) 305–326. https://doi.org/10.1615/IntJEnergeticMaterialsChemProp.v9.i4.20.

[31] Z. Qin, J. Wu, R.Q. Shen, Y.H. Ye, L.Z. Wu, Laser-controlled combustion of solid propellant, Adv. Mater. Res. 884–885 (2014) 87–90. https://doi.org/10.4028/www.scientific.net/AMR.884-885.87.

[32] S. Ikura, D. Haraguchi, Y. Yano, A. Kakami, Performance of a Throttleable Solid Propellant Microthruster Using Laser Heating, Trans. Japan Soc. Aeronaut. Sp. Sci. Aerosp. Technol. Japan. 19 (2021) 598–603. https://doi.org/10.2322/tastj.19.598.

[33] B. Duan, H. Zhang, L. Wu, Z. Hua, Z. Bao, N. Guo, Y. Ye, R. Shen, Controllable combustion behaviors of the laser-controlled solid propellant, Def. Technol. 18 (2022) 38–48. https://doi.org/10.1016/j.dt.2021.03.002.

[34] J. Sun, W. Wang, Q. Yue, Review on microwave-matter interaction fundamentals and efficient microwave-associated heating strategies, Materials (Basel). 9 (2016) 231. https://doi.org/10.3390/ma9040231.

[35] P.A. Mello, J.S. Barin, R.A. Guarnieri, Microwave Heating, in: Encycl. Food Saf.,

Elsevier, 2014: pp. 59–74. https://doi.org/10.1016/B978-0-12-378612-8.00410-8.

[36] P. Biswas, D.J. Kline, M. Rehwoldt, T. Wu, W. Zhao, X. Wang, M.R. Zachariah, Microwave absorption by small dielectric and semi-conductor coated metal particles, ACS Appl. Polym. Mater. 1 (2019) 982–989. https://doi.org/10.1021/acsapm.9b00016.

[37] D.J. Kline, M.C. Rehwoldt, C.J. Turner, P. Biswas, G.W. Mulholland, S.M. Mcdonnell, M.R. Zachariah, Spatially focused microwave ignition of metallized energetic materials, J. Appl. Phys. 055901 (2020). https://doi.org/10.1063/1.5134089.

[38] Y. Meir, E. Jerby, Thermite powder ignition by localized microwaves, Combust. Flame. 159 (2012) 2474–2479. https://doi.org/10.1016/j.combustflame.2012.02.015.

[39] S.J. Barkley, A.R. Lawrence, M. Zohair, O.L. Smithhisler, C.L. Pint, J.B. Michael, T.R. Sippel, Smart Electromagnetic Thermites: GO/rGO Nanoscale Thermite Composites with Thermally Switchable Microwave Ignitability, ACS Appl. Mater. Interfaces. 13 (2021) 39678–39688. https://doi.org/10.1021/acsami.1c04476.

[40] W.L. Perry, A.L. Higginbotham Duque, Micro to mesoscale temperature gradients in microwave heated energetic materials, J. Appl. Phys. 116 (2014). https://doi.org/10.1063/1.4892391.

[41] E. Vargas, M.L. Pantoya, M.A. Saed, B.L. Weeks, Advanced susceptors for microwave heating of energetic materials, Mater. Des. 90 (2016) 47–53. https://doi.org/10.1016/j.matdes.2015.10.110.

[42] C.A. Crane, M.L. Pantoya, B.L. Weeks, Investigating the trade-offs of microwave susceptors in energetic composites: Microwave heating versus combustion performance, J. Appl. Phys. 115 (2014). https://doi.org/10.1063/1.4868337.

[43] S.J. Barkley, K. Zhu, J.E. Lynch, J.B. Michael, T.R. Sippel, Microwave plasma enhancement of multiphase flames: On-demand control of solid propellant burning rate, Combust. Flame. 199 (2019) 14–23. https://doi.org/10.1016/j.combustflame.2018.10.007.

2 Diagnostics and Instrumentation

This chapter covers the major fabrication and characterization tools used to investigate the mechanisms governing ignition and combustion in microwave stimulated solid propellants. Temperature measurements prior to ignition were acquired via high-speed infrared thermometry. Parameters such as time to ignition and temperature profiles during in-operando combustion were characterized with high-speed color camera imaging tools. Microwave stimulation was achieved via localized microwave source at low and high applied powers and a microwave cavity design. Detailed explanation of calibration and power signal measurement for all instrumentation is described below.

2.1 Combustion Diagnostics

2.1.1 High-Speed 2-dimensional Microscope Imaging

High-speed color cameras with microscopic (Vision Research VEO710) and macroscopic (Vision Research Miro110) imaging capabilities were used throughout this work to investigate the ignition and combustion events in nanothermite composites. Color cameras reproduce images by using a complementary metal oxide semiconductor (CMOS) imaging sensor coupled with a color filter array (CFA). The high-speed color cameras used in this research operate on a Bayer-type CFA placed on the CMOS sensor, which records the intensity of the incoming red (R), green (G) and blue (B) radiation at each corresponding pixel location on the sensor (illustrated in Figure 2-1). Since pixel positions are unique to either R or G or B channels, the intensities of two missing channels at

individual pixel locations are interpolated by averaging their neighboring values. This procedure is named demosaicing and results in the reconstruction of the recorded image in color. The generated RGB channel intensities of the incoming light can be further processed into spatial and temporal temperature data by applying thermal radiation principles.

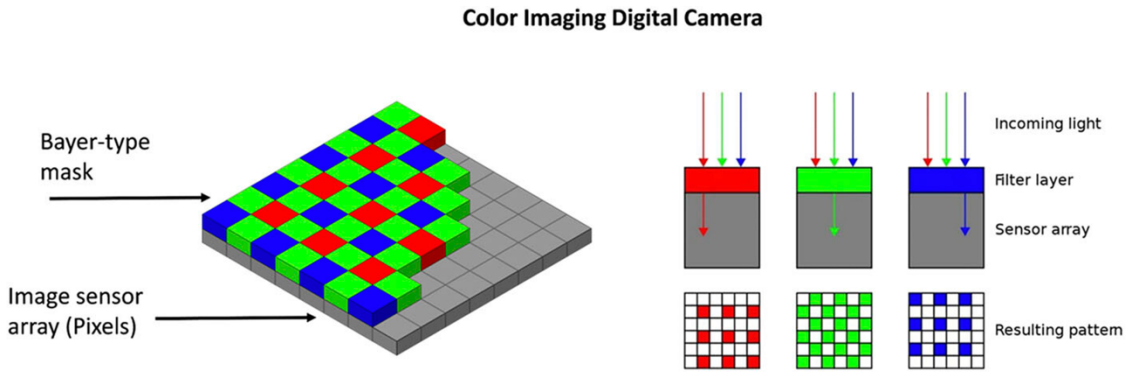

Figure 2-1. *Illustration of Bayer-type CFA placed on the CMOS sensor. Reprinted from Imaging pyrometry for most color cameras using a triple pass filter, 92, McNesby K. et al Page 063102-2, Copyright (2021), with permission from American Institute of Physics* [1].

The conversion of radiated intensities at different channel wavelengths to temperature values is based on Planck's law which states that all physical matter emits electromagnetic radiation. The expression for spectral radiance, which is the power of electromagnetic radiation normalized per unit area of the body, per unit solid angle of radiation, per unit wavelength of a body is provided in Equation 2-1.

$$r(\lambda,T) = \frac{2\pi hc^2}{\lambda^5} \cdot \frac{\epsilon(\lambda,T)}{e^{\frac{hc}{\lambda kT}-1}} \quad (2\text{-}1)$$

In the equation $r(\lambda,T)$ is the spectral radiance, λ is the radiation wavelength, ϵ is the material emissivity, h is the Planck's constant, k is the Boltzmann's constant, c is the speed of light. The color camera's response, I, to each available channel, i, can be expressed in terms of the spectral radiance [2,3]:

$$I_i = \psi_i \Delta A_d \Delta\omega_d \Delta t \int \tau(\lambda) r(\lambda,T) \chi_i(\lambda) d\lambda \quad (2\text{-}2)$$

where ψ_i is the camera gain, $\chi_i(\lambda)$ is the spectral sensitivity of the CFA, $\tau(\lambda)$ is the lens transmission, ΔA_d is the pixel area, Δt is the exposure time and $\Delta\omega_d$ is the solid angle subtended by a pixel. Theoretical values of the expected channels ratios at specified temperatures can be calculated by taking the ratio of the camera's response (I) in equation 2-2 for the different channels (i/j, where i= G,R, or B j= G,R, or B) over a desired theoretical temperature, as shown in Figure 2-2 [4,5]. Once the theoretical values are established the camera's channel intensity ratios can be measured with a standardized blackbody source. Once the theoretical values are established, the camera's channel intensity ratios can be measured with a standardized blackbody source. The ratio of the theoretical to recorded camera values can be then used to calculate the calibration ratio (C_{ij}) of the camera, as shown in the Equation 2-3 below:

$$\left(\frac{I_i}{I_j}\right)_{theoretical} = C_{ij}\left(\frac{I_i}{I_i}\right)_{camera} \quad (2\text{-}3)$$

The ratio pyrometry calculations assume a gray-body approximation, where material emissivity is independent of temperature. The temperature measurements, which are based on three color ratio pyrometry that were customized for our camera systems by previous group members, Dr. Rohit Jacob and Dr. Dylan J. Kline [5], were used in Chapter 7 of this dissertation to understand the effect of microwave heating during combustion of reactive materials. Additionally, a microscopic high-speed imaging set-up was used to experimentally observe the effect of heat transfer mechanisms on the combustion of nanothermite composites presented in Chapter 6 of this work. The allowed temperature array in our systems is 773 K – 4773 K. However, Figure 2-2 shows that the theoretical color ratios overlap in the lower temperature regions (<1000 K), resulting in measurements errors. To improve the accuracy of our measurements, a temperature processing code was designed to exclude error values higher than 110 K, thus most lower temperature regions are not included in the color camera temperature maps.

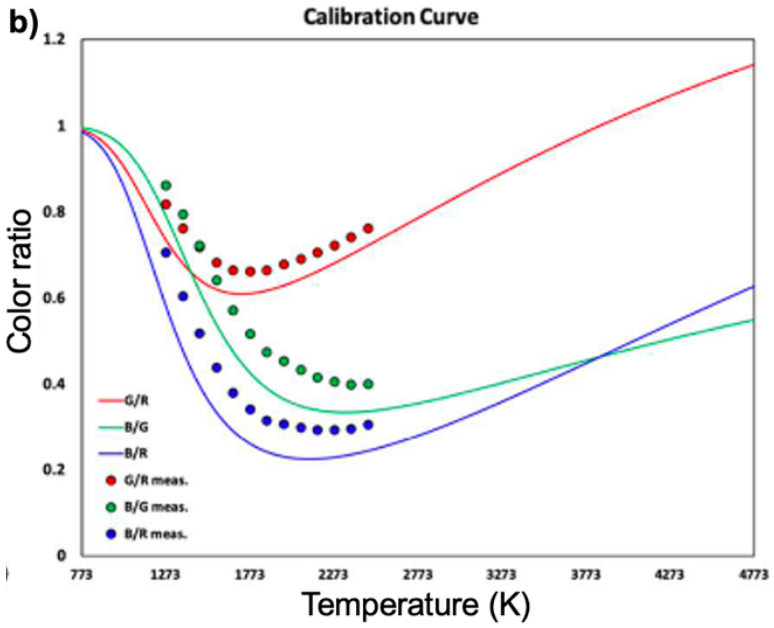

Figure 2-2. *Spectral calibration curve of VEO710 color camera* [4].

2.1.2 High-Speed Infrared Thermometry

Infrared thermometry was used to observe the heating of materials under microwave irradiation below the temperature detection range of visible wavelength cameras. Infrared energy is radiated by all matter above -273.15ºC, where conventionally the spectrum spans from 700 nm – 1000 µm with three main spectral ranges usable for thermal imaging [6,7]:

1. Long-wave infrared (LW-IR): 8 – 14 µm
2. Mid-wave infrared (Mid-IR): 3 – 5 µm
3. Short-wave infrared (SW-IR): 900 nm – 1.7 µm

For our applications, the temperature detection range of 25 - 727ºC was critical since it is not covered by color camera pyrometry and is associated with pre-ignition temperature region for energetic materials. Since heating prior to energetic materials' ignition is usually

associated with fast temperature rise rates (nominally at the order of 10^3 – 10^6 ºC/s), it was integral to have an IR camera with the capability of observing events at rates of 10,000-20,000 frames per second. Short integration times required by maximum frame rate influence the final resolution of the device. The incoming signal intensity decreases during low integration times which reduces the detector's well-filling levels. High acquisition rates and adequate resolution per pixel requirements narrowed the available infrared radiometry technologies to mid-IR operating detectors. This is due to low energy of the LW-IR radiation that limits the detectors to long integration times that allow adequate signal input to the available detector technologies. In our case, Telops Fast M3K operating in the 1.5 – 5 μm range on an InSb (indium antimonide) photovoltaic detector was selected for the measurements due to the fidelity it provides in sensitivity, resolution and acquisition rates. The camera has a pixel pitch of 30 μm, which limits the resolution with a 1X microscope objective to the pixel pitch size (see Table 2-1). In existing detector technologies with the required acquisition rates, a large pixel area was required to ensure sufficient photon collection for valid thermal measurements.

Table 2-1. *Resolution and working distance parameters of the infrared radiometer.*

Lens (30 µm pitch camera)	Minimum working distance (mm)	Field-of-view at minimum working distance (mm)	Spatial resolution per pixel at minimum working distance (µm)
50mm	500	96 x 77	300
50mm with 0.25" extender ring	260	50 x 40	156
50mm with 0.5" extender ring	190	36 x 29	114
50mm with 0.75" extender ring	155	30 x 24	93
50mm with 1" extender ring	132	25 x 20	79
1X long working distance lens	258	9.6 x 7.68	30
1X microscope objective	60	9.6 x 7.7	30
3X microscope objective	25	3.8 x 3.1	10

2.2 Material Fabrication

2.2.1 Direct-Ink Writing of Solid Propellants

Additive manufacturing of energetic materials has been widely studied to assemble solid propellants and pyrotechnics into tailored architectures with consistent packing densities. The explored techniques span from planar structures to volumetric fabrications: direct-ink writing, photopolymerization via laser stereolithogrophy and binder jet printing

as summarized by Muravyev N. V. et al in Figure 2-3 [8]. The direct-ink writing (DIW) method is notable for its simplicity, inexpensiveness. DIW requires nanothermites be suspended in a solvent based wet ink prior to printing to prevent self-ignition due to accidental impact or electric discharge. Previous studies by our group demonstrated that nanopowders of Al/CuO can be printed at high solid loadings (90 - 94 wt.%) via a direct-ink writing method [9,10]. As a result, techniques previously developed in the Zachariah group were employed to assemble materials for microwave stimulation experiments. Unlike the use of dry energetic nanopowders that inevitably lead to inconsistent material packing, prior assembly of the nanoparticles into 3D printed films allowed repeatable particle assembly that reduced variability in the tested structures under microwave stimulation. Coincidently, the high and repeatable packing density of the nanoparticles in film structures reduced the heat loss effects due to poor and variable packing observed in dry energetic materials. This is significant as heat losses to the environment were shown to inhibit the rate of heating under microwave stimulation. To assemble solid nanoparticles into consistent and easily testable structures, binder formulations with polyvinylidene fluoride (PVDF) or a mixture of hydroxypropyl methylcellulose (HPMC) and polyvinylidene fluoride (PVDF) were used. HPMC is a gelation agent that allows higher solid loading content and improves the mechanical integrity of the printed films [9], while PVDF plays a dual role in the formulations as an oxidizer and a binder. Fluorine groups present in the PVDF act as oxidizing agents during reactions with added metal nanopowders.

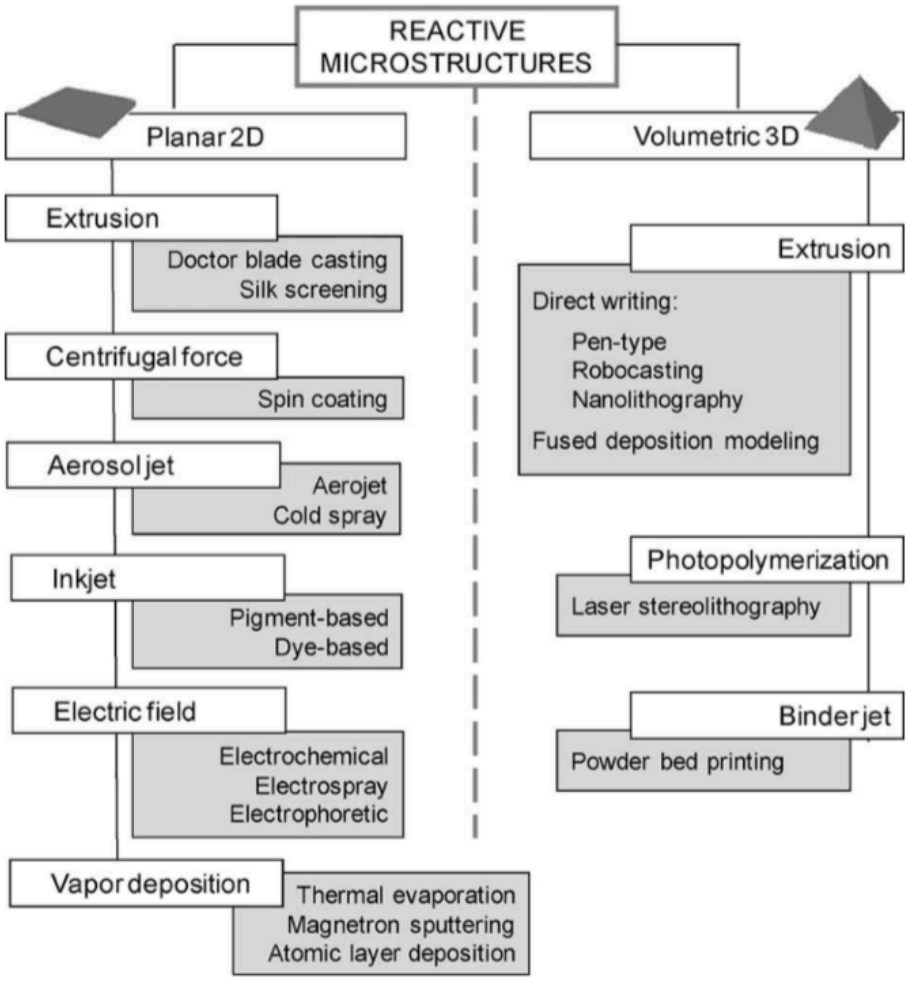

Figure 2-3. *Additive manufacturing techniques used for energetic material assembly. Reprinted from Progress in Additive Manufacturing of Energetic Materials: Creating the Reactive Microstructureswith High Potential of Applications, 35, Muravyev N. V., Page 942., Copyright (2019), with permission from Wiley VCH.*

2.3 Microwave Stimulation Tools

2.3.1 Single Frequency Microwave Cavity Design

A single frequency microwave excitation set up was designed to operate at 2.45 GHz. The microwave energy was supplied by a magnetron (MKS, TM012 MW head) that was fed by a high-power voltage supply (MKS, SM445 switching power supply) presented in the schematic in Figure 2-4. The magnetron was protected from reflected signal by a water-cooled isolator (MKS, VHU210 3kW isolator). The isolator was connected to WR-340 type triple stub-tuner (MKS, AG340M3), dual-directional coupler (MKS, DC2340N), combustion chamber and sliding short (Microwave Techniques, WR340 non-contacting sliding short assembly). A customized combustion chamber was built to stimulate energetic materials and three optical windows were installed to record the excitation process. Since the materials of interest for this research undergo rapid exothermic chemistry accompanied with gas generation, it was critical to incorporate safe gas escape routes in the microwave cavity. Therefore, a gas outlet and a gas inlet tubes were added to the combustion chamber. The gas inlet was added to allow for change in the dielectric properties of the environment in the chamber. The optical windows were built to withstand a maximum pressure exertion of 15 psig to ensure their mechanical integrity during the combustion gas release and pressure build. The detailed illustration of the combustion chamber, the sliding short, and PTFE windows are shown in the Figure 2-5. The sliding short was used to tune the standing wave inside the constructed set up to the center of the combustion chamber to enable the direct observation of materials undergoing peak microwave excitation.

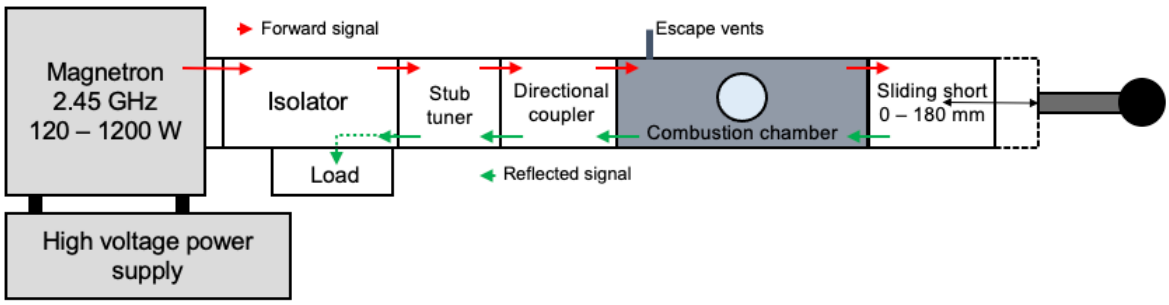

Figure 2-4. *Schematic of the single frequency high power microwave excitation set-up.*

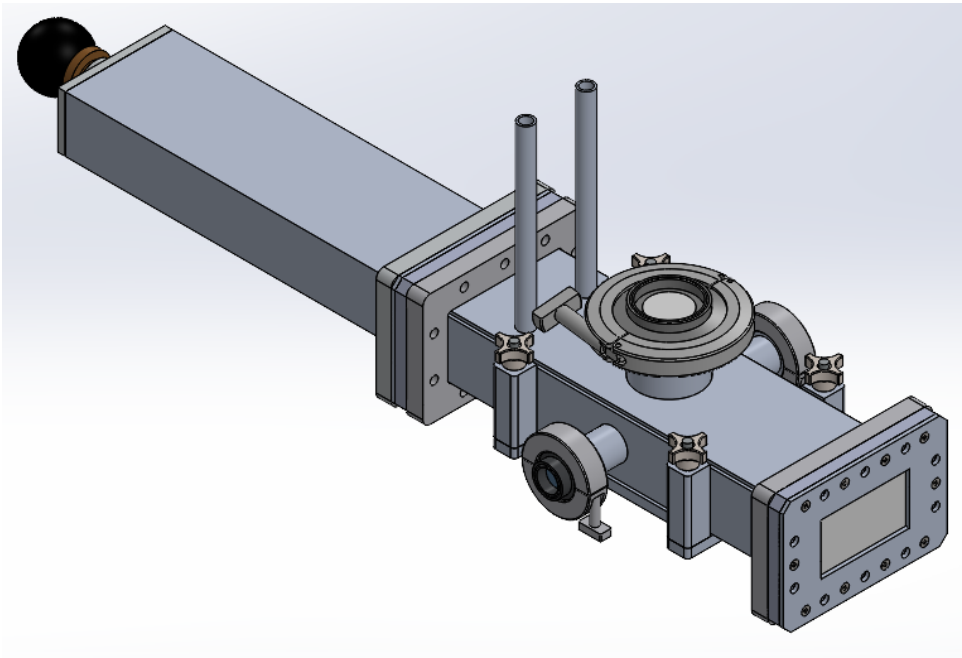

Figure 2-5. *An illustration of the designed combustion chamber terminated with the WR-340 sliding short and polytetrafluoroethylene (PTFE) protective windows.*

The standing wave in the microwave cavity assembly in Figure 2-4 was directly measured via a custom-built antenna that was placed inside the center of the combustion chamber. The antenna was made of 2% thiorated tungsten electrode of 1 mm in diameter

($D_{antenna}$) and 63 mm in length. The diameter of the antenna is significantly smaller than the free space wavelength of the operating microwave frequency $D_{antenna} << \lambda_{free}$, thus it can be assumed that the disturbance due to the present conductive probe is miniscule and standing wave pattern will be reflective of the pattern present without the probe. The flowchart of the microwave sensing is shown in Figure 2-6, where installed antenna was connected to 50 dB high-power attenuator (Fairview Microwave, SA3NFF300W-50) via a coaxial cable (Pasternack, LMR-400). To ensure safety of the spectrum analyzer three additional 10 dB attenuators (Pasternack) were connected from the main attenuator via a SMA cable. The sliding short was moved at 5 mm increments through full (180 mm) length of the part.

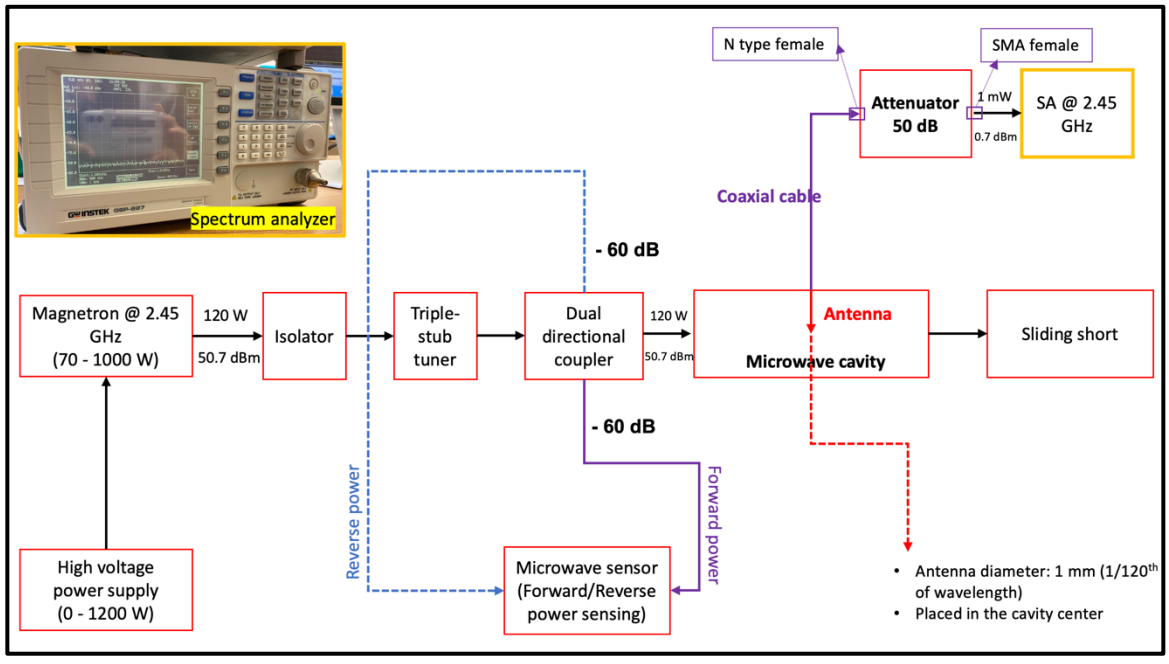

Figure 2-6. *Flowchart of the standing wave sensing inside the microwave cavity/combustion chamber.*

To ensure repeatability and accuracy, the measurements of the output signal were recorded in increasing and receding order: 0:5:180 mm to 180:-5:0 mm and repeated in triplicate. Since the optical windows in the combustion chamber are in the center of the cavity, the samples under test needed to be elevated from the bottom plate of the chamber via supporting stage. Design requirements for the stage had to incorporate two major factors: easy cleanup after combustion of the materials and insensitivity to microwave stimulation at 2.45 GHz. With these two factors in mind, alumina (Al_2O_3) was selected as a support material for the tested samples. All output signals were measured in an empty cavity as well as in the combustion chamber with Al_2O_3 support stage to test if the placement of the alumina support influences the standing wave profile in the single frequency high power microwave excitation set-up. The waveguide wavelength is defined in Equation 2-4 as follows:

$$\lambda_{waveguide} = \frac{\lambda_{free}}{\sqrt{1-(\frac{\lambda_{free}}{\lambda_{cutoff}})^2}} \quad (2\text{-}4)$$

where $\lambda_{\text{waveguide}}$ is a waveguide wavelength, λ_{free} is free space wavelength at the excitation frequency and λ_{cutoff} is the cutoff wavelength at minimum frequency of waveguide's operation. Operating frequency range for WR-340 waveguides is 2.2 – 3.3 GHz, which corresponds to the maximum operational wavelength of $\lambda_{\text{cutoff}} = 17.28\ cm$. The operating frequency of the magnetron is tailored to 2.45 GHz equivalent of λ_{free} = 12.24 cm. Inserting the values into the above equation the waveguide wavelength was

calculated to be 17.76 cm. The standing wave, $D_{standing}$, is defined as half of the waveguide wavelength which should yield 8.67 cm in the WR340 cavity at 2.45 GHz as presented in the Equation 2-5:

$$D_{standing} = \frac{\lambda_{waveguide}}{2} \tag{2-5}$$

The standard calculations aligned well with the values measured with the spectrum analyzer. The standing wave in the empty combustion chamber was 8.6 cm as presented in Figure 2-7 below. Interestingly, the profile of the wave is asymmetric as the peak values are achieved rapidly while the antinode is gradually reached as the signal output decreases. This might be specific to the imperfect cavity design where the placement of the optical viewing windows and the gas escape outlets amend the overall wave profile in the cavity. Nonetheless, the results allowed us to directly measure the profile in the chamber and design experiments in the peak intensity regions.

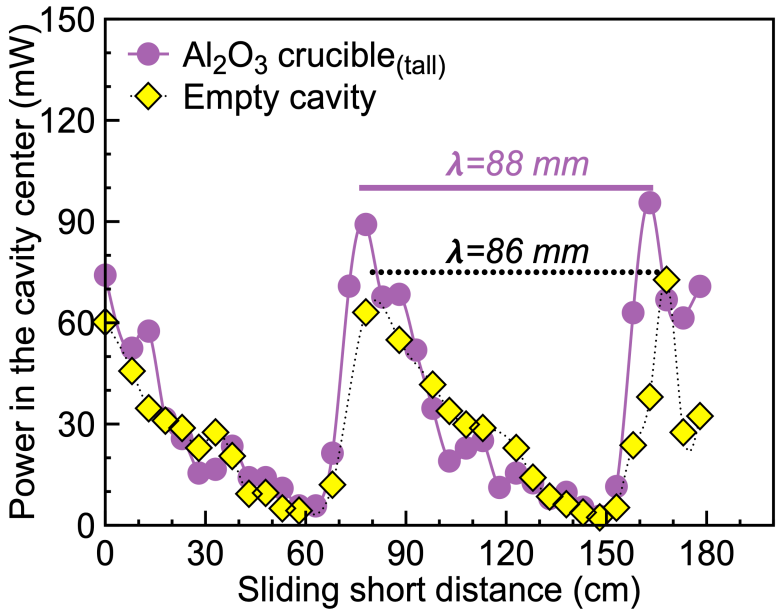

Figure 2-7. *Standing wave profile measured in the center of the combustion chamber via monopole antenna sensing probe.*

2.3.2 High-Power Monopole Antenna Design

A single frequency microwave design was reconfigured to a high-power monopole antenna set-up to observe localized heating effects under microwave stimulation. Briefly, a magnetron (MKS, MW head TM012) fed by a high-voltage supply (MKS, SM445 switching power supply) was connected in-series to a WR-340 type isolator (MKS, VHU210 3kW isolator), triple-stub tuner (MKS, AG340M3), dual-directional coupler (MKS, DC2340N) and WR340 cavity to coaxial cable transition adapter (Microwave Techniques), as illustrated in Figure 2-8. Both the magnetron and isolator were protected by water-cooling systems (OMTECH, CW 3kW) to avoid overheating during operation. The WR340 to coaxial transition is comprised of an aluminum probe placed inside the

cavity terminated with a coaxial insertion adapter with a voltage standing wave ratio (VSWR) of 1.25:1. Although the reflection losses (<5%) of the insertion adapter are marginal, the efficiency of the aluminum probe, which received the incoming signal from the magnetron, was not specified by the manufacturer and had to be experimentally measured. The coaxial insertion adapter from the WR340 transition was connected to a coaxial cable (Pasternack, LMR 400) with a soldered termination connected in series to a monopole antenna.

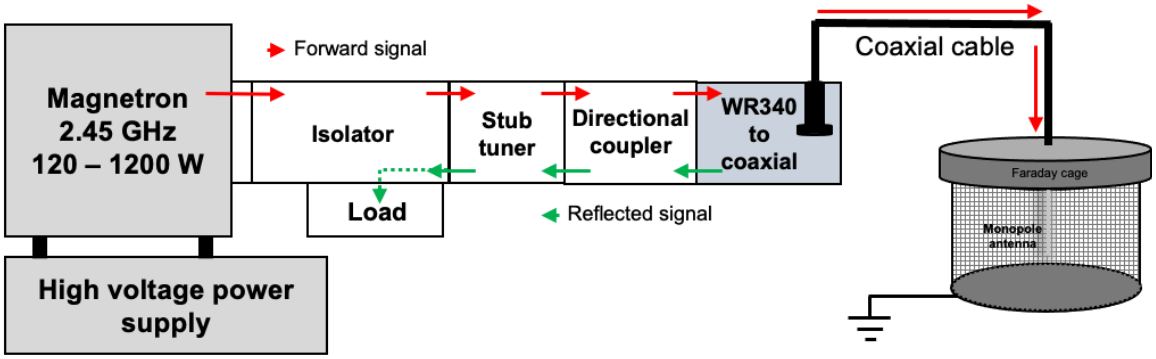

Figure 2-8. *Schematics of the high-power monopole antenna set-up.*

The antenna was made of a 2% thiorated tungsten (2% Th-W) electrode which was 1 mm in diameter and 20 ± 0.3 mm in length. The electrode was inserted onto a custom-made brass piece of 10 mm in height which connected the antenna to the coaxial cable. The total antenna piece length was 30 ± 0.3 mm. To focus the output signal to a narrower region, the ground was directly extended from the outer conductor of the coaxial cable to the aluminum metal plate at the bottom of the antenna tip, as illustrated in Figure 2-9. A Faraday cage was built around the monopole antenna to contain the incidental leakage of

the microwave energy to the environment. The microwave intensity outside of the faraday cage was measured when varying the magnetron power from 12 – 20%. The results showed that the microwave intensity at 2 feet away from the faraday cage dropped to 0.5 – 0.12 mW/cm^2, which is below the allowable limit of 10 mW/cm^2 for non-ionizing radiation sources established by Occupational Safety and Health Administration (OSHA). Although the signal intensity within a 2 feet distance from the cage increases with an increase in applied power (a 200 W input magnetron power yielded a 46 mW/cm^2 microwave intensity), the signal output continuously dropped to below the minimum allowable threshold intensity at 2 feet away from the cage. As a precautionary measure, 5 feet was always maintained away from the Faraday cage while operating the instrument.

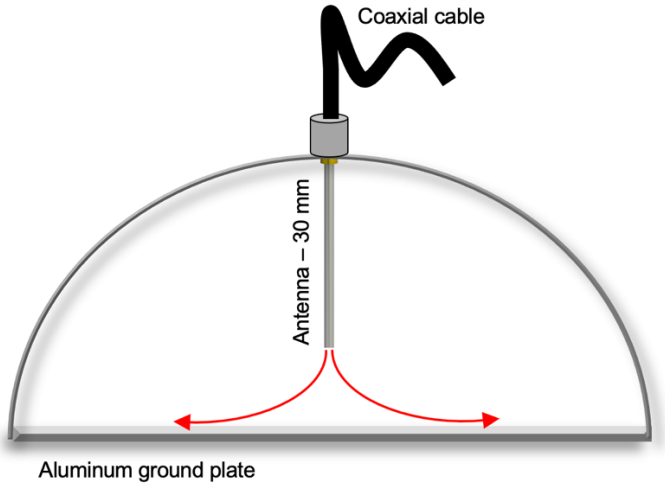

Figure 2-9. *Illustration of the monopole antenna.*

To gauge the efficiency of the WR340 transition component, a spectrum analyzer was used to measure the exact power delivered from the magnetron to the monopole antenna. Thereafter, a monopole antenna was replaced with a 50 dB attenuator (Fairview

Microwave, SA3NFF300W-50) at the coaxial cable's end, which was connected to a coaxial to SMA adapter (Fairview Microwave, SM4217), as illustrated in Figure 2-10. The SMA adapter, operating in frequency ranges of 1- 18 GHz, was connected to three in-series 10 dB attenuators. The total attenuation of the input signal to the spectrum analyzer was fixed at 80 dB. The signals from magnetron input power, ranging from 70 – 400 W, were recorded in triplicate with the spectrum analyzer operating in the frequency span from 2.2 – 2.7 GHz, where the signal consistently showed a peak around 2.45 ± 0.01 GHz. The signal intensity increased as the output frequency span decreased, displaying a narrow signal output as the power input increased.

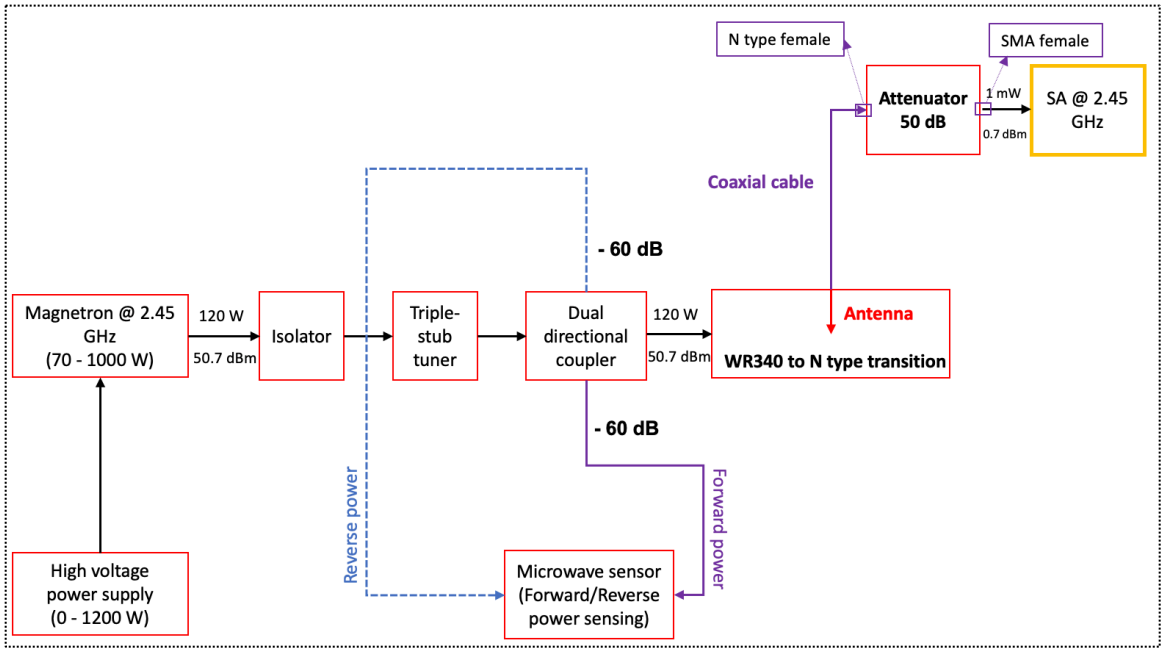

Figure 2-10. *Flowchart of the microwave power output sensing via spectrum analyzer from the monopole antenna configuration.*

The signal showed a linear increase with applied power where the conversion from WR-340 to coaxial adapter revealed a 90X decrease in the output signal as presented in Figure 2-11. The low conversion rate seems typical of WR340 to coaxial transition component.

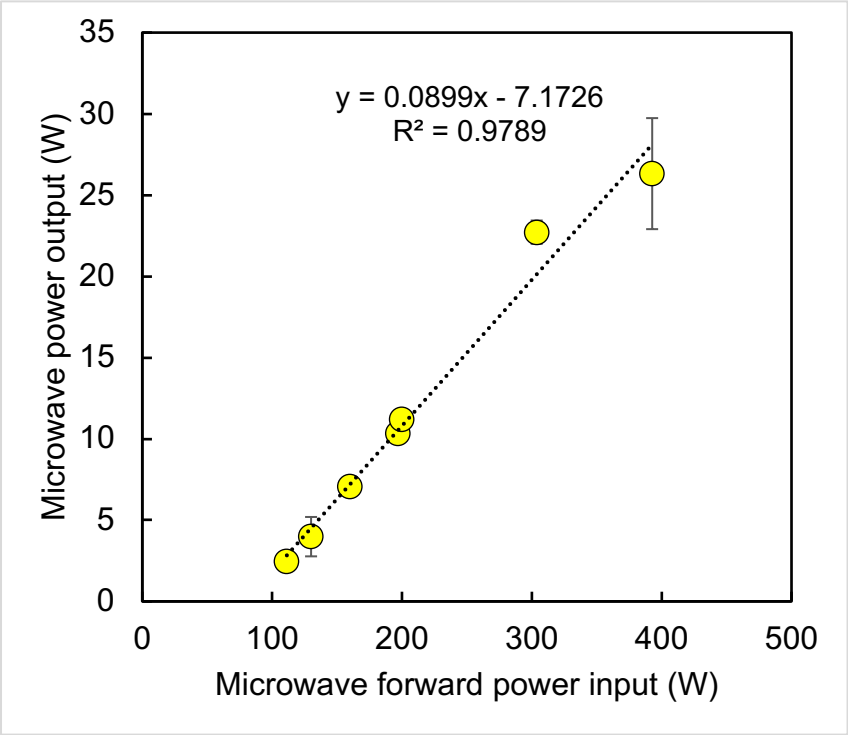

Figure 2-11. *Power output from WR340 transition to the monopole antenna as a function of the forward signal output.*

2.3.3 Localized Monopole Antenna

Before the design of the high-power output monopole antenna was used, a design a near field low-power microwave device was employed to test the microwave sensitivity of materials under 2.45 GHz radiation. The described set-up was designed by Dr. Dylan J. Kline, Dr. Miles Rehwoldt and Dr. Charles Turner and is described in detail elsewhere

[11]. A solid-state 2.45 GHz microwave signal generator (DS Instruments SG12000) was connected in series to a solid-state power amplifier (AMCOM AM206545SF-3H) with a fixed gain of 32 dB as demonstrated in Figure 2-12. The signal output from the signal generator varied at 0.5 dB increments from a minimum output of 0 dB to a 10 dB maximum. The output of the amplifier was connected to a nickel – coated metal pin with a tip diameter of 150 µm (Singer 0.025 in. diameter). Despite having a performance range from 1 – 15 W, the monopole antenna's tip allowed the transfer of field intensities around ~10^5 V/m on measured samples placed in the immediate vicinity of the tip [11–13].

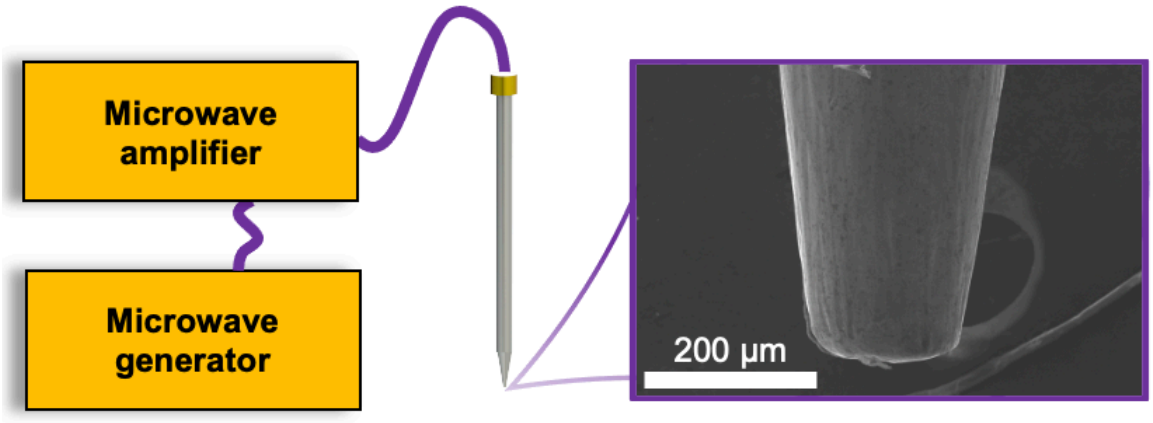

Figure 2-12. *Illustration of the low power localized monopole antenna with the scanning electron microscope inset of the antenna tip.*

2.4 References

[1] J.M. McNesby, Kevin L.; Dean, S.W.; Benjamin, R.; Grant, J.; Anderson, J.; Densmore, Imaging pyrometry for most color cameras, Rev. Sci. Instrum. (2021) In Press.

[2] J.M. Densmore, M.M. Biss, K.L. McNesby, B.E. Homan, High-speed digital color imaging pyrometry, Appl. Opt. 50 (2011) 2659–2665. https://doi.org/10.1364/AO.50.002659.

[3] H. Guo, J.A. Castillo, P.B. Sunderland, Imaging measurements of soot temperature and volume fraction in flames, 8th US Natl. Combust. Meet. 2013. 2 (2013) 1125–1132.

[4] D.J. Kline, Z. Alibay, M.C. Rehwoldt, A. Idrogo-Lam, S.G. Hamilton, P. Biswas, F. Xu, M.R. Zachariah, Experimental observation of the heat transfer mechanisms that drive propagation in additively manufactured energetic materials, Combust. Flame. 215 (2020) 417–424. https://doi.org/10.1016/j.combustflame.2020.01.020.

[5] R.J. Jacob, D.J. Kline, M.R. Zachariah, High speed 2-dimensional temperature measurements of nanothermite composites: Probing thermal vs. Gas generation effects, J. Appl. Phys. 123 (2018). https://doi.org/10.1063/1.5021890.

[6] J.D. Vincent, Fundamentals of Infrared and Visible Detector Operation and Testing, 2012.

[7] M. Vollmer, K.-P. Mollmann, Infrared thermal imaging, Second, Wiley-VCH, 2018.

[8] N. V. Muravyev, K.A. Monogarov, U. Schaller, I. V. Fomenkov, A.N. Pivkina, Progress in Additive Manufacturing of Energetic Materials: Creating the Reactive Microstructures with High Potential of Applications, Propellants, Explos. Pyrotech. 44 (2019) 941–969. https://doi.org/10.1002/prep.201900060.

[9] H. Wang, J. Shen, D.J. Kline, N. Eckman, N.R. Agrawal, T. Wu, P. Wang, M.R. Zachariah, Direct Writing of a 90 wt% Particle Loading Nanothermite, Adv. Mater. 31 (2019) 1–7. https://doi.org/10.1002/adma.201806575.

[10] H. Wang, P. Biswas, D.J. Kline, M.R. Zachariah, Flame stand-off effects on propagation of 3D printed 94 wt% nanosized pyrolants loading composites, Chem. Eng. J. 434 (2022) 134487. https://doi.org/10.1016/j.cej.2021.134487.

[11] D.J. Kline, M.C. Rehwoldt, C.J. Turner, P. Biswas, G.W. Mulholland, S.M. Mcdonnell, M.R. Zachariah, Spatially focused microwave ignition of metallized energetic materials, J. Appl. Phys. 055901 (2020). https://doi.org/10.1063/1.5134089.

[12] E. Jerby, V. Dikhtyar, The microwave drill, Science. 298 (2002) 587–589.

[13] E. Jerby, Y. Meir, A. Salzberg, E. Aharoni, A. Levy, J.P. Torralba, B. Cavallini, Incremental metal-powder solidification by localized microwave-heating and its potential for additive manufacturing, Addit. Manuf. 6 (2015) 53–66. https://doi.org/10.1016/j.addma.2015.03.002.

3 Mechanism of Microwave-Initiated Ignition of Sensitized Energetic Nanocomposites[⊥]

3.1 Summary

One of the challenges in propellant formulation is the inability to moderate the burn rate dynamically. Here, we consider spatially localized remote ignition of additively manufactured composites via microwave absorption. Previous studies demonstrated that a passivating shell on Ti nanoparticles (nTi) enhances microwave absorption. Incorporated within a polyvinylidene fluoride (PVDF) matrix, Ti/PVDF films ignite under microwave irradiation in air. To gain more comprehensive insight into pre-ignition behavior, the ignition delay was studied as a function of applied power and the microwave susceptor loading. Infrared (IR) camera studies were further used to investigate the heating behavior of the films under variable power. We found that ignition delay decreases with increasing power to an apparent heating saturation region, where the ignition sensitivity is limited by the combustion reaction kinetics. Thermogravimetric analysis coupled with differential scanning calorimetry (TGA-DSC) showed that nTi oxidizes with O_2 at lower temperatures than fluorination with PVDF and drives combustion. Findings in this work build a pathway for remote and controlled ignition of solid propellants via microwave radiation.

[⊥]The findings presented in this chapter have been previously published and are reprinted with permission from: Alibay, Zaira*, Dylan J. Kline*, Miles C. Rehwoldt, Prithwish Biswas, Steven Herrera, Haiyang Wang, and Michael R. Zachariah. "Mechanism of microwave-initiated ignition of sensitized energetic nanocomposites." Chemical Engineering Journal 415 (2021): 128657. Copyright 2021 Elsevier. *Co-first authors.

3.2 Introduction

An ongoing challenge in the tailoring of energetic materials is enabling the ability to modulate energy release rates. One way that this can be accomplished is by using additively manufactured graded materials [1–4] which enable electromagnetic radiation to locally stimulate materials to moderate burn rate or initiate reactions at specified locations or times. Infrared, visible (400-700 nm), and ultraviolet (UV, 10-400 nm) wavelength light sources are readily available and considerable effort has been expended on exploring these wavelengths (e.g. laser ignition) [5–9]. However, most energetic materials have a large photon attenuation coefficient at these energies, making the propellants primarily surface absorbers and therefore difficult to excite over the full volume [10–12]. Unlike surface stimulation of the bulk materials, microwave heating offers the potential to trigger energy release within the propellant spatially and temporally, thus enabling the in-operando spatially selective control of the throttling of solid propellants. In large part, the opportunities rely on the fact that dielectric properties at longer wavelengths can vary greatly and offer considerable fidelity in tuning ignition.

Microwave radiation is often regarded to range over 4 orders of magnitude from 0.3 – 300 GHz, with wavelengths between 1 m to 1 mm, respectively, and include millimeter waves with frequencies from 30 – 300 GHz. Electromagnetic heating of materials in microwave frequencies has been extensively utilized for synthesis of ceramics and porous structures [13–16]. The rapid, selective, and volumetric heating capabilities of microwaves offer unique advantages over conventional thermal heating methods for efficient energy release, thus prompting studies on the microwave ignition of organic

explosives [17–19]. However, ignition of metal fuels typically used in solid propellants and thermites under microwave stimuli has found limited applications due to poor absorption capabilities of bulk metals [20–23].

The poor coupling between microwaves and metal particles can be attributed to the poor penetration of the microwaves beyond the skin depth of the material, leading to reflection loss of the incident wave [24]. The skin depth, nominally a few microns for conductive particles (at 2.45 GHz), leads primarily to surface heating. As the metal particle size decreases below the associated skin depth, microwaves couple more effectively into the volume of conducting media [25]. In the case of very conductive, sub-micron particles that are not significantly smaller than the skin depth, oscillations in the associated magnetic field are more effective for microwave heating, even for non-magnetic materials [24,26,27]. Generally, reactive metal particle fuels possess a native oxide shell. We have recently explored the role of the oxide shell for a core-shell structure and have found that certain characteristic dielectric coatings around the metal core can significantly enhance the absorption behavior under microwave irradiation [28]. Recent studies in our group have shown that titanium nanoparticles (nTi), in particular, can be ignited under microwave irradiation at 2.45 GHz [29]. This was attributed to enhanced bulk microwave absorption due to a unique shell composition of amorphous TiO_2 and crystalline TiN [30].

This work expands on previous efforts to investigate the ignition of Ti/PVDF in air under microwave irradiation. Ignition delay time measurements as a function of radiation intensity were used to reveal two major regimes dictating the start of combustion under microwaves. Heating rate studies with an IR camera, as well as thermal transport

simulations via finite element analysis, distinguish heating rate limited regimes from a reaction kinetics governed region.

3.3 Materials and Methods

3.3.1 Materials and Sample Preparation

Titanium (Ti) nanopowder (30 – 50 nm) and titanium nitride (TiN) nanopowder (70 nm) were purchased from US Research Nanomaterials, Inc. Titanium nitride (TiN) was employed as a reference material for thermochemical analysis of the oxidation reaction. Thermogravimetric analysis (TGA) showed that Ti nanopowder has an active content of ~70 wt.% [30]. The Ti nanoparticles have a ~4 - 6 nm passivating shell according to previous transmission electron microscopy (TEM) [30]. X-ray diffraction (XRD) and x-ray photoelectron spectroscopy (XPS) demonstrated that the shell is comprised of ~20% TiN, TiON and ~80% amorphous TiO_2 [30]. Poly(vinylidene fluoride) powder (PVDF) (molecular weight = 534,000) was obtained from Sigma Aldrich (Millipore Sigma) and N,N-dimethylformamide (DMF 99.8%) solvent was obtained from BDH chemicals. All chemicals were used as received.

The precursor ink for printing was prepared by first dissolving PVDF in DMF at 70 mg/ml concentration. Ti nanopowder was added to the polymer solution to final concentrations of 50 wt.% and 65 wt.% of metal fuel and briefly vortexed (Vortex Genie, Scientific Instruments). The samples were then sonicated for 35 minutes (Branson), and mixed for 5 minutes at 2000 rpm in a centrifugal planetary mixer (Thinky USA). The sonication was repeated for 35 minutes before the ink was loaded into the printer.

3.3.2 Film Fabrication

Energetic films were additively manufactured with a pressure-driven extrusion printer (Hyrel System 30M) using a previously reported procedure [29]. Briefly, the prepared inks were loaded in a 30 ml syringe (Beckman Coleman) and printed with an 18-gauge blunt Luer-lock needle (McMaster-Carr). Printed films were ~40 µm thick and were printed as 8 cm x 8 cm squares that were later cut into 5 mm x 5 mm samples for ignition delay and heating rate experiments [29]. Scanning electron microscope images of the 65 wt. % Ti loading film are included in Figure 3-8.

Top surfaces of Ti/PVDF film were characterized using Scanning Electron Microscopy (SEM) (FEI NNS450-FEG). Prior to analysis the films were sputter coated (Cressington A108) with Pt/Pd for 90 seconds.

3.3.3 Microwave Emitter Configuration

The spatially localized microwave apparatus has been described elsewhere in detail and is only briefly discussed here [31]. Figure 3-9 shows the schematic of the microwave ignition system which includes a solid-state microwave generator (DS Instruments SG12000) generating a continuous wave signal at 2.45 GHz with a peak gain of 10 dBm that is controllable in 0.1 dBm increments. This signal is then amplified using a solid-state power amplifier that has a peak gain of 32 dB at 2.45 GHz, bringing the peak power output to 42 dBm (~15 W). This signal is output through a coaxial cable terminated with a nickel-plated straight pin (Singer 0.025” diameter, 18 $\pm$ 1 mm length) soldered into a solder cup

coaxial adapter. Sample microwave exposure in this apparatus is in the near field of the electromagnetic field since the working distance from the sample to the emitter is much smaller than the operating wavelength. To control distance with the microwave needle, samples are fixed to a glass slide with tape and a micrometer-precision translational stage is used to place the needle normal to the surface of the sample without penetrating the sample itself.

3.3.4 Microwave Absorption Modeling

Mie scattering theory has been used to compute the absorption efficiency (Q_{abs}) of the core-shell Ti nanoparticles following the same procedure as described in previous works by our group [28,29]. Q_{abs} is a function of the wavelength (λ) and the particle size parameter ($y = \frac{2\pi r}{\lambda}$), where r is the particle radius and r_c is the core radius and the Mie coefficients a_n and b_n as given by Equation 3-1.

$$Q_{abs} = \frac{2}{y^2}\sum_{n=1}^{\infty}(2n+1)Re(a_n + b_n) - \frac{2}{y^2}\sum_{n=1}^{\infty}(2n+1)(|a_n|^2 + |b_n|^2) \quad (3\text{-}1)$$

The Mie coefficients a_n *and* b_n are functions of the refractive indices of the core (m_1) and the shell (m_2), the core size parameter ($x = \frac{2\pi r_c}{\lambda}$) and the particle size parameter y (see Equation 3-5) [32]. For non-magnetic particles, the refractive index can be calculated as $m = \sqrt{\varepsilon_r}$ where ε_r is the complex permittivity of the material. The complex permittivity of the metallic Ti core (ε_1) is obtained from the conductivity of Ti (2.38×10^6 Sm^{-1}) using

the Drude model, $\varepsilon_1 = \frac{i\sigma}{\omega\varepsilon_0}$ [32]. The Ti shell consists of 80 % TiO_2 and 20 % TiN by volume as discussed in our previous paper [29] and used here for the complex permittivity (ε_2) by volume averaging the complex permittivity of TiO_2 ($33.01 + 10.36i$) and TiN ($15 + 4.2i$). Additionally, we considered absorption properties in the mid-IR wavelength of 10.6 μm (CO_2 Laser) with the following dielectric properties of TiO_2 ($1.23 + 0.33i$) and TiN ($-75 + 100i$) [33,34]. The Mie coefficients a_n and b_n, have been computed from the BHMIE subroutine, using the parameters mentioned above as the input [32]. BHMIE subroutine using the Wiscombe convergence criterion relating the number of Mie coefficient terms (n) to the size parameter (y) as $n \leq y + 4y^{0.3333} + 2$ is used to compute absorption efficiency. With a particle size of 50 nm ($y = 1.2 \times 10^{-6}$), n=2, hence, in the small particle limit, 2 terms are sufficient for convergence. Comparatively, six Mie coefficients are required for mid-IR frequencies in the full convergence of the Q_{abs} calculation.

3.3.5 Heating Rate and Ignition Delay Measurements

An OPTRIS PI160 infrared (IR) camera was used to measure surface temperature at 120 frames/s during microwave irradiation. The camera was set to a temperature range of 20 – 275°C per the calibration range of the device. The heating rates were calculated as slopes of the temperature vs. time curves. The pixel pitch of the camera detector is 25 μm, situated 20 mm away from the sample. The acquired maximum temperatures under the microwave irradiation are the averages over the 67.5 μm area.

A high-speed camera (Phantom Miro M110) was used to capture the ignition delay such that the camera was triggered simultaneously with the power supply. The ignition delay experiments were run in triplicate at each power setting at 5,000 frames/s for applied power between 1 – 3 W and at 10,000 frames/s for applied power between 7.5 – 15 W. The ignition delay was measured to be the time of first light. The camera has a resolution of 20 μm/pixel using a macro lens, so the measured ignition delay time is limited to a 20 μm spatial resolution of the camera set-up.

3.3.6 Thermal Simulations

COMSOL Multiphysics 4.3 was used to model both transient heating of a single particle and a film containing an ensemble of particles. For determination of the power absorbed by a single Ti nanoparticle, a unit cell of PVDF cube with a single Ti sphere inside was built. The dimensions of the unit cell were calculated using the surface-to-surface distance (d_{ss}) between the particles in the bulk film. For a specified volume fraction of Ti nanoparticles, d_{ss} of 16 nm between the particles was calculated using Equation 3-2 [35].

$$d_{ss} = d\left(\xi_0\left(\frac{\pi}{6\varphi}\right)^{\frac{1}{3}} - 1\right) \tag{3-2}$$

Here, d is a matrix filler diameter of 50 nm (Ti), φ is a volume fraction of Ti nanoparticles of 42% (calculated from the given wt.% filler and polymer content) and ξ_0 is an absolute

particle spatial distribution parameter which was set to 1.21, representing the well-dispersed morphology [35]. The parameters tabulated in Table 1 were used for material properties in the model:

Table 3-1. *Thermophysical properties of the constituents.*

Item name	Density [kg m^{-3}]	Specific heat capacity [J kg^{-1} K^{-1}]	Thermal conductivity [W m^{-1} K^{-1}]
Ti	4500	520 [36]	17 [37]
PVDF	1740	1422 [38]	0.2 [39]

To simulate our experimental system, a 500 x 500 µm propellant composite with a thickness of 40 µm was placed on a glass square with 5 mm sides and a thickness of 1 mm. The volume-based averages of Ti and PVDF densities provided by the manufacturers were used to calculate the final composite's density of 2412 kg m^{-3} assuming no porosity. The thermal conductivity of the composite (0.73 W m^{-1} K^{-1}) was estimated using Nielsen-Lewis Equation 5-3 [38,40,41]. The specific heat capacity of 836 J $kg^{-1}K^{-1}$ was calculated as a mass average of the constituents specific heat capacities at constant pressure [42,43]. The built-in material properties were chosen for the glass slide with a thermal conductivity of 1.4 W m^{-1} K^{-1}, density of 2203 kg m^{-3} and specific heat capacity of 670 J kg^{-1} K^{-1}. Finite element calculations were performed under a 3D heat transfer in solids module where heat flux with free convection (horizontal upside plate) was applied on upper and side

boundaries of the film. An extremely fine physics-controlled mesh was applied for all calculations in the software settings. Since the peak irradiation energy is limited by the diameter of the applicator [29,31,44], a heat source of 75 μm radius representing the microwave applicator was assumed in the center of the film.

3.3.7 Thermal Chemistry Characterization

Interactions of the fabricated film with air, as well as interactions of Ti and the fluoropolymer at elevated temperatures, were investigated with thermogravimetry-differential scanning colorimetry (TGA-DSC) (STA 449 F1 Jupiter, NETZCSH). The samples were heated at a rate of 10 K min^{-1} from 25°C - 1000°C in air and under an argon flow rate of 70 mL min^{-1}. Masses of 1-3 mg were loaded per TGA-DSC run.

Powder X-ray diffraction (XRD, PANalytical Empyrean Series 2) was employed to analyze combustion post-products of 65 wt.% Ti/PVDF samples using a step size of 0.013° (2θ).

3.4 Results and Discussion

3.4.1 Microwave Absorption by nTi

Figure 3-1 illustrates the microwave initiation system where a Ti/PVDF film is placed under the microwave concentrator and allowed to heat and reach the ignition point. nTi is employed as both a fuel and microwave (MW) sensitizer [29]. The pre-ignition conversion of microwave to thermal energy in nTi relies on the nanoparticle's core and

shell properties: permittivity (ε), magnetic permeability (μ), and electrical conductivity (σ) at an incident frequency (f). As mentioned previously, Ti nanoparticles have a 4-6 nm dielectric shell of TiN and TiO_2 around the conductive core which alters the absorption efficiency of the bare particles [29,30].

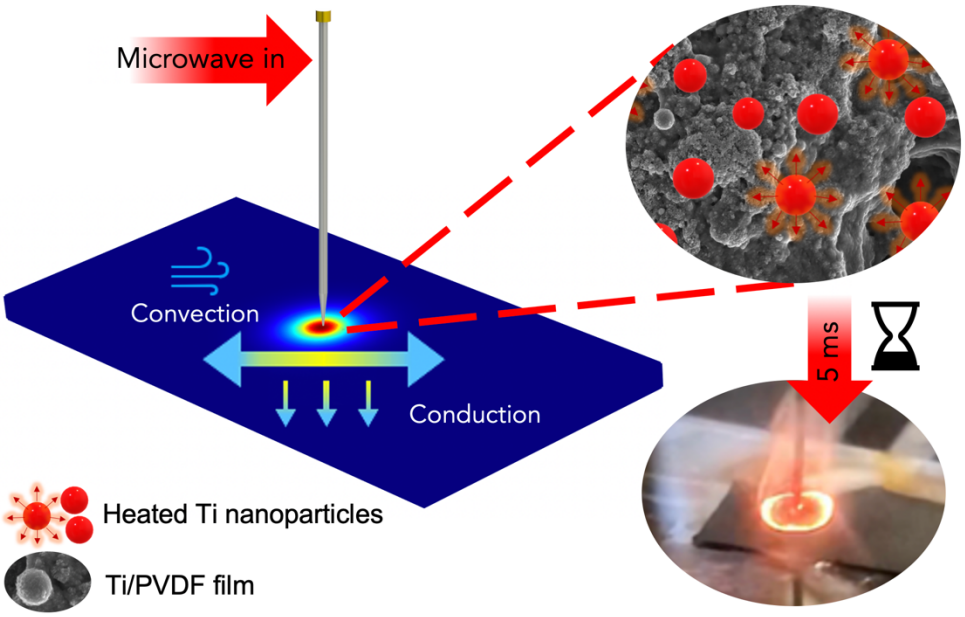

Figure 3-1. *Microwave initiation system: the microwave concentrator is placed above the sample and transfers microwave energy to Ti/PVDF film, heating nTi and leading to ignition.*

We employ Mie scattering theory to compute the absorption efficiency, Q_{abs}, of 50 nm core-shell Ti following the procedure as described previously [28]. The absorption efficiency is a dimensionless parameter that represents the area of energy that has been absorbed by a single particle relative to the particle's cross-sectional area projected onto a plane perpendicular to the incident electromagnetic wave [32]. Figure 3-2 shows that the

efficiency of microwave absorption increases sharply with increase in the dielectric shell thickness until it reaches a saturation region at 20% of the particle diameter. Bare Ti particles have Q_{abs} ~10^{-12}, which is 10,000 times smaller than the case where the same particle has a ~5 nm (10% of the core) dielectric coating. The power absorbed W_{abs} (W) by a single spherical particle is directly proportional to Q_{abs} by Equation 3-3 where I_0 is the incident intensity (W m^{-2}) and A is the particle's cross-sectional area [32].

$$W_{abs} = Q_{abs} I_0 A \tag{3-3}$$

Scattered radiation is negligible for nanoscale particles and secondary absorption effects can be ignored [28]. Thus, for the purposes of analysis, we may assume that all particles have uniform absorption and therefore the absorption power density scales with the particle volume fraction.

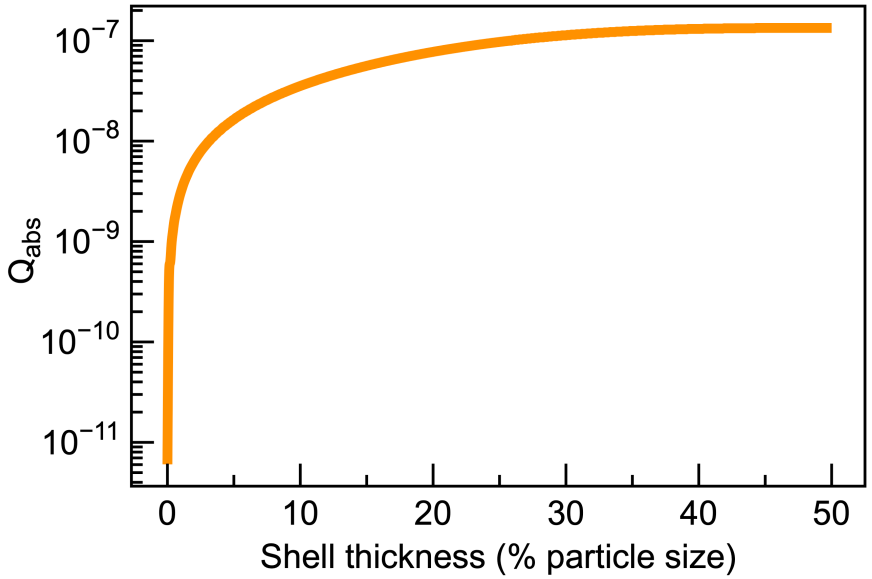

Figure 3-2. *Calculated microwave absorption efficiency of 50 nm nTi with a dielectric coating of variable thicknesses.*

3.4.2 Ignition Delay Measurements

A previous study on the microwave ignition of metallized propellants used a fixed value of applied power since the primary focus was on the effectiveness of microwave heating. These results showed that composites with ≤ 35 wt.% Ti loading did not ignite under the applied microwave power, while for 50 wt.% Ti loading the ignition occurred inconsistently [29]. For a sample to ignite under the microwave irradiation, the heating must be sufficient to overcome any heat losses and still reach the reaction onset temperature. Reaching this temperature should be dependent on the incident power, concentration of microwave susceptors, absorption efficiency of nTi under the irradiation, reaction kinetics, and heat loss. Previous work with a similar microwave ignition set-up

demonstrated that maximum electric field around the microwave concentrator and the ground reaches ~100 kV/m, an order of magnitude lower value required for discharge at 1 atm in air [29]. An important consideration to highlight is that no anisotropic electrostatic discharges (ESD) were detected in any of the tested samples under high-speed camera acquisition, and thus the ESD effects were not considered in this work. However, they might be driving mechanism for ignition under higher applied field for metallized propellants [45–47]. The dependence of ignition delay times under variable incident power was studied for 50 wt.% Ti/PVDF and 65 wt.% Ti/PVDF films as shown in Figure 3-3. At 65 wt.% Ti, the ignition delay time shows an inverse dependence on applied power over a range of 1 – 4.7 W; we refer to this as the low power region. At higher incident power (7.5 – 15 W), ignition delay becomes power-independent and saturates at ~5 ms; we refer to this as the high-power regime. Similar behavior in terms of power-dependent and independent regimes can be observed for 50 wt% Ti/PVDF films as well. No ignition is observed for an input power below 3 W and the power-dependent region spans from 3 W – 7.5 W. Additionally, the ignition delay saturation is only achieved at powers higher than 7.5 W. The results show that lower microwave susceptor density results in the reduction of the power-dependent and power-independent regimes. This raises a question about the origin of power-dependent and power-independent regimes during microwave ignition.

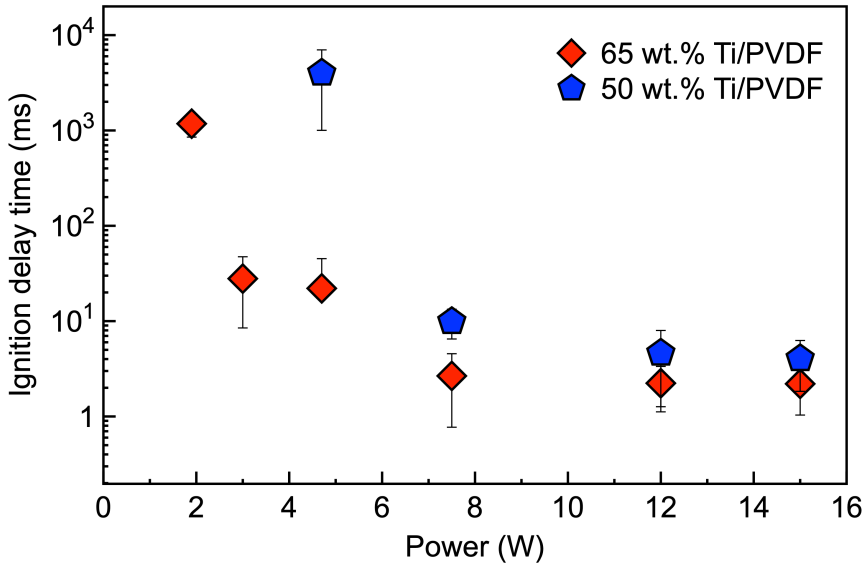

Figure 3-3. *Ignition delay dependence on applied microwave power for 50 wt% and 65 wt% nTi loading films.*

The results from Figure 3-3 can be used to estimate the absorption efficiency of nTi particles. The power absorbed, W_{abs}, by a single particle was calculated using finite element analysis. A 50 nm Ti particle was placed in a composite box and the power required to raise the temperature of a particle to the ignition temperature within 5 ms was determined. For simplicity, the ignition temperature was assumed to be the onset temperature for Ti oxidation, determined by thermogravimetric analysis to be ~470°C (see Section 3.4). This yields a minimum power required to heat Ti nanoparticle from room temperature to the ignition temperature to be ~0.16 nW over 5 ms of observed delay times in Figure 3-3. This is indicative of the minimum power absorbed by a single nanoparticle prior to ignition onset. The peak irradiation power is limited by the diameter of the microwave concentrator as described elsewhere [29,44,48,49]. To calculate the

experimental absorption efficiency per nanoparticle ($Q_{abs,e}$), we can use Equation 3-3 using the 0.16 nW power absorption and the cross-sectional area, to solve for $Q_{abs,e}$ [32]. This gives an estimated value of ~ 1.9 x 10^{-4}, which is much higher than the predicted absorption efficiencies from Mie theory calculations presented in Figure 3-2. The modeled values shown in Figure 3-2 rely on material properties as previously described and thus do not include the presence of defects in the particle's dielectric shell. Previous studies on amorphous TiO_2 and TiN have demonstrated that vacancies and other defects enhance the electromagnetic absorption of these materials in the microwave frequency range [50–52], which may explain why our particles appear to be more efficient absorbers. In either scenario, more detailed studies on the microwave properties of components in the shell should be performed and are reserved for future studies.

3.4.3 Heating Rate and Its Role in Ignition Delay

We now turn our attention to assessing the possible origins of the two power regimes in ignition delay. To probe the two ignition delay regimes, we conduct temporal thermal imaging with an IR camera under microwave irradiation at various power levels. Figure 3-4a shows the temporal temperature at different applied power for a 65 wt.% Ti/PVDF film. Between 7.5-15 W applied power, there is a rapid linear increase in temperature which strains the temporal resolution of camera (8.3 ms). At these high-power regimes where ignition takes place within ~5 ms (see Figure 3-4b), the heating rates represent minimum estimations, as calculated from the IR camera measurement, and range between ~4000°C/s - 6000°C/s.

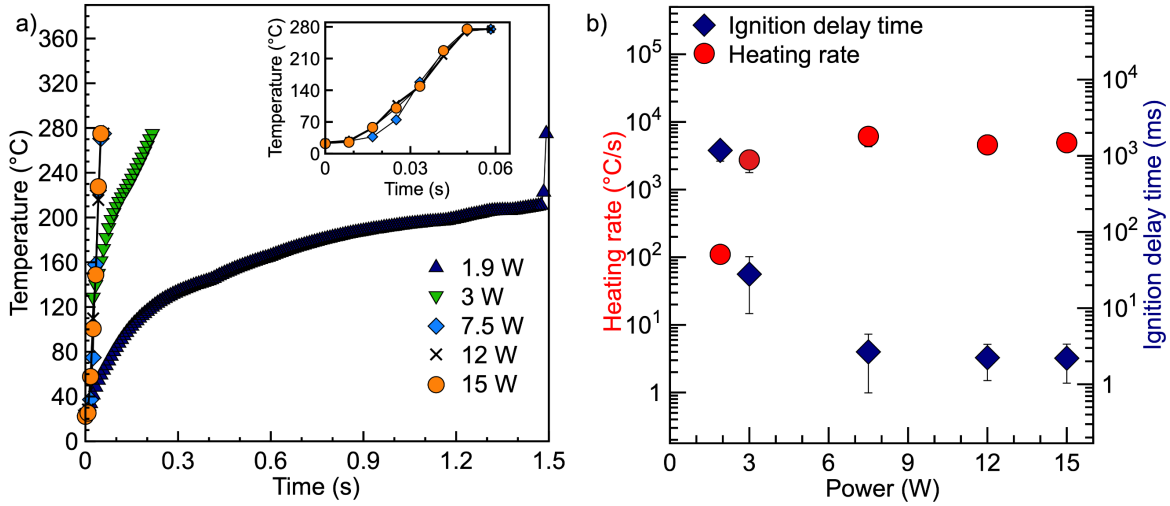

Figure 3-4. *(a) IR imaging temperature vs. time for 65 wt.% Ti/PVDF films at different power levels with an inset of heating profile in the high-power regime and (b) corresponding heating rate and ignition delay times vs. power.*

As seen in Figure 3-4a, high input powers lead to rapid heating rates computed in Figure 3-4b that closely match the power-independent regime observed in Figure 3-3. This power dependence is commonly seen in other ignition sources where the criterion for ignition is that heat applied by the power source and the energy released by the exothermic reaction is larger than the heat losses. Lower applied powers (≤3 W) exhibit slower temperature rises as seen in Figure 3-4a. The slow rise in temperature correlates with the longer ignition delay times in the power-dependent region (Figure 3-4b). This implies that the heating rate dictates the ignition delay times under microwave irradiation for Ti/PVDF composites in the low-power regime. Considering that the ignition delay is effectively power-independent above ~7.5W, there is a second rate-limiting step controlling ignition

at high powers. To investigate whether the heating rate reaches a plateau region in the high applied power regime due to the increased heat losses, a transient heating simulation was performed.

We simulated the spatiotemporal temperature distribution of the films under higher applied powers (≥7.5 W) using a 3-D finite element COMSOL simulation considering both thermal conduction and convection. Using the experimental value of absorption efficiency ($Q_{abs,e}$), 1.9 x 10^{-4}, peak irradiation radius of 75 μm, and varying incident powers; the temperature within the film is computed over 5 ms. The peak irradiation radius was selected based on the tip diameter of the microwave applicator utilized for the ignition delay studies. Figure 3-5a shows a schematic of the geometry, which includes radial conduction of heat away from the source to the glass slide and convective heat losses to the environment. The conductive heat losses to the glass slide results in lower temperatures within the film volume closest to the glass as compared to the surface exposed to the environment. The computed radial thermal profile at 5 ms for various applied power is shown in Figure 3-5b. The peak temperature monotonically increases with applied power, unlike the experiment which shows a plateaued temperature. The temperature profiles calculated in Figure 3-5b suggest that the temperatures of the films are able to meet or exceed the ignition temperature within 5 ms, demonstrating that the power-independent regime of the ignition delay curve in Figure 3-3 is due to some other phenomena which will be explored in the following sections. It should be noted, however, that endothermic chemistry may occur over this timespan but is not captured in this simulation.

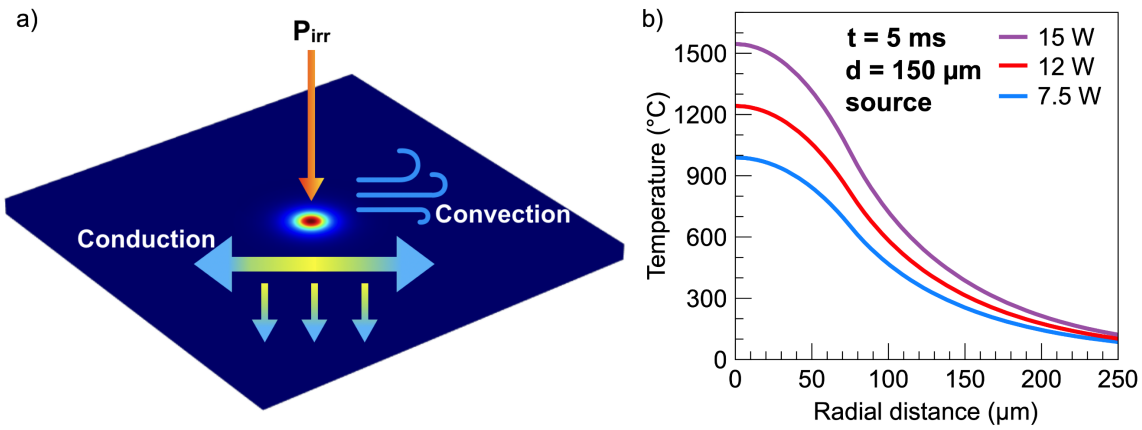

Figure 3-5. *(a) Schematic of a thermal gradient in a film with heat loss and source of 75 µm and (b) modelled radial surface temperature distribution at t=5ms.*

3.4.4 Thermo-chemical Analysis

As we have observed, the power-independent regime is likely related to something other than heating rate and may be associated with intrinsic chemical kinetics. Although the heating rate of TGA/DSC is lower than local heating rate of the samples under microwave exposure, the technique elucidates key interactions. Previous studies have shown that the decomposition temperature of neat PVDF is heating rate dependent but unaffected by environments of argon and air [53,54]. Figure 3-6a shows that PVDF in Ti/PVDF films decomposes at 440°C in argon, while the decomposition starts at ~377°C in air. The difference in the onset temperatures for Ti/PVDF in air and argon can be attributed to the earlier reaction between the Ti nanoparticles and O_2 in air, which facilitates decomposition [54]. The mass loss of ~80% in neat PVDF corresponds to the release of HF as a major product, monomer $C_2H_2F_2$ and small amounts of $C_4H_3F_3$ [55]. The remaining

mass of ~20% corresponds to non-volatile products [53,54]. However, Ti/PVDF films experience only a partial mass loss of ~15%, followed by oxidation of nTi at ~468°C in air. The latter matches the oxidation temperature of nTi with O_2, as can be seen in Figure S3.

DSC analysis of Ti/PVDF in argon shows three exotherms, where the first exotherm is concurrent with PVDF decomposition [53,56] and the second exotherm coincides with mass gain in TGA most likely corresponding to Ti fluorination (Figure 3-6b). The first decomposition exotherm does not take place until ~510°C, which is beyond nTi's oxidation temperature. This implies that, while fluorination could be a concurrent reaction throughout the course of combustion, but it is unlikely that it starts the ignition process. Additionally, TGA of TiN particles in Figure 3-11 demonstrates that the oxidation of TiN in air starts at ~440°C, which is close to Ti oxidation temperature. Since nTi's shell is an amalgam of TiO_2 and TiN, it is likely that the reaction also involves oxidation of TiN [30]. X-ray diffraction analysis was performed on post-combustion products of 65 wt.% Ti/PVDF samples, showing the presence of TiO_2 and possible Ti-O-N (Figure 3-12). The latter predicts that both the Ti core and the TiN shell might participate in the reaction with O_2 in air. Thus, the thermochemical and XRD analysis presented here implies that both the TiN shell and Ti core initially interact with O_2 and start the combustion process.

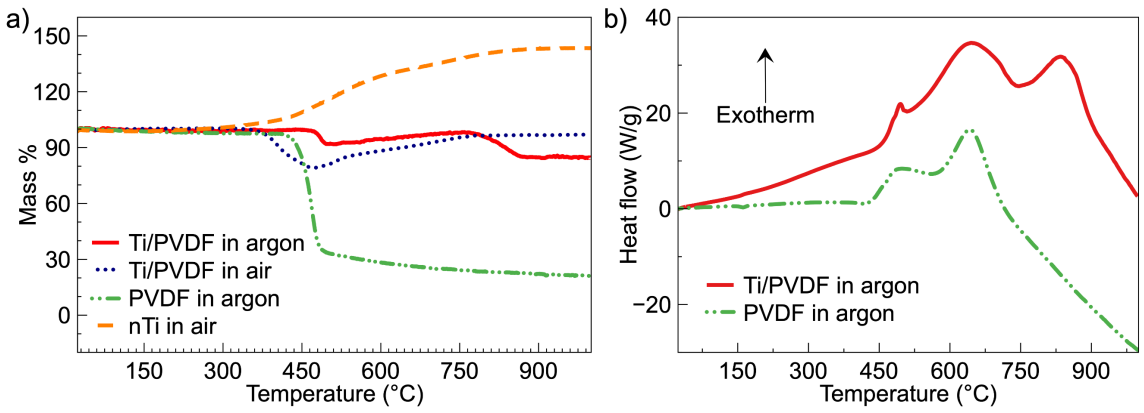

Figure 3-6. *(a) TGA analysis on PVDF in argon, nTi in air and Ti/PVDF composite in air and argon and (b) DSC of PVDF and 65 wt.% Ti/PVDF. The samples were heated at a rate of 10 K min^{-1} in air and argon at a flow rate of 70 mL min^{-1}.*

Since the oxidation of the Ti nanoparticles with air seems to be the primary reaction pathway over fluorination, the kinetics of the oxidation are of considerable importance for this system. Previous studies on oxidation kinetics of Ti have shown that Ti oxidation in air is limited by O_2 diffusion [57,58]. The passivating shell around nTi is a combination of amorphous TiO_2, TiN and TiO_xN [30]. TiO_2 constitutes majority (~90 vol.%) of that shell. Based on particle size distribution and active mass content of immobile Ti, the thickness of the passivating shell is ~ 3-4 nm. Using a diffusion coefficient (D) of O_2 through amorphous TiO_2 of ~8 x 10^{-16} m^2/s, [59] and Equation 3-4, where L is the shell thickness (characteristic length), the characteristic 1D diffusion time, t, is calculated to be 5 - 10 ms at 773K [60].

$$t = \frac{L^2}{2D} \tag{3-4}$$

Considering that the characteristic diffusion time at temperatures near the ignition threshold for Ti/PVDF are very comparable to the power-independent ignition delay shown in Figure 3-3, it is reasonable to assume that a probable limitation in this power-independent regime is actually the diffusion of oxygen through the protective shell of heated Ti particles.

3.4.5 Proposed Ignition Mechanism

As we have demonstrated, there are two input power regimes that are necessary to consider during the microwave ignition of Ti/PVDF composites – a power-dependent regime at low powers and a power-independent regime at high powers. The power-dependent regime is controlled by the rate of heat accumulation driven by absorption of the applied microwave energy to the Ti nanoparticles as confirmed by infrared pyrometry which shows that temperature increases over longer time scales. Therefore, the power-dependent regime of the ignition delay for microwave ignition of Ti/PVDF is a thermally-limited process and thus related to the optical properties of the sensitizer. In particular, the core-shell structure of the metal particle is of significant importance in this low power region [28].

At high MW power, the ignition behavior becomes independent of power, suggesting a second rate-limiting step. Thermogravimetric analysis of the samples and

post-combustion analysis of the products from the Ti/PVDF reaction demonstrate that the primary driving reaction is not necessarily the fluorination of Ti, but rather the oxidation of the active Ti nanoparticle core from O_2 available in the aerobic environment. Characteristic diffusion time analysis for O_2 through the protective TiO_2 shell suggests that the diffusion time at elevated temperatures is ~5 ms and consistent with the time scales observed for ignition delay. These results imply that the power-independent regime is limited by diffusion kinetics.

As a brief summary, the ignition delay of Ti/PVDF as induced by microwave ignition is limited by two factors: (1) heat accumulation and (2) oxygen diffusion through the shell. While O_2 diffusion is likely a limiting step for ignition in air, the microwave ignition is not dependent on O_2 provided that the propellants still ignite in argon environment [29]. For both of the regimes nTi acts as both a MW sensitizer and fuel and rapidly heats the film as shown in Figure 3-7. The polymer in the vicinity of the heated nTi undergoes partial decomposition at elevated temperatures, while O_2 diffuses through amorphous TiO_2 shell reacts with TiN and Ti core.

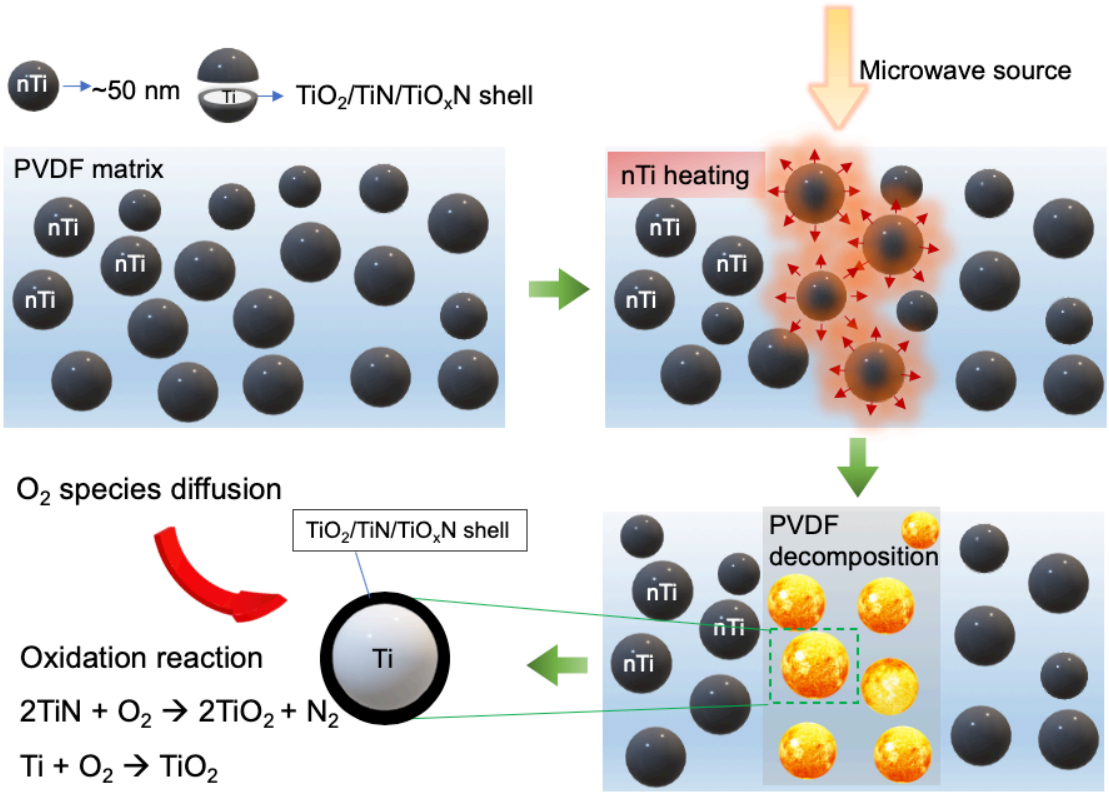

Figure 3-7. *Proposed ignition mechanism under microwave radiation.*

As discussed, the peak irradiation is limited by the tip diameter of the microwave emitter [31,49], in which case the incident power flux in these experiments was in the range of 11 – 85 kW/cm^2. This is quite consistent with prior work on Al/Fe_3O_4 thermite powder showing ignition thresholds of 1 - 2 MW/cm^2 [31]. This resulted in the ignition delay range of 2 – 8 s and is reflective of the material's microwave absorption properties which are inferior to the values observed for nTi [29]. For comparison, results with laser ignition in the UV and NIR *ranges show much smaller* power fluxes [12,58]. Use of 10.6 um wavelength CO_2 laser, on 70 wt. % Al/PTFE composites show ignition delay times of 40 – 400 ms under the laser fluxes of 100 – 600 W/cm^2 [61]. To understand the difference in

higher applied energies in microwave region as opposed to higher frequencies in IR range, the absorption efficiency (Q_{abs}) for Ti nanoparticles under 10.6 μm irradiation (28 THz) is illustrated in Figure 3-13. The efficiency of absorption of Ti nanoparticles in the IR region is ~10^7 times higher than observed values at 12 cm wavelength (2.45 GHz) from Figure 3-2. Dielectric permittivity of metals closely follows the $\varepsilon_1 = \frac{i\sigma}{\omega\varepsilon_0}$ relationship as described earlier [32]. A frequency increase of 10,000x results in the decrease of the metallic core's permittivity, which contributes to the overall rise in the observed absorption efficiency. Beyond the dependence of ignition delay on incident power flux and incident light's interaction with the sample, [5,9,10] laser ignition is a function of the sample's thermophysical properties [6,62]. This factor, as well as the effect of the dielectric properties of the samples, results in the observed differences in incident power fluxes between microwave and laser energy sources. However, unlike visible and IR frequency radiation, microwaves can penetrate deep into the volume of the material and enables volumetric heating as opposed to surface driven temperature rise presented by higher frequency waves. The enhanced penetration depth of microwaves offers the potential of 3-D printing of material with sensitizers strategically placed within the material to affect and control energy propagation.

3.5 Conclusions

This work investigated ignition mechanism of nTi composites under microwave radiation at 2.45 GHz. The ignition delay is categorized into an incident microwave energy power-dependent and power-independent regime. The power-dependent regime is

governed by slow heating rates, confirming that Ti/PVDF ignition is dictated by the heat accumulation rate. As an aside, one advantage of employing low heating rate could be local preheating for in-operando throttling of a propellant since the energy barrier needed for ignition could be partially overcome by increasing the temperature. At higher powers, the heating increases rapidly with the applied power, however, the increased temperatures had no effect on the ignition delay implying governance by another distinct mechanism. Thermogravimetric analysis on Ti/PVDF samples revealed that Ti oxidation with O_2 is suspected to occur earlier than metal fluorination with the polymer matrix. Since the shells of the nanoparticles contain TiN that oxidizes with air, the O_2 species reacts with both TiN and Ti, starting the combustion process. Calculation of the characteristic diffusion times of the O_2 through amorphous TiO_2 revealed that the ignition delay in the power-independent region closely matches the O_2 species diffusion time. This work demonstrates that heating rate and combustion kinetics dictate the ignition of Ti/PVDF composites under microwave radiation.

3.6 Supplemental Information

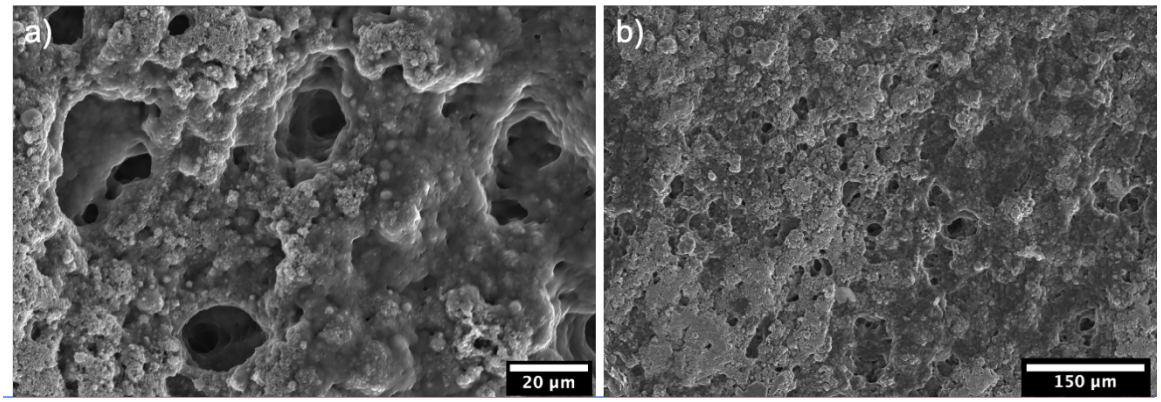

Figure 3-8. *Scanning electron microscope (SEM) images of 65 wt.% Ti/PVDF films.*

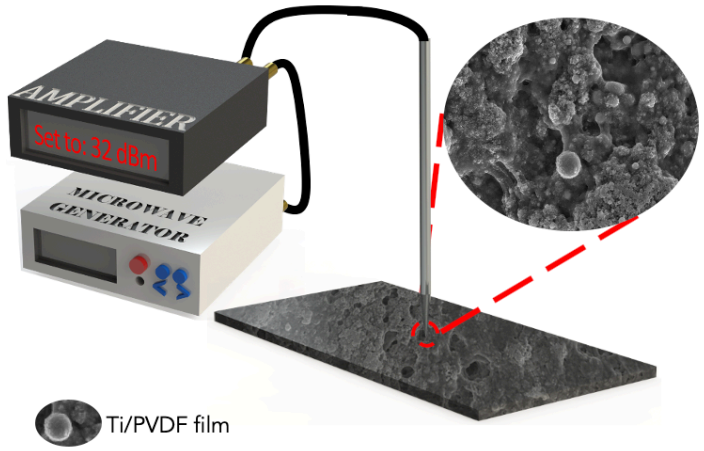

Figure 3-9. *Microwave ignition set-up.*

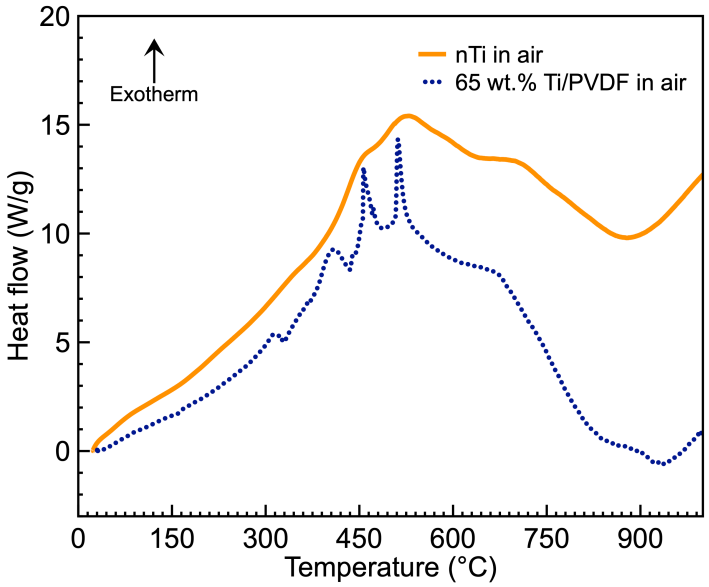

Figure 3-10. *Differential Scanning Colorimetry (DSC) of nTi and 65 wt.% Ti/PVDF at 10 K min^{-1} heating rate and 70 mL min^{-1} air flow rate.*

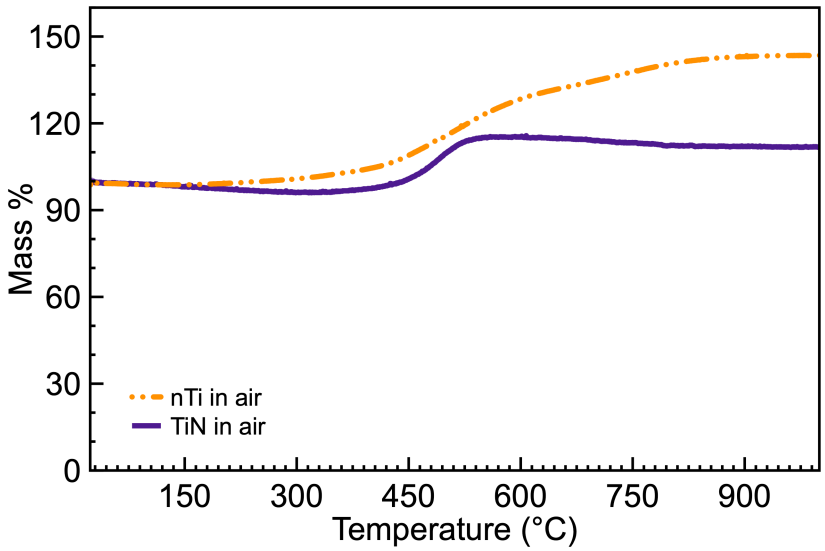

Figure 3-11. *Thermogravimetric analysis (TGA) on Ti and TiN nanoparticles in air.*

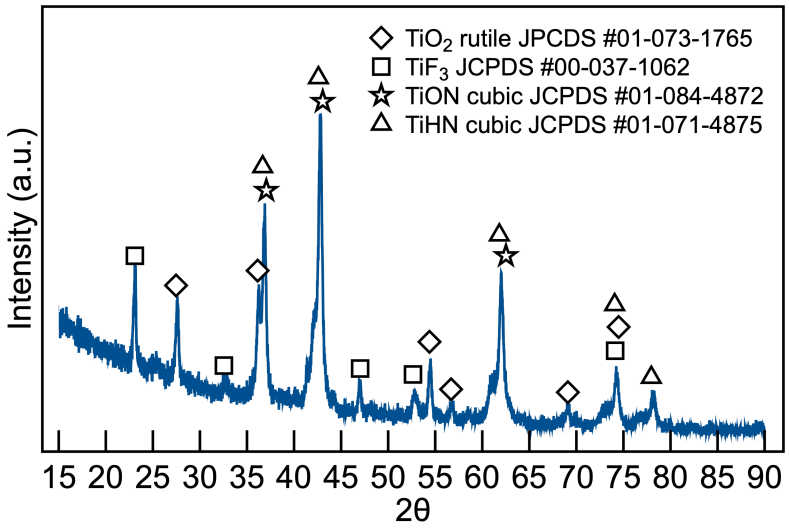

Figure 3-12. *X-ray diffraction (XRD) analysis on post-combustion products of 65 wt.% Ti/PVDF films burned in air.*

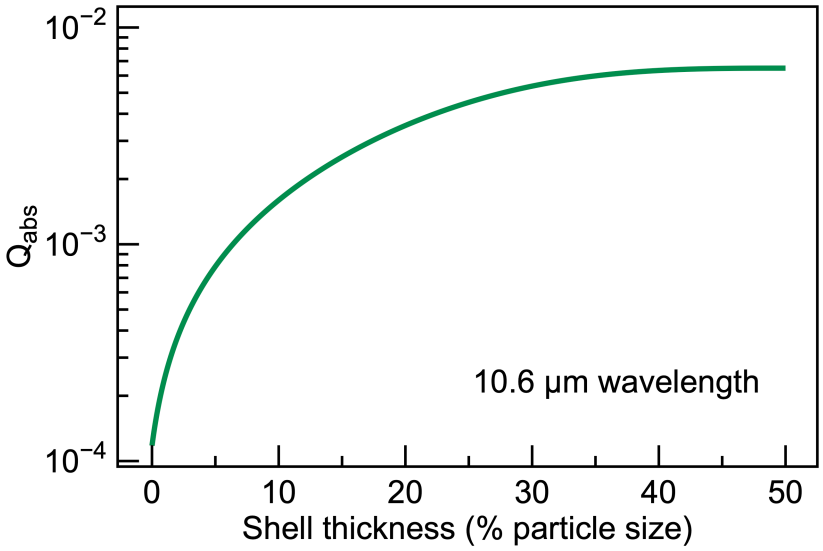

Figure 3-13. *Absorption efficiency of Ti nanoparticle at 10.6 um wavelength.*

The Mie coefficients for coated spheres:

$$a_n = \frac{\Psi_n(y)[\Psi_n'(m_2y) - A_n\chi_n'(m_2y)] - m_2\Psi_n'(y)[\Psi_n(m_2y) - A_n\chi_n(m_2y)]}{\xi_n(y)[\Psi_n'(m_2y) - A_n\chi_n'(m_2y)] - m_2\xi_n'(y)[\Psi_n(m_2y) - A_n\chi_n(m_2y)]} \quad (3\text{-}1)$$

$$b_n = \frac{m_2\Psi_n(y)[\Psi_n'(m_2y) - B_n\chi_n'(m_2y)] - \Psi_n'(y)[\Psi_n(m_2y) - B_n\chi_n(m_2y)]}{m_2\xi_n(y)[\Psi_n'(m_2y) - B_n\chi_n'(m_2y)] - \xi_n'(y)[\Psi_n(m_2y) - B_n\chi_n(m_2y)]}$$

$$A_n = \frac{m_2\Psi_n(m_2x)\Psi_n'(m_1x) - m_1\Psi_n'(m_2x)\Psi_n(m_1x)}{m_2\chi_n(m_2x)\Psi_n'(m_1x) - m_1\chi_n'(m_2x)\Psi_n(m_1x)}$$

$$B_n = \frac{m_2\Psi_n(m_1x)\Psi_n'(m_2x) - m_1\Psi_n(m_2x)\Psi_n'(m_1x)}{m_2\chi_n'(m_2x)\Psi_n(m_1x) - m_1\Psi_n'(m_1x)\chi_n(m_2x)}$$

where $m_1 = \sqrt{\varepsilon_1}$ and $m_2 = \sqrt{\varepsilon_2}$

$$k_c = k_m * \frac{1 + A*B*V_f}{1 - \psi*B*V_f}$$

$$\psi = 1 + \frac{1-\varphi_m}{\varphi_m^2} * V_f \quad (3\text{-}6)$$

$$B = \frac{\frac{k_f}{k_m} - 1}{\frac{k_f}{k_m} + A},$$

where φ_m is the maximum theoretical packing fraction of the filler, V_f is a volume fraction of the filler, k_f is the thermal conductivity of the filler, k_m is the thermal conductivity of the matrix and A is a constant taking into account relation of filler dimensions and orientation. In this calculation A = 1.5 for randomly packed spheres and φ_m = 0.637.

3.7 References

[1] B.P. Mason, C.M. Roland, Solid propellants, Rubber Chem. Technol. 92 (2019) 1–24. https://doi.org/10.5254/rct.19.80456.

[2] F.M. Gallant, H.A. Bruck, S.E. Prickett, M. Cesarec, Graded polymer composites using twin-screw extrusion: A combinatorial approach to developing new energetic materials, Compos. Part A Appl. Sci. Manuf. 37 (2006) 957–969. https://doi.org/10.1016/j.compositesa.2005.03.025.

[3] R.A. Chandru, N. Balasubramanian, C. Oommen, B.N. Raghunandan, Additive manufacturing of solid rocket propellant grains, J. Propuls. Power. 34 (2018) 1090–1093. https://doi.org/10.2514/1.B36734.

[4] M.S. McClain, I.E. Gunduz, S.F. Son, Additive manufacturing of ammonium perchlorate composite propellant with high solids loadings, Proc. Combust. Inst. 37 (2019) 3135–3142. https://doi.org/10.1016/j.proci.2018.05.052.

[5] N.K. Bourne, On the laser ignition and initiation of explosives, Proc. R. Soc. A Math. Phys. Eng. Sci. 457 (2001) 1401–1426. https://doi.org/10.1098/rspa.2000.0721.

[6] J.J. Granier, M.L. Pantoya, Laser ignition of nanocomposite thermites, Combust. Flame. 138 (2004) 373–383. https://doi.org/10.1016/j.combustflame.2004.05.006.

[7] E.D. Aluker, A.G. Krechetov, A.Y. Mitrofanov, D.R. Nurmukhametov, M.M. Kuklja, Laser initiation of energetic materials: Selective photoinitiation regime in pentaerythritol tetranitrate, J. Phys. Chem. C. 115 (2011) 6893–6901. https://doi.org/10.1021/jp1089195.

[8] Y. Jiang, S. Deng, S. Hong, J. Zhao, S. Huang, C.C. Wu, J.L. Gottfried, K.I. Nomura, Y. Li, S. Tiwari, R.K. Kalia, P. Vashishta, A. Nakano, X. Zheng, Energetic Performance of Optically Activated Aluminum/Graphene Oxide Composites, ACS Nano. 12 (2018) 11366–11375. https://doi.org/10.1021/acsnano.8b06217.

[9] A.N. Konovalov, N. V. Yudin, V.I. Kolesov, V.A. Ul'yanov, Increasing the heating efficiency and ignition rate of certain secondary explosives with absorbing particles under continuous infrared laser radiation, Combust. Flame. 205 (2019) 407–414. https://doi.org/10.1016/j.combustflame.2019.04.026.

[10] S.R. Ahmad, D.A. Russell, Laser ignition of pyrotechnics - Effects of wavelength, composition and confinement, Propellants, Explos. Pyrotech. 30 (2005) 131–139. https://doi.org/10.1002/prep.200400095.

[11] X. Fang, S. R. Ahmad, Laser ignitability of insensitive propellants, Adv. Mater. Sci. 3 (2018) 1–4. https://doi.org/10.15761/ams.1000139.

[12] L. de Yong, T. Nguyen, J. Waschl, Laser Ignition of explosives, pyrotechnics and propellans: a review, 1995.

[13] W.H. Sutton, Microwave processing of materials, MRS Bull. 18 (1993) 22–29. https://doi.org/10.1017/S0883769400038495.

[14] D.K. Agrawal, Microwave processing of ceramics, Curr. Opin. Solid State Mater. Sci. 3 (1998) 480–485. https://doi.org/10.1016/S1359-0286(98)80011-9.

[15] A. Mirzaei, G. Neri, Microwave-assisted synthesis of metal oxide nanostructures for gas sensing application: A review, Sensors Actuators, B Chem. 237 (2016) 749–775. https://doi.org/10.1016/j.snb.2016.06.114.

[16] B.D. de Greñu, R. de los Reyes, A.M. Costero, P. Amorós, J.V. Ros-Lis, Recent progress of microwave-assisted synthesis of silica materials, Nanomaterials. 10 (2020) 1–21. https://doi.org/10.3390/nano10061092.

[17] K. Hasue, M. Tanabe, N. Watanabe, S. Nakahara, F. Okada, A. Iwama, Initiation of some energetic materials by microwave heating, Propellants, Explos. Pyrotech. 15 (1990) 181–186. https://doi.org/10.1002/prep.19900150502.

[18] M.E. Daily, B.B. Glover, S.F. Son, L.J. Groven, X-band microwave properties and ignition predictions of neat explosives, Propellants, Explos. Pyrotech. 38 (2013) 810–817. https://doi.org/10.1002/prep.201300068.

[19] M. Curling, A. Collins, G. Dima, W. Proud, Progress towards microwave ignition of explosives, in: AIP Conf. Proc., 2009: pp. 486–489. https://doi.org/10.1063/1.3295180.

[20] H. Cheung, N. Cohen, On the performance of solid propellants containing metal additives, in: Solid Propellant Rocket Conf., 1964: pp. 1437–1440. https://doi.org/10.2514/6.1964-116.

[21] H. Wang, J. Shen, D.J. Kline, N. Eckman, N.R. Agrawal, T. Wu, P. Wang, M.R. Zachariah, Direct Writing of a 90 wt% Particle Loading Nanothermite, Adv. Mater. 31 (2019) 1–7. https://doi.org/10.1002/adma.201806575.

[22] K. Sullivan, M.R. Zachariah, Simultaneous pressure and optical measurements of nanoaluminum thermites: Investigating the reaction mechanism, J. Propuls. Power. 26 (2010) 467–472. https://doi.org/10.2514/1.45834.

[23] S. Horikoshi, R.F. Schiffmann, J. Fukushima, N. Serpone, Microwave chemical and

materials processing: A tutorial, 2017. https://doi.org/10.1007/978-981-10-6466-1.

[24] J. Ma, J.F. Diehl, E.J. Johnson, K.R. Martin, N.M. Miskovsky, C.T. Smith, G.J. Weisel, B.L. Weiss, D.T. Zimmerman, Systematic study of microwave absorption, heating, and microstructure evolution of porous copper powder metal compacts, J. Appl. Phys. 101 (2007). https://doi.org/10.1063/1.2713087.

[25] J. Sun, W. Wang, Q. Yue, Review on microwave-matter interaction fundamentals and efficient microwave-associated heating strategies, Materials (Basel). 9 (2016) 231. https://doi.org/10.3390/ma9040231.

[26] K.I. Rybakov, V.E. Semenov, S. V. Egorov, A.G. Eremeev, I. V. Plotnikov, Y. V. Bykov, Microwave heating of conductive powder materials, J. Appl. Phys. 99 (2006) 023506. https://doi.org/10.1063/1.2159078.

[27] T. Galek, K. Porath, E. Burkel, U. Van Rienen, Extraction of effective permittivity and permeability of metallic powders in the microwave range, Model. Simul. Mater. Sci. Eng. 18 (2010). https://doi.org/10.1088/0965-0393/18/2/025015.

[28] P. Biswas, G.W. Mulholland, M.C. Rehwoldt, D.J. Kline, M.R. Zachariah, Microwave absorption by small dielectric and semi-conductor coated metal particles, J. Quant. Spectrosc. Radiat. Transf. (2020) 106938.

[29] D.J. Kline, M.C. Rehwoldt, C.J. Turner, P. Biswas, G.W. Mulholland, S.M. Mcdonnell, M.R. Zachariah, Spatially focused microwave ignition of metallized energetic materials, J. Appl. Phys. 055901 (2020). https://doi.org/10.1063/1.5134089.

[30] M.C. Rehwoldt, Y. Yang, H. Wang, S. Holdren, M.R. Zachariah, Ignition of Nanoscale Titanium/Potassium Perchlorate Pyrotechnic Powder: Reaction Mechanism Study, J. Phys. Chem. C. 122 (2018) 10792–10800. https://doi.org/10.1021/acs.jpcc.8b03164.

[31] Y. Meir, E. Jerby, Thermite powder ignition by localized microwaves, Combust. Flame. 159 (2012) 2474–2479. https://doi.org/10.1016/j.combustflame.2012.02.015.

[32] C.F. Bohren, D.R. Huffman, Absorption and Scattering of Light by Small Particles, 1998. https://doi.org/10.1002/9783527618156.

[33] J. Kischkat, S. Peters, B. Gruska, M. Semtsiv, M. Chashnikova, M. Klinkmüller, O. Fedosenko, S. MacHulik, A. Aleksandrova, G. Monastyrskyi, Y. Flores, W.T. Masselink, Mid-infrared optical properties of thin films of aluminum oxide, titanium dioxide, silicon dioxide, aluminum nitride, and silicon nitride, Appl. Opt. 51 (2012) 6789–6798. https://doi.org/10.1364/AO.51.006789.

[34] M. Salemizadeh, F.F. Mahani, A. Mokhtari, Tunable mid-infrared graphene-titanium nitride plasmonic absorber for chemical sensing applications, J. Opt. Soc. Am. B. 36 (2019) 2863. https://doi.org/10.1364/josab.36.002863.

[35] Z.H. Liu, R.K.Y. Li, S.C. Tjong, C.L. Choy, X.G. Zhu, Z.N. Qi, F.S. Wang, Influence of particle dispersion on the matrix ligament thickness of polymer blends 2. A generalized equation and particle spatial distributions for different morphologies, Polymer (Guildf). 40 (1999) 2903–2915. https://doi.org/10.1016/S0032-3861(98)00533-3.

[36] K.D. Maglić, D.Z. Pavičić, Thermal and electrical properties of titanium between 300 and 1900 K, Int. J. Thermophys. 22 (2001) 1833–1841. https://doi.org/10.1023/A:1013151303111.

[37] B.I. Ermolaev, Thermal conductivity and electrical conductivity of materials based on titanium and its alloys at temperatures from 20-80, (1974) 46–47.

[38] W. Zhou, J. Zuo, W. Ren, Thermal conductivity and dielectric properties of Al/PVDF composites, Compos. Part A Appl. Sci. Manuf. 43 (2012) 658–664. https://doi.org/10.1016/j.compositesa.2011.11.024.

[39] G. Krishna Bama, P. Indra Devi, K. Ramachandran, Structural and thermal properties of PVDF/PVA blends, J. Mater. Sci. 44 (2009) 1302–1307. https://doi.org/10.1007/s10853-009-3271-8.

[40] T.B. Lewis, L.E. Nielsen, Dynamic Mechanical Properties of Particulate- Filled Composites, J. Appl. Polym. Sci. 14 (1970) 1449–1471.

[41] L.E. Nielsen, Thermal Conductivity of Particulate-Filled Polymers, J. Appl. Polym. Sci. 17 (1973) 3819–3820.

[42] P.J. Linstrom, W.G. Mallard, NIST Chemistry webBook, NIST Standard Reference Database Number 69, Natl. Inst. Stand. Technol. (2014). https://doi.org/citeulike-article-id:3211271.

[43] M.S. Jayalakshmy, J. Philip, Enhancement in pyroelectric detection sensitivity for flexible LiNbO3/PVDF nanocomposite films by inclusion content control, J. Polym. Res. 22 (2015) 1–11. https://doi.org/10.1007/s10965-015-0688-4.

[44] E. Jerby, V. Dikhtyar, The microwave drill, Science. 298 (2002) 587–589.

[45] V. Dikhtyar, E. Jerby, Fireball ejection from a molten hot spot to air by localized microwaves, Phys. Rev. Lett. 96 (2006) 1–4. https://doi.org/10.1103/PhysRevLett.96.045002.

[46] E. Jerby, A. Golts, Y. Shamir, S. Wonde, J.B.A. Mitchell, J.L. Legarrec, T. Narayanan, M. Sztucki, D. Ashkenazi, Z. Barkay, N. Eliaz, Nanoparticle plasma ejected directly from solid copper by localized microwaves, Appl. Phys. Lett. 95 (2009) 93–96. https://doi.org/10.1063/1.3259781.

[47] S. Popescu, E. Jerby, Y. Meir, Z. Barkay, D. Ashkenazi, J.B.A. Mitchell, J.L. Le Garrec, T. Narayanan, Plasma column and nano-powder generation from solid titanium by localized microwaves in air, J. Appl. Phys. 118 (2015). https://doi.org/10.1063/1.4926491.

[48] E. Jerby, O. Aktushev, V. Dikhtyar, Theoretical analysis of the microwave-drill near-field localized heating effect, J. Appl. Phys. 97 (2005). https://doi.org/10.1063/1.1836011.

[49] E. Jerby, Y. Meir, A. Salzberg, E. Aharoni, A. Levy, J.P. Torralba, B. Cavallini, Incremental metal-powder solidification by localized microwave-heating and its potential for additive manufacturing, Addit. Manuf. 6 (2015) 53–66. https://doi.org/10.1016/j.addma.2015.03.002.

[50] C. Gong, H. Meng, X. Zhao, X. Zhang, L. Yu, J. Zhang, Z. Zhang, Unique Static Magnetic and Dynamic Electromagnetic Behaviors in Titanium Nitride/Carbon Composites Driven by Defect Engineering, Sci. Rep. 6 (2016) 1–7. https://doi.org/10.1038/srep18927.

[51] M. Green, A.T. Van Tran, R. Smedley, A. Roach, J. Murowchick, X. Chen, Microwave absorption of magnesium/hydrogen-treated titanium dioxide nanoparticles, Nano Mater. Sci. 1 (2019) 48–59. https://doi.org/10.1016/j.nanoms.2019.02.001.

[52] M. Green, P. Xiang, Z. Liu, J. Murowchick, X. Tan, F. Huang, X. Chen, Microwave absorption of aluminum/hydrogen treated titanium dioxide nanoparticles, J. Mater. 5 (2019) 133–146. https://doi.org/10.1016/j.jmat.2018.12.005.

[53] J.B. Delisio, X. Hu, T. Wu, G.C. Egan, G. Young, M.R. Zachariah, Probing the Reaction Mechanism of Aluminum/Poly(vinylidene fluoride) Composites, J. Phys. Chem. B. 120 (2016) 5534–5542. https://doi.org/10.1021/acs.jpcb.6b01100.

[54] J.B. DeLisio, C. Huang, G. Jian, M.R. Zachariah, G. Young, Ignition and reaction analysis of high loading nano-Al/fluoropolymer energetic composite films, 52nd Aerosp. Sci. Meet. (2014) 1–8. https://doi.org/10.2514/6.2014-0646.

[55] S. Zulfiqar, M. Zulfiqar, M. Rizvi, A. Munir, I.C. McNeill, Study of the thermal degradation of polychlorotrifluoroethylene, poly(vinylidene fluoride) and copolymers of chlorotrifluoroethylene and vinylidene fluoride, Polym. Degrad. Stab. 43 (1994) 423–430. https://doi.org/10.1016/0141-3910(94)90015-9.

[56] H. Li, H. Kim, Thermal degradation and kinetic analysis of PVDF/modified MMT nanocomposite membranes, Desalination. 234 (2008) 9–15. https://doi.org/10.1016/j.desal.2007.09.064.

[57] N. V. Muravyev, K.A. Monogarov, A.N. Zhigach, M.L. Kuskov, I. V. Fomenkov, A.N. Pivkina, Exploring enhanced reactivity of nanosized titanium toward oxidation, Combust. Flame. 191 (2018) 109–115. https://doi.org/10.1016/j.combustflame.2018.01.011.

[58] O.G. Glotov, Ignition and combustion of titanium particles. Experimental methods and results, Uspekhi Fiz. Nauk. 189 (2019) 135–171. https://doi.org/10.3367/ufnr.2018.04.038349.

[59] J.W. Rogers, K.L. Erickson, D.N. Belton, R.W. Springer, T.N. Taylor, J.G. Beery, Low temperature diffusion of oxygen in titanium and titanium oxide films, Appl. Surf. Sci. 35 (1988) 137–152. https://doi.org/10.1016/0169-4332(88)90043-8.

[60] E.J. Carr, Characteristic time scales for diffusion processes through layers and across interfaces, Phys. Rev. E. 97 (2018) 1–9. https://doi.org/10.1103/PhysRevE.97.042115.

[61] M.A. Rubio, I.E. Gunduz, L.J. Groven, T.R. Sippel, C.W. Han, R.R. Unocic, V. Ortalan, S.F. Son, Microexplosions and ignition dynamics in engineered aluminum/polymer fuel particles, Combust. Flame. 176 (2017) 162–171. https://doi.org/10.1016/j.combustflame.2016.10.008.

[62] S.C. Stacy, M.L. Pantoya, Laser ignition of nano-composite energetic loose powders, Propellants, Explos. Pyrotech. 38 (2013) 441–447. https://doi.org/10.1002/prep.201200157.

4 Microwave Stimulation of Energetic Al-based Nanocomposites for Ignition Modulation[1]

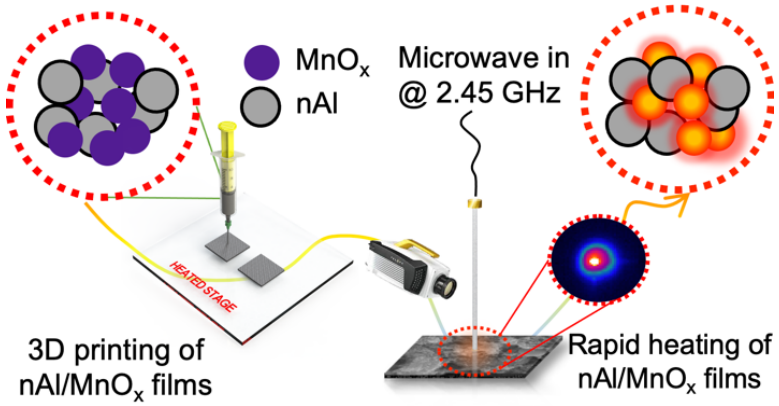

4.1 Summary

Although electromagnetic stimulation promises safe and controlled ignition of energetic materials, ultraviolet (UV) to infrared (IR) wavelengths sources experience significant photon attenuations in energetic materials. Conversely, radiation in microwave frequencies is recognized for instantaneous volumetric heating capabilities. However, many energetics are poor microwave heaters and to accelerate the heating recent efforts focused on adding microwave susceptors, which do not participate in the energetic reaction. This effort is first to demonstrate that nanoscale aluminum (nAl)/manganese oxide (MnO_x) can be rapidly heated at rates ~10^4 °C/s under microwave radiation without addition of inert microwave susceptors. Detailed analysis of nanoscale MnO_x was performed via XPS, XRD and TEM. The samples of MnO_x at different loadings of nAl were 3D printed into composite films and tested with a microwave applicator at 2.45 GHz frequency. Infrared thermometry experiments showed that with increase in MnO_x content

the heating rate in the samples increases by orders of magnitude. Computational modeling based on the dielectric and thermo-physical properties of the materials showed that electric field is the dominant mechanism accounting for ~96% of the heating of the nAl/MnOx composites at microwave frequencies. The microwave ignition mechanism was deconvoluted via high-speed IR imaging, in-situ TOFMS, T-jump and TGA/DSC analysis. The results show that microwave stimulation can effectively heat and control ignition in nAl based thermites with MnO_x, where the oxidizer acts dually as a microwave susceptor and ignition driver.

⊥The findings presented in this chapter have been previously published and are reprinted with permission from: Alibay, Zaira, Daniel Olsen, Prithwish Biswas, Cody England, Feiyu Xu, Pankaj Ghildiyal, Min Zhou, and Michael R. Zachariah. "Microwave Stimulation of Energetic Al-Based Nanoparticle Composites for Ignition Modulation." ACS Applied Nano Materials (2022). Copyright 2022 American Chemical Society. All modeling work presented in this chapter has been performed in collaboration with Daniel H. Olsen from Dynamic Properties Research Lab under Dr. Min Zhou's supervision at Georgia Institute of Technology.

4.2 Introduction

With uses spanning from micro-chip initiators to automobile safety airbags, energetic materials have found applications in both military and civilian industries. Nanoscale heterogeneous energetic materials have been of particular interest due to their high energy density, environmental benignancy and tunability [1–5]. Although successfully employed, safe and controlled ignition of solid propellants as well as dynamic modulation of their energy release rates is a challenge [6]. One way of addressing this challenge has been through the assembly and additive manufacturing of nanoscale thermites with tunable energy release rates during combustion [7–9]. Along this path, electromagnetic (EM) stimulation via laser or flash ignition [10–12] has been used as a means of safe ignition. In this regard, ultraviolet (UV) to infrared (IR) frequencies have been widely explored for ignition, however, the associated high photon attenuation in energetic materials has limited the complete exploitation of the propellant volume [13–16]. Uhlenhake *et. al* showed that the absorbed energy in nAl (nano aluminum)/PVDF energetic composite films, at a 10 wt.% loading, diminishes within a ~4 μm depth, indicating that the UV-IR wavelength ignition sources primarily rely on surface heating effects [17]. To address this challenge, one could extend the incident wavelength to microwave frequencies: 300 MHz – 3000 GHz.

Unlike UV, visible, and IR radiation, microwave wavelengths are low energy and capable of penetrating deep into the material volume. Microwave radiation incident on a material can lead to dielectric heating, arc discharge, and ionization of the gaseous species, which in turn can be employed to modulate combustion performance [18,19]. Dielectric

heating is expected to be the initiator to thermally driven reactions and would occur before gaseous species are released. This dielectric heating is expected to be a primary contributor in overcoming the reaction activation barrier and regulating the ignition event [20]. Research on microwave stimulation of metal particles (often used as fuels) have demonstrated that the dielectric (native oxide) coating on metals can dramatically increase electromagnetic (EM) absorption in otherwise microwave insensitive particles [21,22]. This led to the design of architectures where nTi coated with TiO_2/TiN was used to stimulate microwave ignition in energetic materials [23].

On the other hand, aluminum is nominally the fuel of choice due to its relatively low cost, and mass and volume specific energy density [24–28]. However, the dielectric properties of nAl render it relatively microwave insensitive [23,29]. Thermites of nAl/Fe_3O_4 previously studied under microwave stimulation show that while initiation can be obtained, the event extended to several minutes [30]. To compensate for the microwave passiveness of nAl, sensitizers such as graphene, carbon nanotubes and reduced graphene oxide (rGO) have been added to energetic materials [29,31,32] to ignite and modulate combustion via microwave radiation. Since these materials do not participate in the energetic reaction, the increase in the microwave sensitivity decreases the exothermic output of the composites. This finding led to our exploration of metal oxides that are capable of harnessing the energy density of nAl while being microwave sensitive. The manganese dioxide (MnO_2) reaction with nAl has been previously studied [33–35] and the theoretical heat release from the thermite reaction of MnO_2 and Al is higher or comparable to classical thermites of Al/Fe_3O_4 and Al/CuO [27]. Moreover, multivalent manganese

oxides (-3 - +7 oxidation states) have been shown to have high dielectric constant values and have been utilized in microwave assisted catalysis applications [36–41]. The dielectric properties of the oxidizer open avenues for exploration of the metal oxide in nAl based microwave stimulated thermites.

In this work, we investigate the microwave heating and ignition mechanism of nanoscale Al/MnO_x energetic composites. We study the heating rates of MnO_x composites via infrared thermometry and primary heating mechanisms via finite element simulations under incident microwaves at 2.45 GHz. The detailed analysis of the MnO_x nanopowder composition was performed via X-ray diffraction (XRD), X-ray photoelectron spectroscopy (XPS) and thermogravimetric analysis (TGA) techniques. The morphology of the as-received MnO_2/Mn_2O_3 nanopowders as well as of direct-ink written films were characterized with Scanning Electron and Transmission Electron Microscopy (SEM and TEM). Commercially available mixtures of MnO_2/Mn_2O_3 were formulated with nAl at different equivalence ratios to better understand the range of microwave ignition of nAl based thermites. In-situ temperature-jump ignition (T-jump), time-of-flight mass spectroscopy (TOFMS) and differential scanning calorimetry (DSC) were used to uncover the thermochemical reactions in the 3D printed energetic composites and shed a light on the ignition mechanism. This chapter demonstrates that MnO_x is an excellent oxidizer for microwave ignition with nAl and not only drives the heating of the energetic composites under microwave stimulation but also controls the ignition in the 3D printed nAl/MnO_x films.

4.3 Material and Methods

4.3.1 Materials and Sample Preparation

Manganese dioxide (MnO_2, 50 – 80 nm) and aluminium nanoparticles (nAl, 80 nm) were purchased from US Research Nanomaterials, Inc. and Novacentrix, respectively. Thermogravimetric analysis showed that nAl has 77% active metal content by mass, which was considered in all stoichiometric calculations of nAl/MnO_x formulations. Methylcellulose (HPMC, METHOCEL™ F4M) with a molecular weight of 86,000 was purchased from DuPont. Polyvinylidene fluoride (PVDF, average molecular weight: ~534,000) and N, N-Dimethylformamide (DMF, 99.8%) were purchased from Sigma Aldrich. All materials were us as received with no further treatment.

A polymer base for the high loading solid inks was first prepared by dissolving PVDF and HPMC at 2/3 mass ratio in DMF with a total polymer concentration of 31.25 mg/mL. The polymer solution was magnetically stirred for a minimum of 2 hours. Nanopowder was then added to the clear solution and lightly vortexed and sonicated for 30 minutes in Branson sonicator. The vortexing and sonication steps were repeated after each new addition of a constituent. After all components were added, the ink was magnetically stirred for 24 hours and mechanically mixed for 1.5 hours prior to fabrication by 3D printing.

4.3.2 3D Printed Film Fabrication

The prepared ink was transferred to a 10 mL Beckman Colder syringe with a 16-gauge needle tip (1.6 mm ID) and printed on a hot bed via direct-ink writing method on a Hyrel 3D printer. The temperature of the hot bed was maintained at 70ºC to allow evaporation of the DMF as the film layers were printed. The inks were printed at 250 mm/min with extrusion rate of 56.3 mm^3/min and a total of two layers were printed for all ink formulations.

4.3.3 Morphology and Thermochemistry Characterization

X-ray photoelectron spectroscopy (XPS) characterization was carried out by using a Kratos AXIS ULTRA^{DLD} XPS system equipped with an Al Kα X-ray source and a 165-mm mean radius electron energy hemispherical analyzer. The as-received MnO_x nanopowder and microstructures of the printed samples were investigated with a Thermo-Fisher Scientific NNS450 scanning electron microscope (SEM) and Transmission Electron Microscope (TEM) Talos L120C. Powder X-ray diffraction (XRD, PANalytical Empyrean Series 2, Cu-Kα source (λ=1.543 Å)) was employed to analyze MnO_x nanopowder with a step size of 0.013°.

Interactions of the fabricated film with air, as well as interactions of MnO_x with nAl in the PVDF/HPMC matrix were investigated with simultaneous thermogravimetry–differential scanning calorimetry (TGA-DSC) (STA 449 F3 Jupiter, NETZCSH). The

samples were heated at a rate of 10 K min^{-1} from 25°C to 1000°C in air and under an argon flow rate of 70 mL min^{-1}. Masses of 1–3 mg were loaded per TGA-DSC run.

4.3.4 Microwave Emitter Configuration

A spatially localized microwave emitter apparatus has been employed for all microwave heating tests with the infrared camera and is described in more details in Chapter 2.3.3 [23]. The emitter configuration includes a solid-state microwave generator (DS Instruments SG12000) with peak power output of 10 dBm at 2.45 GHz as seen in Figure 4-1. The output signal from the generator is then amplified by a solid-state amplifier with the peak gain of 32 dB, allowing the output power to be maximized to 42 dBm (~15 W). The output signal is the transmitted through a coaxial cable terminated with a nickel-plated straight pin (Singer 0.025″ diameter, mm length) mounted on a custom-made brass adapter. The sample to antenna distance was controlled via a micrometer-precision translational stage, where the antenna tip was placed directly in contact with the sample without penetrating the material as seen in Figure 4-1.

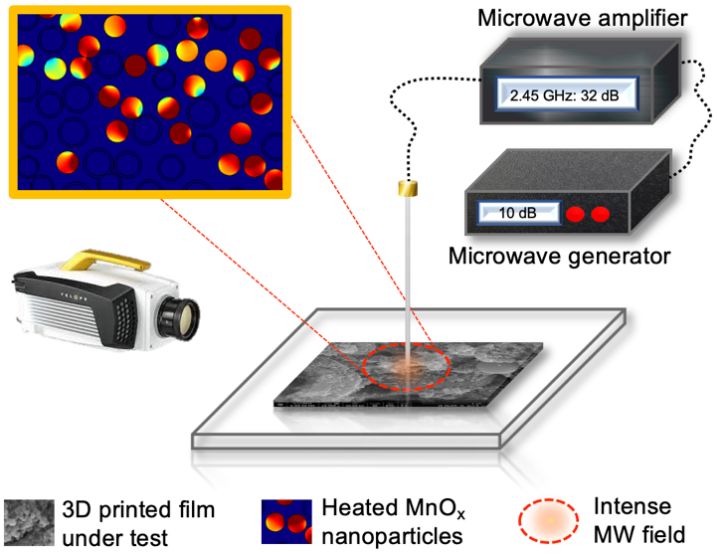

Figure 4-1. *Schematic illustration of the microwave emitter configuration.*

4.3.5 Thermal Imaging Characterization

A Telops FASTM3K infrared (IR) camera was used to measure surface temperature at 10,000 - 20,000 frames per second during microwave irradiation. A 50 mm lens with 1 inch extender ring was attached to the camera (In/Sb detector) and a fixed exposure of 5 µs was used on all acquired images. The camera was set to a temperature range of 0–151°C per the calibration range of the device. The heating rates were calculated as slopes of the temperature vs. time curves. The pixel pitch of the camera detector was 30 µm and the temperature was averaged over 75 µm region when the lens was situated 268 mm away from the sample.

4.3.6 Modeling/Simulations

Along with the experimental studies, computational analyses of the microwave heating of the MnO_x and nAl/MnO_x in PVDF matrix were carried out. The primary intent is to understand how heating occurs through the interactions of the electric and magnetic fields (E-field and H-field respectively) of the incident microwaves with the composite microstructures of both dielectric and conducting constituents. To this end, the microstructure models include four constituents: PVDF, aluminum oxide (Al_2O_3), aluminum (Al), and MnO_x. HPMC was not included in the matrix as the polymer's thermophysical properties are similar to that of PVDF. Particles in the microstructure have radii of between 25 and 35 nm for aluminum and only 25 nm for MnO_x. The thickness of the oxide shell around each aluminum particle is such that the active aluminum core is 77 wt.%, matching that for the nAl used experimentally. The core-shell structured particles are embedded in the PVDF binder matrix. The microstructures were used in electrodynamic calculations which track the E-fields and the H-fields through which dielectric heating and conductive heating are evaluated.

The calculations were carried out in COMSOL Multiphysics® [42]. The microstructure samples are 3 μm × 8 μm in size. This size is smaller than the 2 mm × 2 mm × 250 μm sample size used in the experiments, as necessitated by high computational costs for larger samples. Even so, the model allows the mechanisms and extent of heating to be analyzed. This computationally efficient model probes the scattering and absorption of the incident energy by the particles and the binder in the microstructures. To match the experiments, multiple samples with different amounts of nAl and MnO_x were created. The

particles are approximately uniformly distributed in the microstructures; particulate agglomeration and voids were not modeled. The excitation condition emulates that in the experiments, with the incident wave coming from the top of the two-dimensional sample and the E-field vector in plane and horizontal. The symmetrical boundary conditions were applied at the edges of the 3 μm wide sample, where incident wave was incident evenly across the top and heat losses to the surrounding were not accounted for. The boundary condition at the bottom edge of the sample was transparent such that EM waves can pass through deeper into the material, thereby accounting for the effect of the larger specimen size in the experiments. The model setup allows the effects of microstructure to be explicitly analyzed.

Table 4-1. *Material properties of constituents.*

	nAl [43]	Al_2O_3 [43]	PVDF [44,45]	MnO_2 [46-48]	Mn_2O_3 [41,48]
Mass Density (kg/m^3)	2941	3970	1780	5030	4500
Relative Permittivity	1	9.6 - 0.0006j	7 - 0.0009j	10.47 – 3.58j	4 – 3j
Relative Permeability	1	1	1	1.03 - 0.1j	1
Electrical Conductivity ($S \cdot m^{-1}$)	3.75×10^7	1×10^{-14}	1×10^{-10}	5×10^{-14}	1×10^{-12}
Specific Heat ($J \cdot mol^{-1} \cdot K^{-1}$)	900	765	1200	54.1	80
Thermal Conductivity ($W \cdot m^{-1} \cdot K^{-1}$)	237	36	0.19	0.209	0.4

4.3.7 T-jump Ignition and Time-of-Flight Mass Spectroscopy

The ignition temperatures of the energetic composites and temporal evolution of O_2 species from MnO_x were measured by T-jump and time-of-flight mass spectroscopy (TOFMS) methods that are described in more detail elsewhere [49]. Briefly, the samples were thinly coated on a Pt wire (length~0.8 cm, diameter ~76 µm, Omega Engineering, Inc) which was pulse heated to ~1500 K at ~10^5 K/s in a specialized chamber. The measurements were conducted either under vacuum or air/Argon at 1 atm. The temperature of the wire is monitored by probing the current and voltage across the wire at a temporal resolution of 100 ns. The ignition delay time was captured at ~µs resolution with high-speed camera (Vision Research Phantom V12.1). The ignition time was defined as a time of first light after which sustained combustion on the wire was observed. The measured ignition timestamps were coupled to the wire temperatures (calculated via the Callendar-Van Dusen Equation) to determine the corresponding ignition temperatures.

4.4 Results

The composition of as-received manganese oxide powder was characterized via X-ray photoelectron spectroscopy (XPS), X-ray diffraction analysis (XRD) and thermogravimetric analysis (TGA). XRD analysis in Figure 4-2c demonstrated that the metal oxide contains crystalline phase Mn_2O_3. XPS analysis showed that the Mn $2p_{3/2}$ peak of the as-received powder (642.0 eV) is close to that of Mn^{4+} (MnO_2) at 642.1 eV (Figure 4-2a). The shift to a lower binding energy is indicative of the presence of Mn^{3+}. Further investigation of the splitting of Mn 3s peaks, MnO_2 (ΔE = 4.8 eV), Mn_2O_3 (ΔE = 5.5 eV),

and MnO (ΔE = 5.9 eV), has been used to distinguish different oxidation states of manganese oxides [50–52]. In Figure 4-2a, the splitting of the as-received powder is 5.1 eV, which is between the characteristic values of MnO_2 and Mn_2O_3. These results suggest that as-received MnO_2 nanopowder is in fact an assortment of MnO_2 and Mn_2O_3. The absence of the MnO_2 traces in XRD spectra confirms (Figure 4-2c) that there is no crystalline phase manganese dioxide present in the as-received powders; however, characteristic $2p_{3/2}$ and 3s traces of MnO_2 in XPS spectra reveal the presence of amorphous phase Mn^{4+} species. To quantitatively analyze bulk composition of the manganese oxide powder, thermogravimetric analysis was performed in an argon environment. A two-step mass loss under argon flow in the TGA plot of Figure 4-2d is characteristic of phase transition of MnO_2 → Mn_2O_3 at 530ºC (5.4% loss) and Mn_2O_3 → Mn_3O_4 at 730ºC (3.7% loss) [33,53]. Calculation of the mass balance Equations 4-1 and 4-2 presented below concludes that the as-received powder is a mixture of 40 wt.% Mn_2O_3 and 60 wt.% MnO_2.

$$4MnO_2 \rightarrow 2Mn_2O_3 + O_2 \uparrow \quad (4\text{-}1)$$

$$6Mn_2O_3 \rightarrow 4Mn_3O_4 + O_2 \uparrow \quad (4\text{-}2)$$

The particles of MnO_2/Mn_2O_3 have a primary size distribution from 30 – 50 nm (Figure 4-2f -h) and form nanoparticle clusters in the as-received powders as shown in Figure 4-2e and f. For simplicity, the MnO_2/Mn_2O_3 nanoparticles at 2/3 mass ratio will be referred as MnO_x in the rest of the paper.

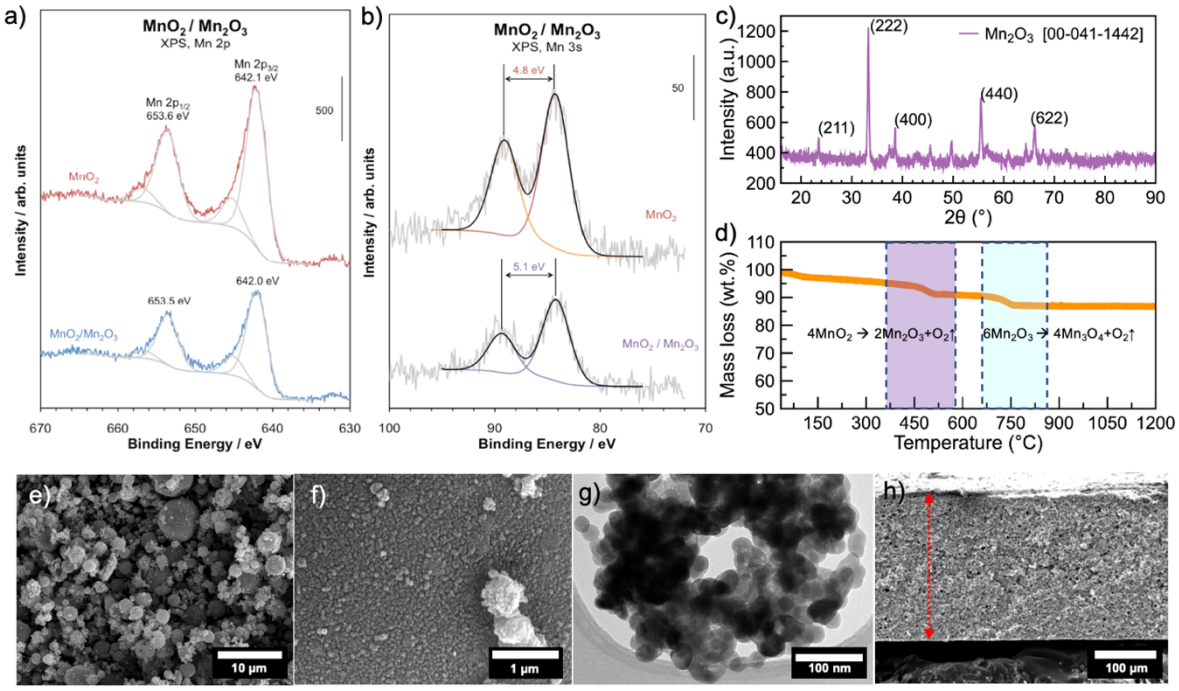

Figure 4-2. *X-ray photoelectron spectroscopy of the as-received manganese oxide powder showing a mixture of MnO_2 and Mn_2O_3: a) spectrum of 2p peaks b) spectrum of 3s peaks; c) X-ray diffraction analysis of the manganese oxide nanopowder; d) Thermogravimetric analysis of the as-received nanopowder in argon demonstrating phase change from MnO_2 → Mn_2O_3 and Mn_2O_3 → Mn_3O_4 and respective O_2 content loss; e-f) SEM images of the MnO_2/Mn_2O_3 nanopowder; g) TEM of the nanopowder; h) SEM image of the fabricated MnO_2/Mn_2O_3 film at 90 wt.% MnO_x loading in 4 wt.% PVDF/6 wt.% HPMC matrix.*

The obtained MnO_x nanopowder was processed into inks at 90 wt.% solid loading and printed at a 250 µm thickness as shown in Figure 2h. The films were tested with the monopole antenna set-up at 2.45 GHz incident EM radiation (Figure 4-1). The infrared camera tests under 15W of applied microwave power showed that the heating rate of manganese oxide was on the order of $2x10^5$ °C/s (see Figure 4-3a). The heating rate of the

printed composites was computed in a temperature region below which any exothermic/endothermic chemistry occurs, determined by differential scanning calorimetry (described later). The heating is first localized to a few pixels under the immediate area of the antenna tip. As time progresses the heated region expands to over 250 μm radial depth (see Figure 4-3c-f). The initial localization of the heating is due to the higher intensity field present at the antenna tip [54–56], therefore the microwave sensitizer was kept in close proximity to the higher microwave intensity zone. The spread of the heated region over the immediate microwave incidence zone is mainly due to heat conduction away from the microwave sensitized zone, based on the characteristic thermal diffusion times of the assembled films. The finite element simulations of the heating of the film microstructure demonstrate that nanoparticles instantly heat under the incident wavelength and reach thermal equilibrium with the polymer binder surrounding them in ~1 ms. This is due to the instantaneous nature of energy transfer from EM absorption to thermal output [57]. Manganese oxide is non-magnetic [40,46,58] , hence heating of MnO_2/Mn_2O_3 occurs primarily *via* the electric rather than the magnetic field. This is illustrated in Figures 3b, which shows that the power absorbed by electric field in the nanoparticles is 3 orders of magnitude higher than that of the magnetic field, where maximum electric field absorption at the film surface is 160 GW/m^3 and magnetic field absorption is 0.12 GW/m^3. To understand the effect of nAl loading in microwave heating and ignition of the nAl/MnO_x thermite system, the infrared thermometry of fabricated films was studied at different equivalence ratios.

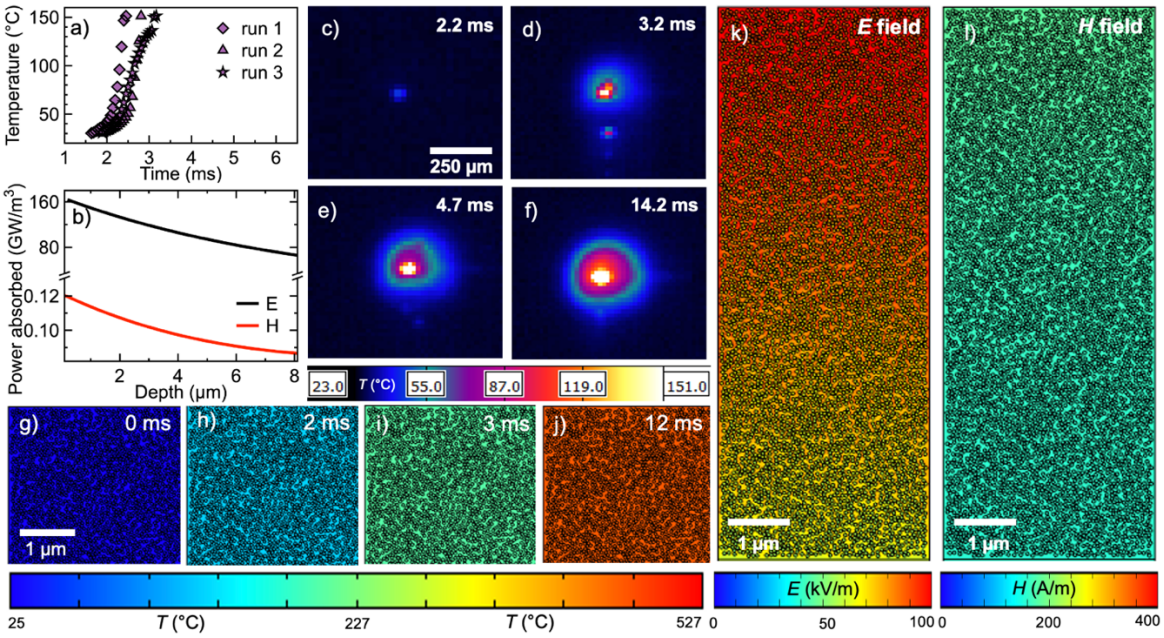

Figure 4-3. *a) Experimental heating rate from thermal imaging; b) power absorbed by electric and magnetic field components as a function of film depth from finite element simulation results; c-f) infrared thermometry snapshots of MnO_2/Mn_2O_3 films; f–i) finite element simulation results of temperature profiles in the microstructure of the MnO_2/Mn_2O_3 films; j) electric field profile of the MnO_2/Mn_2O_3 films at t = 1 ms; k) magnetic field profile in the MnO_2/Mn_2O_3 film at t = 1 ms.*

Since microwave absorption of nAl is negligible [23,59] one must rely on the manganese oxide sensitizer content which can be increased to change heating rate in the films as demonstrated in Figure 4a both experimentally and *via* modeling. The heating rates based on the modeling show similar trend as the experimentally observed values, where MnO_x content decrease is accompanied by lower heating rates. The difference between the experimental and modeled values can be attributed to inhomogeneous distribution of

nanoparticles in the films and limitations of the 2-dimensional modeling where heat losses to the environment were not fully encompassed as described in the experimental section. Additionally, the actual dielectric properties of the MnO_x nanoparticles might differ from the values found in literature where were used in the computations. However, the results still depict the microwave incidence effects in the microstructures of the nAl/MnO_x composites. Experimental microwave heating rate increases from $5x10^3$ ºC/s to $1.3x10^4$ ºC/s as the content of MnO_x is increased from 60 wt.% (equivalence ratio, φ=0.4) to 75 wt.% (equivalence ratio, φ=1). This range also demarks the ignition threshold with ignition taking place within a 10-100 ms temporal window. Below this threshold level, the exposure times up to 1 min still do not lead to ignition. For the ignition to occur the rate of energy deposition ($\rho c_p \frac{dT}{dt}$) must surpass the energy threshold presented by minimum ignition energy (MIE) presented in Equation 4-3 below:

$$\rho c_p \frac{dT}{dt} \geq \frac{MIE}{t_{ign}} \tag{4-3}$$

$$MIE = \rho c_p \left(T_{ign} - T_{ambient}\right) \tag{4-4}$$

where ρ is the composite density, c_p is the specific heat capacity, $\frac{dT}{dt}$ is the rate of temperature change, T_{ign} is the ignition temperature, $T_{ambient}$ is the ambient temperature and t_{ign} is the time to ignition. As discussed later (Figure 4-6a), sample heating below 180ºC does not involve any endothermic/exothermic chemistry. Therefore, the external

heat generation rate in this region (based upon the values from Figure 4a) is a sole result of the balance between microwave absorption of the composites and the heat losses involved (see Equation 4-5).

$$T < 180℃ \rightarrow \dot{Q}_{chem} = 0$$

$$\rho c_p \frac{dT}{dt} = \dot{Q}_{abs} - \dot{Q}_{lost} \quad (4\text{-}5)$$

The heat generation rate left side of Equation 4-5 can be deduced experimentally from the rate of temperature change and material properties (Table 4-1) to yield 14.4 and 5.6 GW/m^3 for the 75 and 60 wt.% samples respectively. From Equation 4-4 the minimum energy (MIE) required to ignite the sample based on T-jump ignition data was 651 and 676 MJ/m^3 for the φ=1 and φ=0.4 samples, respectively. Importantly, the ignition temperatures from T-jump data were selected due to the proximity of the latter to microwave heating rates of 10^3 - 10^5 ºC/s. An estimate of the time to ignition from Equation 4-3 using the experimental power absorbed and the MIE gives a *minimum time to ignition* in the two samples of 45 ms and 117 ms. Although this analysis does not consider any exothermicity occurring prior to ignition, the alignment of *minimum* estimated time with the experimentally determined ignition delay times (φ=0.4 samples) demonstrates that the MW source is acting as a thermal heat source at the particle level. Interestingly, the relation between sensitizer content and heating rate is non-linear, where 15 wt.% decrease in the sensitizer content results in a 60% decrease in the heating rate. The simulation results show that $\dot{Q}_{abs\,model}$

in φ=1 and φ=0.4 samples is 8.5 and 16.8 GW/m^3 respectively, confirming that 15 wt.% increase in MnO_x accounts for doubling in the composite absorption rates. This confirms that the decrease in the sensitizer content can significantly alter the energy deposition rates. As the amount of nAl is increased and content of MnO_x is decreased to 60 wt.% the films do not reach the ignition temperature. This could mainly be due to (i) reduced overall microwave absorption capability of the composites and (ii) higher thermal conductivity of the films with increased nAl content. Combination of these factors results in a faster heat dissipation away from the irradiance zone that precludes film ignition. These effects can be clearly seen in Figures 4b-i, where at 3.2 ms the films at φ=1 have localized heat to a radial region of 20 µm while MnO_x-rich samples spanned to radial region 250 µm. Under incident microwave irradiation the critical region is getting heated but is also losing the gained heat to the surrounding microstructure and the support the film is mounted on via conduction as well as convection. As the time progresses the rate of heat gain stays the same while the thermal diffusion time allows the heat losses to become more prominent than the heat gain rate, allowing the steady-state between the rate of heat loss from the critical heating region.

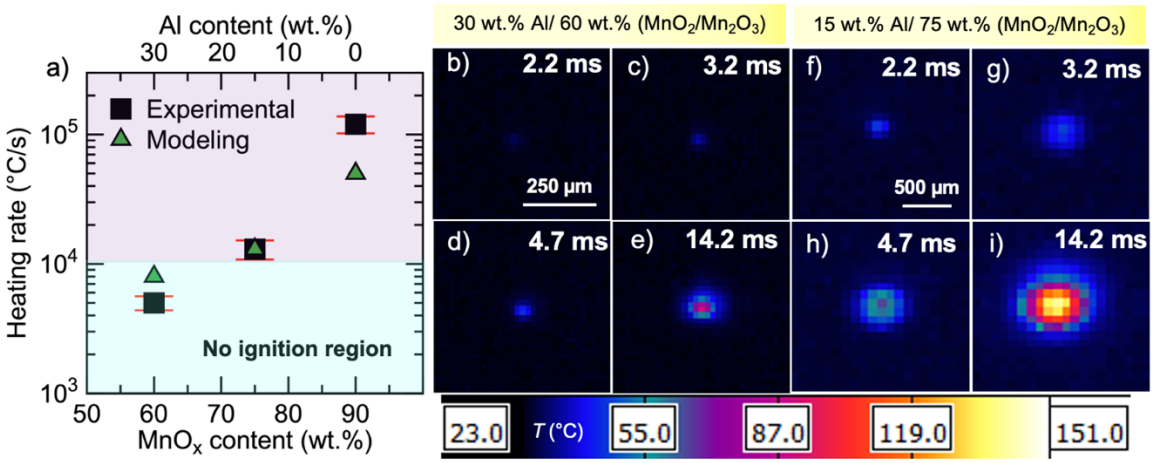

Figure 4-4. *a) Experimental and simulated microwave heating rates of the films at varying ratio of manganese oxide and nAl and fixed content of the 4 wt.% PVDF/6 wt.% HPMC binder; infrared thermal images of nAl based thermite composites at t= 2.2, 3.2, 4.7 and 14.2 ms: b – e) at 60 wt.% loading of MnO_2/Mn_2O_3 and f-i) at 75 wt.% loading of MnO_2/Mn_2O_3*

Finite element simulations of the nAl/MnO_x mixtures show that manganese oxide nanoparticles heat first under the incident wavelength and transfer heat to the neighboring aluminum nanoparticles and the polymer binder (see Figure 4-5a-e). Manganese oxide accounts for 99.4% of the absorption in the assembled energetic films and negligible absorption by nAl particles is seen. The volumetric power absorbed by MnO_x nanoparticles is in the range of 5 - 10 GW/m^3, which gives the total heat absorbed per MnO_x nanoparticle of 0.7 pW. Compared to absorption with other microwave sensitizers, such as nTi the absorption of MnO_x particles is 2 orders of magnitude lower than nTi [20], which also leads to a much longer ignition delay time for MnO_x. To better understand the thermochemistry

in fabricated nAl/MnO_x thermites, differential scanning calorimetry and T-jump ignition tests were conducted.

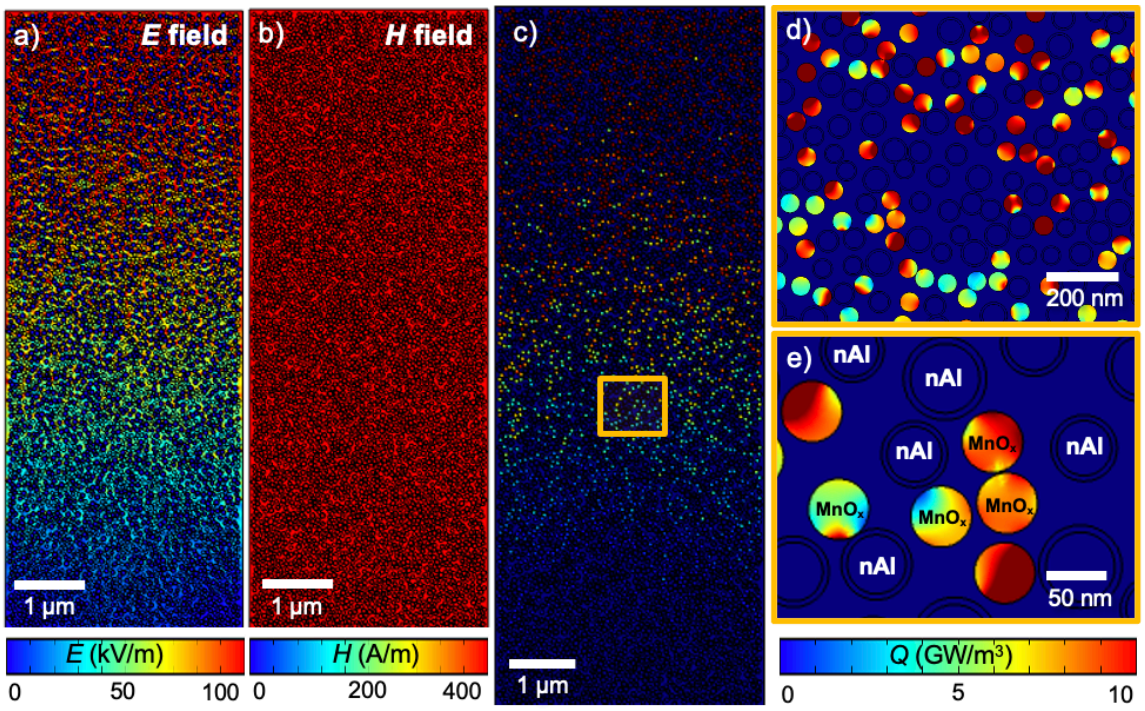

Figure 4-5. *Finite element simulation results of nAl/MnO_2/Mn_2O_3 composites at 75 wt.% MnO_2/Mn_2O_3 loading under 2.45 GHz 0.5 MV/m field strength: a) electric field distribution in the films at t = 4 ns; b) magnetic field distribution in the films at t = 1 ms; c-e) total heat absorbed by the films.*

As mentioned earlier, manganese dioxide undergoes a two-step phase change process that is accompanied by mass loss due to O_2 release (see Equations 4-1 and 4-2). Both of the phase change steps to Mn_2O_3 and Mn_3O_4 under air flow are endothermic and occur at 530°C and 920°C, respectively, as confirmed by DSC data in Figure 4-6a.

Interestingly, the second endotherm occurs at higher temperature in air than was detected in argon environment in Figure 4-2d [60]. When fabricated into a polymer binder both MnO_x and nAl/MnO_x composites do not undergo any endothermic/exothermic chemistry below 180°C. The first exotherm in the DSC plot is characteristic of exothermic decomposition of the polymer binder [61,62] with corresponding peaks at 240°C and 270°C for MnO_x and nAl/MnO_x composites, respectively. The mass loss from MnO_x/HPMC/PVDF films confirm that MnO_2 releases O_2 at 530°C, which is shortly followed by the exothermic reaction with Al [63,64]. These results are further confirmed by ultra-fast heating temperature jump ignition and mass spectrometry results presented in Figure 4-6b. Both ignition in air and argon environments occur after O_2 release from MnO_x at 620°C. The difference in O_2 release temperatures in DSC and T-jump ignition data is due to the 10^4 order of magnitude difference in heating rates [65,66]. The heating rate in T-jump experiments is at the order of 10^5 °C/s, which is closer to the observed heating rates under microwave stimulation. Numerous studies reported that oxidation of nAl proceeds when the passivating shell is compromised due to polymorphic phase changes in Al_2O_3 and diffusion of Al cations and O_2 species drives ignition [67,68]. Our results imply that the heat transfer from MnO_x particles, localized heating of nAl particles and O_2 release from the oxidizer allows ignition to occur under microwave irradiation. X-ray diffraction analysis on post-product species in air (Figure 4-8) showed traces of galaxite formation ($MnAl_2O_4$) with no traces of remnant Al, implying full consumption of the metal fuel in the reaction.

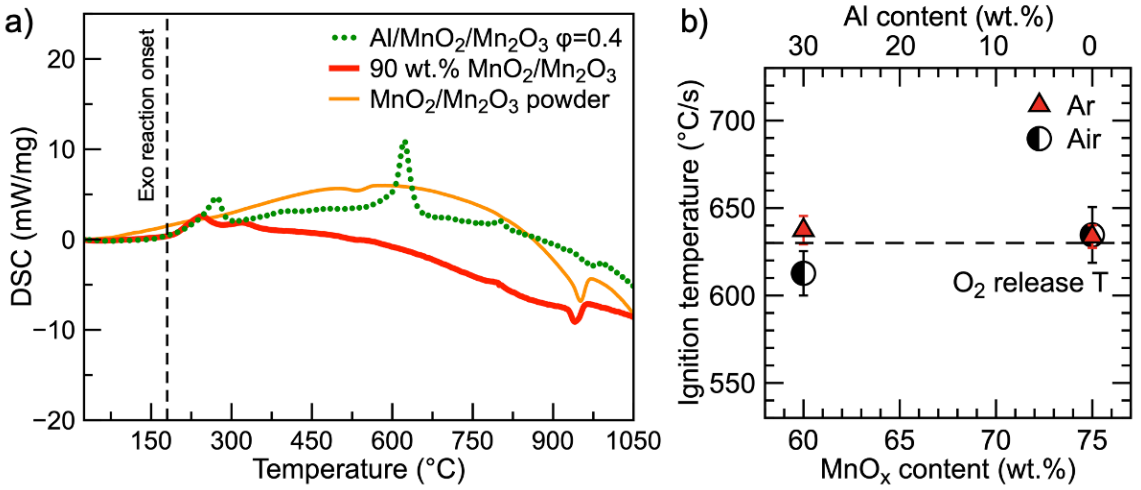

Figure 4-6. *a) DSC of $Al/MnO_2/Mn_2O_3$, MnO_2/Mn_2O_3 composites and MnO_2/Mn_2O_3 nanopowder in air; b) T-jump ignition results of $Al/MnO_2/Mn_2O_3$ energetic composites at 60 wt.% MnO_2/Mn_2O_3 loading compared against Al nanopowder results at varying O_2 pressure.*

When stimulated under EM radiation a significant factor to consider alongside microwave sensitizer content and thermochemistry that drive ignition is an energy deposition depth of the incident wave into the material volume. Finite element simulation of the films in Figure 4-7 shows that under electromagnetic stimulation at 2.45 GHz (λ = 12 cm), 564 THz (λ = 532 nm) and 282 THz (λ = 1062 nm) the nanoparticles absorb more effectively at higher energy frequencies, leading to a shorter penetration depth. Although 3D printed nAl/MnO_x composites are comprised of nanoscale constituents that have skin depths larger than their size, their assembly into microstructures at 90 wt.% nanoparticle loading enables percolating pathways within the macrostructure [69,70]. This in turn introduces screening of the incident wavelength, and the wave interaction only within the

assembled microstructure's penetration depth. Penetration depth is defined as a distance where the maximum amplitude of the incident wave decays by 63%, as it propagates into the material [57]. As seen in Equation 4-6, penetration depth in conductive materials (δ) is inversely proportional to the incident frequency (f), permeability of free space (μ_0), magnetic permeability (μ) and electrical conductivity (σ) of the sample under test. Considering the mass averaged electrical conductivity (Table 4-1) of nAl, MnO_x and the polymers the penetration depth of the films at 15 wt.% nAl content was calculated at each simulated frequency based on Equation 4-6.

$$\delta = \sqrt{\frac{2}{2\pi f \mu_0 \mu \sigma}} \tag{4-6}$$

As such, penetration depths based on macroscopic electrical conductivity of the composites were 6.7 μm, 22 nm and 16 nm at 2.45 GHz, 282 THz and 564 THz respectively. Unlike IR and visible ignition sources where absorption at high solids loading is limited to nanoscale depth heating, microwave absorption is not limited by a narrow penetration depth for conductive composites. Figure 4-7a demonstrates the heating in the printed samples under incident radiation at 2.45 GHz where deposited electric field drops with the depth of the film from a maximum value of 300 kV/m to about 110 kV/m in 6 μm. In contrast, at 532 nm and 1064 nm the electric field decreases rapidly within nanometer scale and no electric field can be deposited beyond 500 nm depth (see Figure 4-7b and Figure 4-7c). Furthermore, and from a practical standpoint, the ability to print suggests the ability

to embed MW sensitizers within the body of a structure to initiate chemistry in a desired location.

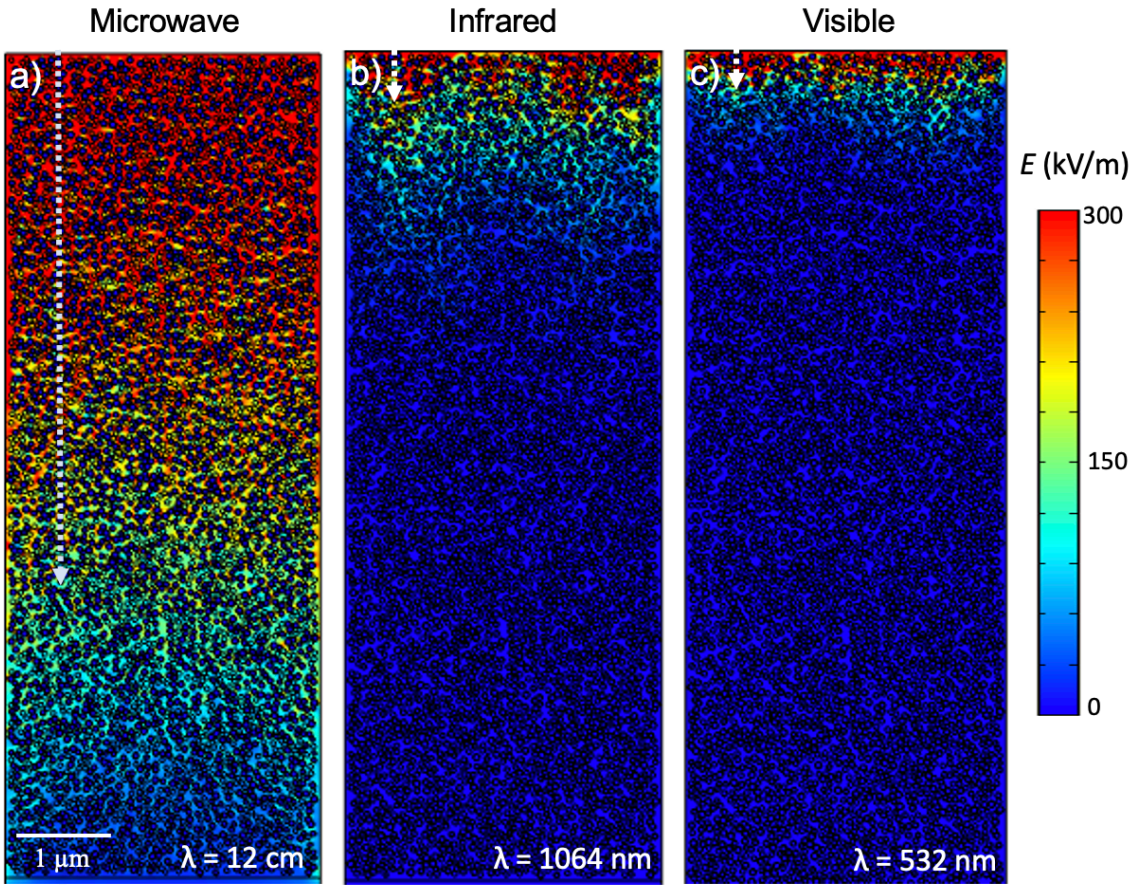

Figure 4-7. *Electric field induced in the matrix of 15 wt.% Al/ 75 wt.% (MnO_2/Mn_2O_3) films at incident wavelengths of a) 12 cm and b) 1064 nm and c) 532 nm (from left to right)*

4.5 Conclusion

In the presence of nanoscale MnO_x, otherwise inert nAl based energetic composites can be ignited under EM stimulation at 2.45 GHz. At 90 wt.% MnO_x loading, the composites rapidly heat via electric field absorption at 10^5 °C/s. The experimental infrared

thermometry coupled with finite element simulations showed that MnO_x nanoparticles effectively heat under the microwave irradiation and transfer heat to the surrounding nAl particles. In-situ TOFMS T-jump ignition results showed that O_2 release from MnO_2, present in the oxidizer, triggers the ignition in the energetic composites of nAl/MnO_x. These results demonstrate that MnO_x nanoparticles not only absorb microwave energy and transfer heat to the surrounding media but also control the ignition onset in the presented energetic composites.

4.6 Supplemental Information

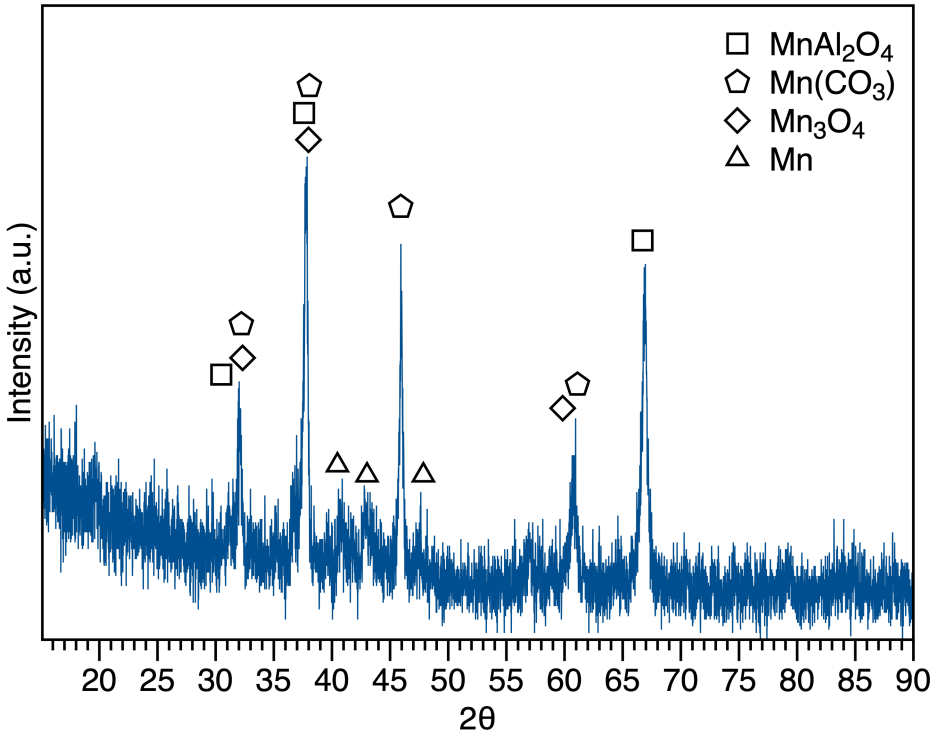

Figure 4-8. *X-ray diffraction analysis on combustion post-products of Al/MnOx/PVDF/HPMC in air at 60 wt.% loading of MnO_x.*

4.7 References

[1] L. Wang, Z. Munir, Y. Maximov, Review of Thermite Reactions: their utilization in the synthesis and processing of materials, J. Mater. Sci. 28 (1993) 3693–3708.

[2] M.R. Weismiller, J.Y. Malchi, J.G. Lee, R.A. Yetter, T.J. Foley, Effects of fuel and oxidizer particle dimensions on the propagation of aluminum containing thermites, Proc. Combust. Inst. 33 (2011) 1989–1996. https://doi.org/10.1016/j.proci.2010.06.104.

[3] J.T. Koenig, A.P. Shaw, J.C. Poret, W.S. Eck, L.J. Groven, Performance of W/MnO2 as an Environmentally Friendly Energetic Time Delay Composition, ACS Sustain. Chem. Eng. 5 (2017) 9477–9484. https://doi.org/10.1021/acssuschemeng.7b02579.

[4] M.L. Pantoya, J.J. Granier, Combustion behavior of highly energetic thermites: Nano versus micron composites, Propellants, Explos. Pyrotech. 30 (2005) 53–62. https://doi.org/10.1002/prep.200400085.

[5] C.E. Aumann, G.L. Skofronick, J.A. Martin, Oxidation behavior of aluminum nanopowders, J. Vac. Sci. Technol. B Microelectron. Nanom. Struct. 13 (1995) 1178–1183. https://doi.org/10.1116/1.588232.

[6] C. Rossi, Two decades of research on nano-energetic materials, Propellants, Explos. Pyrotech. 39 (2014) 323–327. https://doi.org/10.1002/prep.201480151.

[7] H. Wang, G. Jian, S. Yan, J.B. Delisio, C. Huang, M.R. Zachariah, Electrospray formation of gelled nano-aluminum microspheres with superior reactivity, ACS Appl. Mater. Interfaces. 5 (2013) 6797–6801. https://doi.org/10.1021/am401238t.

[8] H. Wang, D.J. Kline, M. Rehwoldt, T. Wu, W. Zhao, X. Wang, M.R. Zachariah, Architecture Can Significantly Alter the Energy Release Rate from Nanocomposite Energetics, ACS Appl. Polym. Mater. 1 (2019) 982–989. https://doi.org/10.1021/acsapm.9b00016.

[9] T. Calais, A. Bancaud, A. Estève, C. Rossi, Correlation between DNA Self-Assembly Kinetics, Microstructure, and Thermal Properties of Tunable Highly Energetic Al-CuO Nanocomposites for Micropyrotechnic Applications, ACS Appl. Nano Mater. 1 (2018) 4716–4725. https://doi.org/10.1021/acsanm.8b00939.

[10] V.A. Arkhipov, A.G. Korotkikh, The influence of aluminum powder dispersity on composite solid propellants ignitability by laser radiation, Combust. Flame. 159 (2012) 409–415. https://doi.org/10.1016/j.combustflame.2011.06.020.

[11] N.K. Bourne, On the laser ignition and initiation of explosives, Proc. R. Soc. A

Math. Phys. Eng. Sci. 457 (2001) 1401–1426. https://doi.org/10.1098/rspa.2000.0721.

[12] S. Huang, V.S. Parimi, S. Deng, S. Lingamneni, X. Zheng, Facile Thermal and Optical Ignition of Silicon Nanoparticles and Micron Particles, Nano Lett. 17 (2017) 5925–5930. https://doi.org/10.1021/acs.nanolett.7b01754.

[13] D.K. Agrawal, Microwave processing of ceramics, Curr. Opin. Solid State Mater. Sci. 3 (1998) 480–485. https://doi.org/10.1016/S1359-0286(98)80011-9.

[14] W.H. Sutton, Microwave processing of materials, MRS Bull. 18 (1993) 22–29. https://doi.org/10.1017/S0883769400038495.

[15] X. Fang, S. R. Ahmad, Laser ignitability of insensitive propellants, Adv. Mater. Sci. 3 (2018) 1–4. https://doi.org/10.15761/ams.1000139.

[16] S.R. Ahmad, D.A. Russell, Laser ignition of pyrotechnics - Effects of wavelength, composition and confinement, Propellants, Explos. Pyrotech. 30 (2005) 131–139. https://doi.org/10.1002/prep.200400095.

[17] K.E. Uhlenhake, D. Olsen, M. Gomez, M. Örnek, M. Zhou, S.F. Son, Photoflash and laser ignition of full density nano-aluminum PVDF films, Combust. Flame. 233 (2021) 111570. https://doi.org/10.1016/j.combustflame.2021.111570.

[18] S.J. Barkley, K. Zhu, J.E. Lynch, J.B. Michael, T.R. Sippel, Microwave plasma enhancement of multiphase flames: On-demand control of solid propellant burning rate, Combust. Flame. 199 (2019) 14–23. https://doi.org/10.1016/j.combustflame.2018.10.007.

[19] K. Zhu, S.J. Barkley, T.R. Sippel, J.B. Michael, Flame temperature characterization of microwave-assisted aluminum particle combustion, AIAA Scitech 2019 Forum. (2019) 1–10. https://doi.org/10.2514/6.2019-0834.

[20] Z. Alibay, D.J. Kline, M.C. Rehwoldt, P. Biswas, S. Herrera, H. Wang, M.R. Zachariah, Mechanism of microwave-initiated ignition of sensitized energetic nanocomposites, Chem. Eng. J. 415 (2021) 128657. https://doi.org/10.1016/j.cej.2021.128657.

[21] A. Porch, D. Slocombe, P.P. Edwards, Microwave absorption in powders of small conducting particles for heating applications, Phys. Chem. Chem. Phys. 15 (2013) 2757–2763. https://doi.org/10.1039/c2cp43310a.

[22] P. Biswas, G.W. Mulholland, M.C. Rehwoldt, D.J. Kline, M.R. Zachariah, Microwave absorption by small dielectric and semi-conductor coated metal particles, J. Quant. Spectrosc. Radiat. Transf. 247 (2020) 106938.

https://doi.org/10.1016/j.jqsrt.2020.106938.

[23] D.J. Kline, M.C. Rehwoldt, C.J. Turner, P. Biswas, G.W. Mulholland, S.M. Mcdonnell, M.R. Zachariah, Spatially focused microwave ignition of metallized energetic materials, J. Appl. Phys. 055901 (2020). https://doi.org/10.1063/1.5134089.

[24] V.E. Sanders, B.W. Asay, T.J. Foley, B.C. Tappan, A.N. Pacheco, S.F. Son, Reaction Propagation of Four Nanoscale Energetic Composites (Al/MoO3, Al/WO3, Al/CuO, and B12O3), J. Propuls. Power. 23 (2007) 707–714. https://doi.org/10.2514/1.26089.

[25] J.J. Granier, K.B. Plantier, M.L. Pantoya, The role of the Al2O3 passivation shell surrounding nano-Al particles in the combustion synthesis of NiAl, J. Mater. Sci. 39 (2004) 6421–6431. https://doi.org/10.1023/B:JMSC.0000044879.63364.b3.

[26] M. Comet, C. Martin, F. Schnell, D. Spitzer, Nanothermites: a short review. Factsheet for experimenters, present and future challenges, Propellants, Explos. Pyrotech. 44 (2019) 18–36. https://doi.org/10.1002/prep.201800095.

[27] S. Fischer, M. Grubelich, Theoretical energy release of thermites, intermetallics, and combustible metals, in: 24th Int. Pyrotech. Semin., 1998: p. 56. http://journals.pepublishing.com/openurl.asp?genre=article&id=doi:10.1243/09544097F01505.

[28] G. Jian, N.W. Piekiel, M.R. Zachariah, Time-resolved mass spectrometry of nano-Al and nano-Al/CuO thermite under rapid heating: A mechanistic study, J. Phys. Chem. C. 116 (2012) 26881–26887. https://doi.org/10.1021/jp306717m.

[29] C.A. Crane, M.L. Pantoya, B.L. Weeks, Investigating the trade-offs of microwave susceptors in energetic composites: Microwave heating versus combustion performance, J. Appl. Phys. 115 (2014). https://doi.org/10.1063/1.4868337.

[30] Y. Meir, E. Jerby, Localized rapid heating by low-power solid-state microwave drill, IEEE Trans. Microw. Theory Tech. 60 (2012) 2665–2672. https://doi.org/10.1109/TMTT.2012.2198233.

[31] E. Vargas, M.L. Pantoya, M.A. Saed, B.L. Weeks, Advanced susceptors for microwave heating of energetic materials, Mater. Des. 90 (2016) 47–53. https://doi.org/10.1016/j.matdes.2015.10.110.

[32] S.J. Barkley, A.R. Lawrence, M. Zohair, O.L. Smithhisler, C.L. Pint, J.B. Michael, T.R. Sippel, Smart Electromagnetic Thermites: GO/rGO Nanoscale Thermite Composites with Thermally Switchable Microwave Ignitability, ACS Appl. Mater. Interfaces. 13 (2021) 39678–39688. https://doi.org/10.1021/acsami.1c04476.

[33] S. Jiaxing, G. Tao, D. Wen, M. Yiming, F. Xiang, W. Hao, Study on Thermal Chemical Reaction of Al/MnO2 Thermite, IOP Conf. Ser. Earth Environ. Sci. 186 (2018). https://doi.org/10.1088/1755-1315/186/2/012046.

[34] J. Song, T. Guo, M. Yao, J. Chen, W. Ding, F. Bei, Y. Mao, Z. Yu, J. Huang, X. Zhang, Q. Yin, S. Wang, A comparative study of thermal kinetics and combustion performance of Al/CuO, Al/Fe2O3 and Al/MnO2 nanothermites, Vacuum. 176 (2020) 109339. https://doi.org/10.1016/j.vacuum.2020.109339.

[35] J. Song, T. Guo, W. Ding, M. Yao, L. Yang, X. Zhang, Z. Yu, J. Wu, J. Zhang, X. Fang, The Effect of Al Particles Size on the Thermal Behavior and Kinetics of Al-MnO2 Thermite System, Adv. Mater. Sci. Eng. 2020 (2020) 1–11.

[36] D.R. Baghurst, D.M.P. Mingos, Application of microwave heating techniques for the synthesis of solid state inorganic compounds, J. Chem. Soc. Chem. Commun. (1988) 829–830. https://doi.org/10.1039/C39880000829.

[37] E. Vileno, H. Zhou, Q. Zhang, S.L. Suib, D.R. Corbin, T.A. Koch, Synthetic todorokite produced by microwave heating: An active oxidation catalyst, J. Catal. 187 (1999) 285–297. https://doi.org/10.1006/jcat.1999.2639.

[38] C. Marún, Catalytic oligomerization of methane via microwave heating, J. Phys. Chem. A. 103 (1999) 4332–4340. https://doi.org/10.1021/jp984671j.

[39] X. Wang, G. Lv, L. Liao, G. Wang, Manganese oxide - an excellent microwave absorbent for the oxidation of methylene blue, RSC Adv. 5 (2015) 55595–55601. https://doi.org/10.1039/c5ra08486e.

[40] H. Guan, S. Liu, Y. Zhao, Y. Duan, Electromagnetic characteristics of nanometer manganese dioxide composite materials, J. Electron. Mater. 35 (2006) 892–896. https://doi.org/10.1007/BF02692544.

[41] Y. Duan, Z. Liu, H. Jing, K. Yin, S. Liu, The effects of annealing treatment on the morphology and microwave absorption properties of α-MnO2, Proc. Inst. Mech. Eng. Part L J. Mater. Des. Appl. 227 (2013) 61–69. https://doi.org/10.1177/1464420712450813.

[42] COMSOL Multiphysics, (n.d.).

[43] C.A. Crane, M.L. Pantoya, B.L. Weeks, M. Saed, The effects of particle size on microwave heating of metal and metal oxide powders, Powder Technol. 256 (2014) 113–117. https://doi.org/10.1016/j.powtec.2014.02.008.

[44] W. Zhou, J. Zuo, W. Ren, Thermal conductivity and dielectric properties of Al/PVDF composites, Compos. Part A Appl. Sci. Manuf. 43 (2012) 658–664.

https://doi.org/10.1016/j.compositesa.2011.11.024.

[45] X.M. Meng, X.J. Zhang, C. Lu, Y.F. Pan, G.S. Wang, Enhanced absorbing properties of three-phase composites based on a thermoplastic-ceramic matrix (BaTiO3 + PVDF) and carbon black nanoparticles, J. Mater. Chem. A. 2 (2014) 18725–18730. https://doi.org/10.1039/c4ta04493b.

[46] D. Yuping, M. He, L. Xiaogang, L. Shunhua, J. Zhijiang, The microwave electromagnetic characteristics of manganese dioxide with different crystallographic structures, Phys. B Condens. Matter. 405 (2010) 1826–1831. https://doi.org/10.1016/j.physb.2010.01.055.

[47] M. Hedden, N. Francis, J.T. Haraldsen, T. Ahmed, C. Constantin, Thermoelectric properties of nano-meso-micro β-MnO2 powders as a function of electrical resistance, Nanoscale Res. Lett. 10 (2015). https://doi.org/10.1186/s11671-015-1000-6.

[48] K.T. Jacob, A. Kumar, G. Rajitha, Y. Waseda, Thermodynamic data for Mn 3O 4, Mn 2O 3 and MnO 2, High Temp. Mater. Process. 30 (2011) 459–472. https://doi.org/10.1515/HTMP.2011.069.

[49] L. Zhou, N. Piekiel, S. Chowdhury, M.R. Zachariah, Time-resolved mass spectrometry of the exothermic reaction between nanoaluminum and metal oxides: The role of oxygen release, J. Phys. Chem. C. 114 (2010) 14269–14275. https://doi.org/10.1021/jp101146a.

[50] M.C. Falub, K. Kuepper, X-ray photoelectron spectra of manganites were studied. It was shown that for the formal valence of manganese from 3+ to 3.3+, the doping holes are O2, 49 (2008) 54–58.

[51] V.R. Galakhov, M. Demeter, S. Bartkowski, M. Neumann, N.A. Ovechkina, E.Z. Kurmaev, N.I. Lobachevskaya, Y.M. Mukovskii, J. Mitchell, D.L. Ederer, Mn (formula presented) exchange splitting in mixed-valence manganites, Phys. Rev. B - Condens. Matter Mater. Phys. 65 (2002) 1–4. https://doi.org/10.1103/PhysRevB.65.113102.

[52] A.G. Kochur, A.T. Kozakov, A. V. Nikolskii, K.A. Googlev, A. V. Pavlenko, I.A. Verbenko, L.A. Reznichenko, T.I. Krasnenko, Valence state of the manganese ions in mixed-valence La 1-αBi βMn 1+δO 3±γ ceramics by Mn 2p and Mn 3s X-ray photoelectron spectra, J. Electron Spectros. Relat. Phenomena. 185 (2012) 175–183. https://doi.org/10.1016/j.elspec.2012.06.017.

[53] I.A. Reyes, M. Flores, E.G. Palacios, H. Islas, J.C. Juárez, M. Reyes, A.M. Teja, C.A. Pérez, Kinetics of the thermal decomposition of rhodochrosite, Minerals. 11 (2020) 1–13. https://doi.org/10.3390/min11010034.

[54] E. Jerby, V. Dikhtyar, The microwave drill, Science. 298 (2002) 587–589.

[55] E. Jerby, O. Aktushev, V. Dikhtyar, Theoretical analysis of the microwave-drill near-field localized heating effect, J. Appl. Phys. 97 (2005). https://doi.org/10.1063/1.1836011.

[56] Y. Meir, E. Jerby, Thermite powder ignition by localized microwaves, Combust. Flame. 159 (2012) 2474–2479. https://doi.org/10.1016/j.combustflame.2012.02.015.

[57] S. Horikoshi, R.F. Schiffmann, J. Fukushima, N. Serpone, Microwave chemical and materials processing: A tutorial, 2017. https://doi.org/10.1007/978-981-10-6466-1.

[58] J. Zhang, D. Yuping, L. Shuqing, L. Xiaogang, L. Shunhua, The effects of high magnetic field on the morphology and microwave electromagnetic properties of MnO2 powder, J. Solid State Chem. 183 (2010) 1490–1495. https://doi.org/10.1016/j.jssc.2010.04.027.

[59] K.I. Rybakov, V.E. Semenov, S. V. Egorov, A.G. Eremeev, I. V. Plotnikov, Y. V. Bykov, Microwave heating of conductive powder materials, J. Appl. Phys. 99 (2006) 023506. https://doi.org/10.1063/1.2159078.

[60] D.M. Tinsley, J.H. Sharp, THERMAL ANALYSIS OF MANGANESE DIOXIDE IN CONTROLLED ATMOSPHERES, J. Therm. Anal. 3 (1971) 43–48.

[61] X.G. Li, M.R. Huang, H. Bai, Thermal decomposition of cellulose ethers, J. Appl. Polym. Sci. 73 (1999) 2927–2936. https://doi.org/10.1002/(SICI)1097-4628(19990929)73:14<2927::AID-APP17>3.0.CO;2-K.

[62] J.B. Delisio, X. Hu, T. Wu, G.C. Egan, G. Young, M.R. Zachariah, Probing the Reaction Mechanism of Aluminum/Poly(vinylidene fluoride) Composites, J. Phys. Chem. B. 120 (2016) 5534–5542. https://doi.org/10.1021/acs.jpcb.6b01100.

[63] J. Zhang, J. Huang, X. Fang, Y. Li, Z. Yu, Z. Gao, S. Wu, L. Yang, J. Wu, J. Kui, Thermal decomposition and thermal reaction process of PTFE/Al/MnO2 fluorinated thermite, Materials (Basel). 11 (2018). https://doi.org/10.3390/ma11122451.

[64] J. Song, T. Guo, W. Ding, M. Yao, F. Bei, X. Zhang, J. Huang, X. Fang, Study on thermal behavior and kinetics of Al/MnO2 poly(vinylidene fluorine) energetic nanocomposite assembled by electrospray, RSC Adv. 9 (2019) 25266–25273. https://doi.org/10.1039/c9ra04425f.

[65] R.A. Williams, J. V. Patel, A. Ermoline, M. Schoenitz, E.L. Dreizin, Correlation of optical emission and pressure generated upon ignition of fully-dense nanocomposite thermite powders, Combust. Flame. 160 (2013) 734–741.

https://doi.org/10.1016/j.combustflame.2012.11.021.

[66] G. Jian, L. Zhou, N.W. Piekiel, M.R. Zachariah, Low effective activation energies for oxygen release from metal oxides: Evidence for mass-transfer limits at high heating rates, ChemPhysChem. 15 (2014) 1666–1672. https://doi.org/10.1002/cphc.201301148.

[67] M.A. Trunov, M. Schoenitz, E.L. Dreizin, Effect of polymorphic phase transformations in alumina layer on ignition of aluminium particles, Combust. Theory Model. 10 (2006) 603–623. https://doi.org/10.1080/13647830600578506.

[68] S. Chowdhury, K. Sullivan, N. Piekiel, L. Zhou, M.R. Zachariah, Diffusive vs explosive reaction at the nanoscale, J. Phys. Chem. C. 114 (2010) 9191–9195. https://doi.org/10.1021/jp906613p.

[69] L. Yang, Q. Zhao, Y. Hou, R. Sun, M. Cheng, M. Shen, S. Zeng, H. Ji, J. Qiu, High breakdown strength and outstanding piezoelectric performance in flexible PVDF based percolative nanocomposites through the synergistic effect of topological-structure and composition modulations, Compos. Part A Appl. Sci. Manuf. 114 (2018) 13–20. https://doi.org/10.1016/j.compositesa.2018.07.039.

[70] L. Zhang, W. Wang, X. Wang, P. Bass, Z.Y. Cheng, Metal-polymer nanocomposites with high percolation threshold and high dielectric constant, Appl. Phys. Lett. 103 (2013). https://doi.org/10.1063/1.4838237.

5 Experimental Observation of the Heat Transfer Mechanisms that Drive Propagation in Additively Manufactured Energetic Materials[1]

5.1 Summary

The rise of additive manufacturing has led to the development of new architectures and allowed researchers to 3D-print a variety of energetic composites with different formulations. However, reactive sintering within the composites can negatively impact overall performance of nanoenergetic or reactive materials via the loss of nanostructure. It has been previously proposed that the addition of a gas generator could reduce the impact of reactive sintering while enhancing reactivity. Iodine pentoxide (I_2O_5) is an extremely powerful oxidizer and a strong gas generator which has been proposed as an efficient source of molecular iodine for biocidal applications. However, fabricated Al/I_2O_5 nanocomposite propellants are unable to propagate. In this study, we demonstrate that the addition of small quantities of CuO enables consistent propagation. Employing high-speed pyrometry and microscopy, we estimate advective heat transfer in the system and demonstrate that the addition of CuO offers a pathway for enhanced energy-transfer by metal condensation that is not available when I_2O_5 is the sole oxidizer. Elimination of condensing metal vapor as a participant in energy transfer increased the reliance of the system on particle advection. Small additions of CuO yield a condensable product vapor which can effectively eliminate the reliance on heat transfer via advection, enabling consistent propagation in reactive solid materials. We conclude with a general comment

that where reliable propagation is critical, such as a stable burn of a solid propellant or delivery of a biocide, small additions of an oxidizer with a condensable metal vapor could be the difference between guaranteed performance and critical failure.

┴The findings presented in this chapter have been previously published and are reprinted with permission from: Dylan J. Kline*, Zaira Alibay*, Miles C. Rehwoldt, Alexander Idrogo-Lam, Spencer G. Hamilton, Prithwish Biswas, Feiyu Xu, and Michael R. Zachariah. "Experimental observation of the heat transfer mechanisms that drive propagation in additively manufactured energetic materials." *Combustion and Flame* 215 (2020): 417-424. Copyright 2020 Elsevier. *Co-first authors

5.2 Introduction

Thermites (or reactive materials) are a subclass of energetic materials that participate in a highly exothermic redox reaction and have been traditionally prepared using a mixture of metals and metal oxides [1,2]. Compared to organic, monomolecular explosives, thermite reactants have a higher energy density because the enthalpy of formation for solid products is substantially lower than the gaseous products of organic explosives (whose primary products are CO_2 and water) [1–4]. However, thermites have been traditionally mixed using micron powders which have large diffusion distances between the fuels and oxidizers and thus have much slower reactions than explosives [5]. Recent research in thermites has centered around the use of nanoparticles as the fuel and oxidizer to increase the burn rate [1,5–8] and the rise of additive manufacturing has opened new avenues by which to architecture [9–13] these materials for applications in high energy-density solid propellants.

Nanothermites have also been investigated as a biocide delivery mechanism for defense against the threat of bioweapons [14–16]. Iodine-containing compounds have received the widest attention as a readily-available biocidal additive to reactive materials due to the effectiveness of molecular iodine at killing spores [14–19]. Numerous studies have focused on the incorporation of iodine pentoxide (I_2O_5) into a variety of nanothermites as both the oxidizer and iodine carrier where it has been found that the combustion performance in a constant-volume cell is superior to metal/metal oxide mixtures, likely due to the large amount of gas generated as part of the reaction [15,20,21]. Other studies have

investigated the incorporation of iodine into the oxide shell of the metal fuel particles to further enhance reactant mixing and improve performance [17,18].

Gas-producing oxidizers, such as I_2O_5 and CuO, also offer a unique advantage over the strictly condensed-phase oxidizers since they reduce reactive sintering during the thermite reaction – a phenomenon that results in the loss of nanostructure during reaction and can arrest reactions prematurely [22–25]. By introducing a gas generator that also serves as an oxidizer for the mixture, agglomeration of particles is reduced. Furthermore, the gas release would also likely increase the heat transfer via advection to unreacted areas of the propellant – a critical mechanism of heat transfer for sustained propagation in energetic materials as described by Egan et al. [26]. However, Egan et al. also demonstrated that condensing metal vapor could contribute more than enough energy to sustain combustion, but it is estimated that only ~15% of the energy used for ignition is from product condensation and ~50% is from advective heat transfer in a modeled burn tube experiment [26]. Certainly, advection would be enhanced in the case of I_2O_5 oxidizer over other metal oxides because of its considerably higher gas production, though it is unclear whether the increase in gas production could offset the energy lost in systems that totally lack the recondensing metal vapor.

This work investigates the role of different heat transfer mechanisms that facilitate propagation in solid propellants to improve combustion performance without compromising reliability. Propagation of the reaction front is observed at the microscale for high-loading, additively manufactured energetic materials to estimate the impact of gas release, advection, and metal vapor condensation on combustion performance and stability.

It was found that, while gas generation in the Al/I_2O_5 reaction reduced reactive sintering, the printed material was unable to consistently propagate, likely attributable to the lack of condensing metal vapor products that would provide heat feedback for propagation. However, small additions of CuO to the sample improved the propagation reliability without significant impacts on the reactive sintering, thus revealing the fine balance between gas generation and heat transfer as tuning mechanisms for performance in solid energetic materials.

5.3 Methods

5.3.1 Chemicals

METHOCEL F4M hydroxypropyl methylcellulose (HPMC) was ordered from Dow Chemical Company. Poly(vinylidene fluoride) (PVDF, molecular weight: ≈534,000), N,N dimethylformamide (DMF, 99.8%) and Iodine Pentoxide (I_2O_5) were purchased from Sigma-Aldrich. CuO nanoparticles (d≈40 nm) were purchased from US Research Nanomaterials. Aluminum nanoparticles (Al NPs, ≈85 nm) were purchased from Novacentrix. The active aluminum content is ≈ 81 wt% according to thermogravimetry/differential scanning calorimetry (TGA/DSC) results. I_2O_5 crystals were purchased from Sigma Aldrich (99.9% purity). The crystals were heated in a tube furnace at 300°C for 2 hours, then ball-milled (Retsch Cryomill) with 5/32" steel balls in hexane for 2 hours to prevent moisture uptake. The powder was stored in a low-humidity environment and reheated in a tube furnace at 300°C for 1 hour immediately prior to ink preparation.

5.3.2 Precursor Preparation

Inks for 3D-printing of burn sticks were prepared by first mixing 50mg PVDF and 75mg HPMC in 4mL of DMF for 30 minutes at 2000 rpm in a planetary centrifugal mixer (Thinky USA). The Al NPs were then added to the polymer solution and dispersed by ultrasonication for 35 minutes. After the dispersion of the Al NPs, the mixture was mixed in the Thinky Mixer again at 2000 rpm on the mixing mode for 5 minutes and placed in the sonicator for an additional 35 minutes. This process of addition, dispersion by ultrasonication, and mixing was repeated for the CuO NPs and I_2O_5.

Mixture formulations for the thermites added to the PVDF/HPMC mixture were calculated for the stoichiometric reaction between active fuel and solid oxidizer, whereby the oxidizer content was varied by small additions of CuO. The amount of CuO added was determined by assuming that a percentage of the active fuel was reacting with different oxidizers. Table 5-1 shows the formulations for the different precursors where the Al wt.% includes the mass of the Al_2O_3 shell. Experiments were only performed on mixtures containing up to 25% CuO to retain the primarily biocidal properties of the I_2O_5 mixture.

Formulations are named by the theoretical percentage of Al that would react with the different oxidizers. For example, in the Al/75% I_2O_5/25% CuO sample, 75% of the available aluminum would stoichiometrically react with the I_2O_5 and the remaining 25% of Al would react with CuO. Mixture formulations did not consider the stoichiometry of the samples including the fluoropolymer binder, therefore the overall sample stoichiometry is slightly fuel-lean (Φ~0.92-0.93).

Table 5-1. *Mixture formulations of thermites added to PVDF/HPMC ink. Al wt.% includes the mass of Al_2O_3 shell.*

Oxidizer (% Al reacting with I_2O_5)	Al (wt. %)	I_2O_5 (wt. %)	CuO (wt. %)
100%	25%	75%	0%
95%	25%	71%	4%
75%	25%	54%	22%

5.3.3 Direct-Writing of Burn Sticks

Burn sticks were fabricated using a Hyrel System 30M printer with a heating stage. The precursor was loaded in a 30 mL syringe with a needle size of 18 gauge (inner diameter 1 mm). The heating stage was topped with a glass, microscope coverslips (VWR 0.17mm thickness, 22mm square) and heated to ≈70°C before printing to ensure total solvent evaporation before deposition of another layer. The width of the deposited sticks was kept at 2 mm by employing an 18 gauge needle [11]. The printer was programmed to write 14 layers, resulting in a thickness range of 388-450 µm per burn stick. The thickness and cross-sectional area of the final products were measured by scanning electron microscopy (SEM). Density of the final products was estimated by using the measured mass and volume of the burn sticks. Porosity was calculated by using the measured and theoretical density values of the composites. The results are tabulated in Table 5-4.

5.3.4 Macro-Scale Burn Tests

To evaluate the combustion performance of the prepared materials on the macro-scale, as-printed samples were removed from the surface of the microscope coverslips to

propagate as a free-standing propellant. The burn performance apparatus is a glass cylinder with rubber stops at each end for atmosphere control and electrical throughputs for combustion initiation. Evenly-spaced metal plates around the glass tube are used for pixel/distance ratio calculations for flame speed analysis. The free-standing films are mounted on one end between a braided nichrome wire and double-sided tape on the other end. The wire is resistively heated to ignite the sample, and the combustion event recorded using a high-speed camera (Phantom Miro M110) recording at 4,000 frames/s. Burn rate is calculated by tracking the distance that the reaction front moves as a function of time. The burn rate for samples that did not consistently propagate was measured for the period of time that a stable burn was sustained. All experiments were performed in a constant-pressure air atmosphere.

5.3.5 High Speed In-Operando Microscopy/Thermometry and Particle Tracking

Sample combustion was also observed using a custom-built high-speed microscopy apparatus that allows for reaction front imaging at μm and μs resolution.[25] The glass coverslips on which the samples are printed are mounted on a 3-axis translational stage, brought into focus, and ignited using a resistively heated nichrome wire along one edge. Propagation of the reaction front is then captured using a high-speed camera (Phantom VEO710L) that is coupled to a long-distance microscope (Infinity Photo-Optical Model K2 DistaMax). The apparatus provides a pixel/distance ratio of ~1.7 μm/pixel from a working distance of ~54 mm. Videos of the reaction propagation were recorded at 14,000-18,000 frames/s.

The high-speed microscope apparatus has also been calibrated for color pyrometry to estimate the temperature of the reaction. Color pyrometry has been discussed in other articles and is only briefly described here [24]. Three channel intensity ratios are used to estimate the temperature of materials based upon the theoretical intensity for the sensor assuming graybody emission behavior of the material. Calibration factors for the assembly are determined for the assembly by comparing the theoretical response (estimated using Planck's Law and the response spectrum of the CMOS sensor) to actual response when observing a blackbody source (Mikron M390). The calibration curve for this assembly can be seen in Figure 5-5. Prior to temperature calculations, the raw images are imported using a house-built MATLAB routine and demosaiced for the camera's Bayer filter using the built-in MATLAB algorithms [27]. For these videos, the error threshold was increased to a maximum error of 400K, however, the error is nominally 200K.

Particle tracking and estimated particle velocities of advecting materials produced by the reaction were estimated using the pixel/distance ratios and exposure times of the images for each video.

5.3.6 Morphology Characterization

Scanning electron microscopy (SEM) was performed on as-prepared samples and post-combustion products to evaluate the morphology. A FEI NNS450 SEM and an energy-dispersive X-ray spectroscopy (EDX) probe were used to observe the sectioned samples and construct elemental maps of samples that were mounted with carbon tape to SEM stages.

5.4 Results

5.4.1 Materials

Prior to combustion experiments, it was important to verify that the materials being prepared retained the properties of the original reactants – especially I_2O_5. I_2O_5 has been known to absorb water, in which case its crystal structure changes to that of HI_3O_8. The as-purchased I_2O_5 crystals were substantially larger than the nanometal additives and contained small amounts of HI_3O_8 [28]. Therefore, crystals were dried in a furnace and ball-milled in hexane to prevent moisture uptake. This reduced the final size of the particles to ~ 2-4 µm crystals, as shown in Figure 5-6 and prevented moisture uptake [28].

An example image of the as-prepared films can be seen in Figure 5-6 for the original I_2O_5 crystals, Al/I_2O_5, and Al/75% I_2O_5/25% CuO burn sticks. The images show that the I_2O_5 crystals were reduced in size from ~25-100µm to ~2-10 µm crystal domains that can be seen extending from the surface of the material. Despite the size reduction for the I_2O_5 crystals, the Al and CuO primary particles are still substantially smaller (~50-80nm) in comparison. The final films are also porous primarily due to the theoretical maximum packing density of the particle aggregates and evaporation of the DMF solvent used for the ink during the printing process [11,29,30]. To further reduce the likelihood that the samples reabsorbed any water and eliminate any remaining solution, the samples were placed on a hot plate at 100°C prior to preparation and were stored in a desiccator if not used immediately. The sample moisture content up until the time of the experiments was considered minimal but was not directly measured [31].

5.4.2 Macro-Scale Burn Tests

Free-standing Al/I_2O_5 high-loading burn sticks would consistently ignite but would fail to propagate to completion – a peculiar result for a mixture that nominally should have excellent performance because of its enhanced gas generation, high adiabatic flame temperature, and low ignition temperature. Egan et al. detailed the role of different heat transfer mechanisms on propagation in reactive materials that were packed into constant volume burn tubes [26]. The major result was that, while convection played a significant role on heat transfer for propagation, the presence of condensed metal vapor in the products was a comparable contributor. In the case detailed here (Al/I_2O_5), heat transfer via condensation is not as significant since Al_2O_3 is not formed from the vapor and I_2 has a small heat of condensation [26]. A more detailed discussion on this result and the role of different heat transfer mechanisms on propagation in these materials is presented in a later section.

If the conjecture above is true, it should be possible to overcome the difficulties in propagation with the addition of material that could produce a condensable metal vapor. For our purposes, we chose CuO which was added in small amounts such that a certain percentage of the available Al would stoichiometrically react with I_2O_5 and the remainder would stoichiometrically react with CuO. Upon addition of 5% CuO (Al/95% I_2O_5/5% CuO), the sample propagated to completion in ~50% of all experiments with a propagation velocity of ~6 cm/s. Addition of more CuO (up to 25%) results in consistent propagation, albeit with a slightly lower velocity of ~3 cm/s. The propagation velocity of Al/75%

I_2O_5/25% CuO is more reflective of the high-loading Al/CuO films that were tested by Wang et al. [11,25]. A summary of the results is presented in Figure 5-1. Temperature-jump, time-of-flight mass spectrometry (T-Jump/TOFMS) was performed on oxidizer mixtures and revealed no apparent interactions between CuO and I_2O_5 that would promote decomposition or gas release (see Table S1). Furthermore, adiabatic flame temperature calculations (with CHEETAH) shown in Figure 5-7 demonstrates that the adiabatic flame temperature at constant pressure depresses slightly with the addition of CuO, implying that small additions of CuO do not significantly impact the overall thermophysics [32]. It is believed that, should the Al/I_2O_5 sample been capable of sustaining combustion, it would likely have propagated at the fastest rate since Al/I_2O_5 powders are known to burn faster than Al/CuO [33,34]. The apparent decrease in propagation velocity is therefore not a result of special interactions of the mixture, but rather reflects a sliding scale in performance from the pure Al/I_2O_5 to the Al/CuO case.

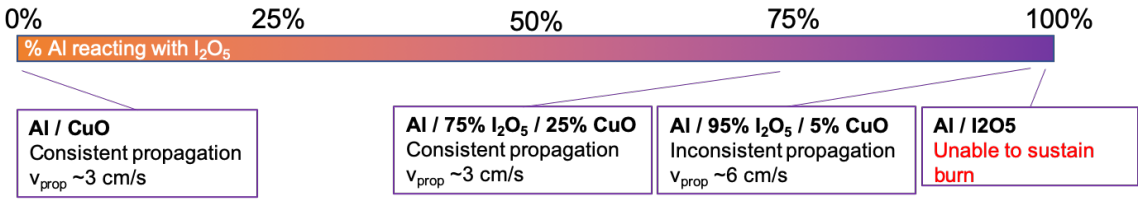

Figure 5-1. *Summary of combustion performance data from macroscale combustion experiments for different mixtures of Al/I_2O_5/CuO.*

Whereas it would regularly be expected that the large volume of gas generated by I_2O_5 during reaction would dramatically reduce reactive sintering leading to superior

performance, an energy deficiency emerges which leads to poor or non-propagation. The enhanced burn with small additions of CuO and the ability to made propagation consistent suggests that condensing metal vapor may play a significant role in combustion of these samples and will be explored later in this paper.

5.4.3 High-Speed In-Operando Microscopy

To further investigate energy transfer mechanisms that drive propagation in reactive materials, it was important to see how the material was reacting on the particle scale. Egan et al. suggested that advection of hot material from the reaction front to regions far away must provide significant energy contributions to sustain propagation in energetic materials to make up for an energy deficit that was present in their calculations [26]. When reaction propagation was visualized in our recent article, we did not see significant advection events for a high-loading Al/CuO ink, however there was substantially less gas generated from that composite in comparison to Al/I_2O_5 composites.

High-speed microscopy images of all of the Al/I_2O_5/CuO energetic composites tested showed clear particle advection events that were in stark contrast to the images that were presented in our previous study [25]. Each of the images collected in all of the mixtures had large concentrations of hot particle streaks that would either extinguish (if the final destination did not have a high concertation of advected particles) or would create a secondary ignition event at a location away from the front (depicted in Figure 5-2). The reaction fronts observed in these mixtures are also very different morphologically from those presented in our previous work. The reaction front in these mixtures is not clearly-

defined, likely due to the large gas generation that could distort the morphology at the film near the front [25].

Reaction temperatures for the propagation event were also processed using color camera pyrometry [24] to estimate the bulk reaction temperature and advected particle temperature. Figure 5-2a-b show a typical reaction propagation event for the Al/75% I_2O_5/25% CuO mixture and its corresponding temperature map, which shows a wide temperature distribution ranging from ~1500 K in cooling regions, and >2500 K in the reaction front and advected particles. The temperatures for the reaction front are lower than the adiabatic flame temperatures for the mixture which is likely due to the addition of polymer binders (which nominally have flame temperatures in the ~2000K region) incomplete reactions, and radiative loss. Measured temperature of the samples did not largely change with additions of CuO to the mixture, which is expected since the calculated adiabatic flame temperature changes only slightly with small additions of CuO (Figure 5-7, Figure 5-8 and Figure 5-9). An analysis on the energy transferred by advecting particles will be presented in later sections based on the pyrometry images presented below.

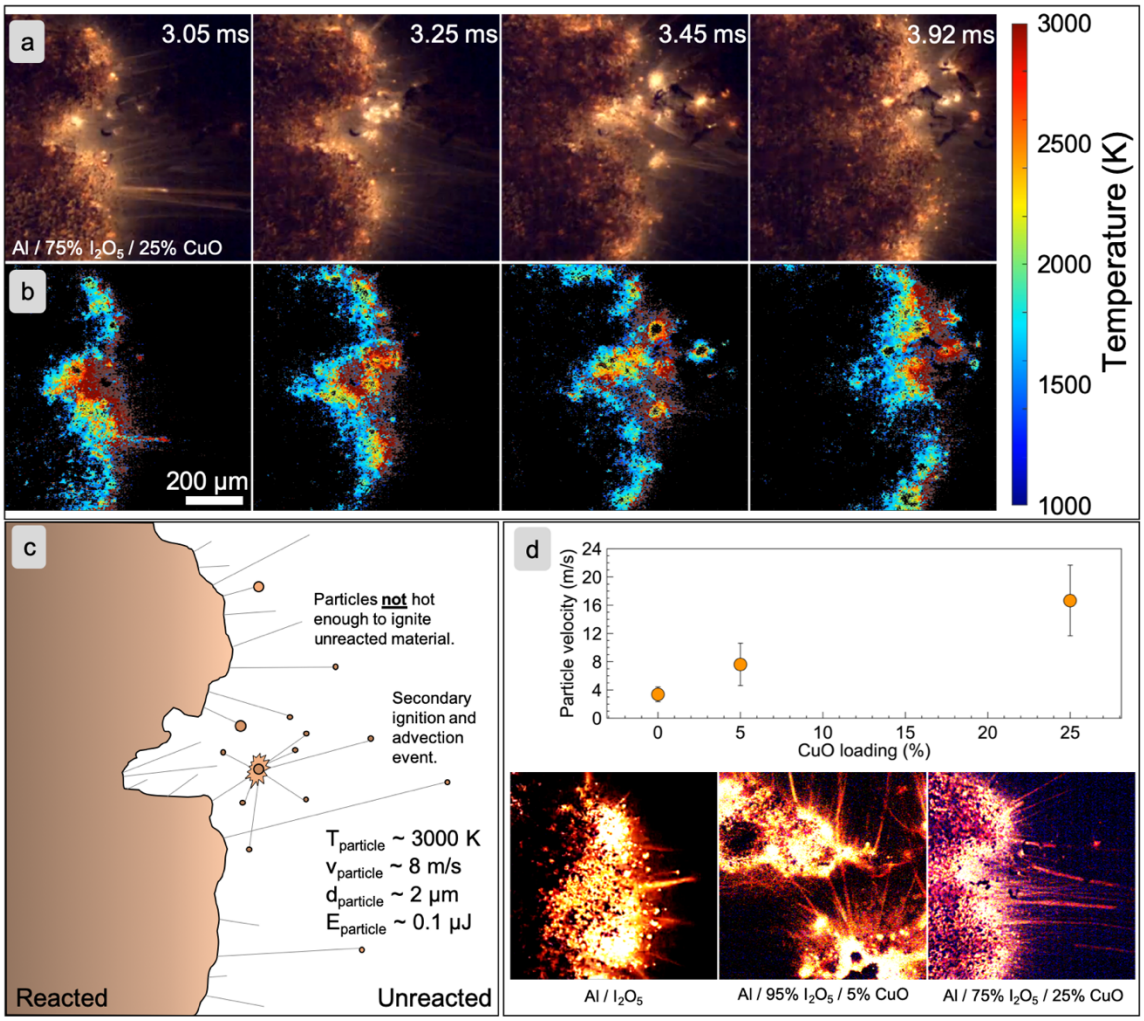

Figure 5-2. *(a) High-speed microscopy images for the Al/75% I_2O_5/25% CuO sample and (b) corresponding temperature maps as calculated by color ratio pyrometry. (c) Drawing depicting different advection events that are observed in the reaction front for the high-speed microscopy videos. (d) Average particle velocity for particles that are ejected from the reaction front and example image for each mixture. Pictures in (d) have been brightened to clearly show streaks, but each picture has the same exposure time.*

Velocities of the advected particles were estimated using the pixel/distance ratio for the assembly, estimated length of the particle path streak, and the exposure time of each frame. Despite the expectation that gas generation would increase the average advected particle velocity, the opposite phenomenon was found. With increasing CuO content, (see Figure 5-2d) the average particle velocity increases from ~3m/s to ~18m/s, both of which are ~100x faster than the bulk propagation speed. Assuming solid-to-gas conversion at constant pressure, the density difference should result in a factor of 1000x in gas velocity relative to the propagating front, in the absence of area expansion. Thus, the changes in particle velocity may result from a complex amalgam of gas production and expansion leading to particle advection. The main point, however, is that particle advection is clearly observed, consistent with the analysis of Egan et al., and will be discussed further in this paper.

5.4.4 Post-Reaction Forensics

A major detractor from using a metal oxidizer such as CuO in nanoenergetic composites with Al is the tendency for materials to reactively sinter to form μm-sized particles that can effectively slow reaction rates and lead to incomplete combustion [23,25]. Reactive sintering has been observed in other high-speed microscopy studies that we have performed, however it has been proposed in other works that the addition of a gas generator can reduce the degree of reactive sintering [24,25]. In principle, I_2O_5 would represent the ideal oxidizer since there is less metal that would be able to reactively sinter with the nAl

and the constant gas generation would likely enhance particle dispersion, leading to smaller product particles.

To investigate the degree of reactive sintering in the CuO-doped Al/I_2O_5 energetic composites, reaction products were imaged under a scanning electron microscope. Figure 5-3 shows the different particle morphologies for the reaction products as a function of CuO content. Interestingly, the rough final particle size did not appreciably vary from mixture to mixture, however, the final particle sizes were an order of magnitude smaller than those observed in a pure Al/CuO high-loading composite burn stick (~20μm) [25]. This result suggests that the gas generated from the decomposition of I_2O_5 significantly impacts the degree of reactive sintering, as expected, and that small additions of CuO do not significantly alter the final particle size. Particle morphology did seemingly change from mixture to mixture though, whereby the pure Al/I_2O_5 had an overwhelmingly spherical particle shape and the morphology shifted towards the previously-reported "snowman" shape that would arise from nanoparticles sintering [23,35]. The apparent surface roughness of the CuO-doped samples is also comparable to the post-combustion product images reported by Jacob et al. where the small surface features are Cu vapor condensate [36]. The presence of these small Cu surface features suggests that the combined nucleation and cooling time of small particles is on the time scale of the propagation [36]. It could be reasonably expected that the degree of reactive sintering would steadily increase as a function of CuO content since the amount of gas generated would decrease. Despite this proposed behavior, the Al/I_2O_5/CuO mixtures explored in this

study do not appear to significantly impact the overall degree of reactive sintering since the I_2O_5 content is still relatively high.

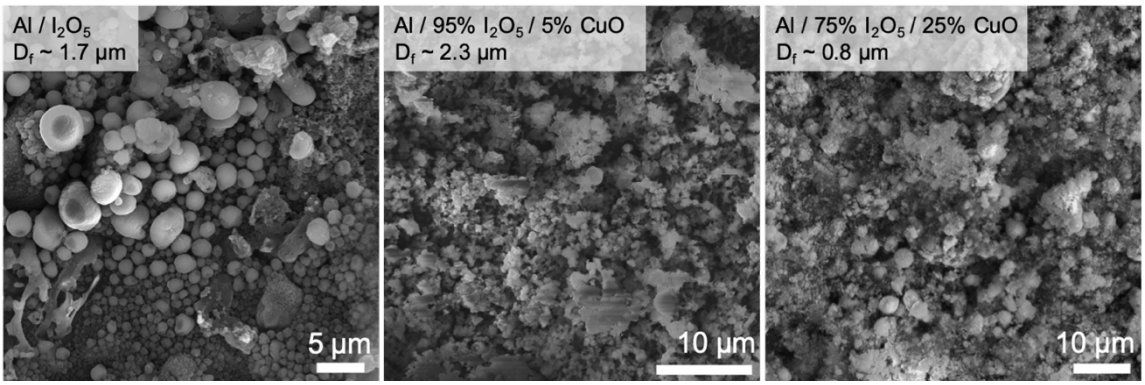

Figure 5-3. *Post-reaction SEM images for different CuO-doped Al/I_2O_5 composites and final particle diameter (D_f).*

5.5 Discussion

The results show that small additions of CuO can dramatically increase the reliability of a high-loading Al/I_2O_5 composite film. This observation points to the interplay of different heat transfer mechanisms on propagation that had previously only been estimated using back-of-the-envelope calculations. The discussion below explores the impact that advection and metal condensation have for sustained combustion in heterogeneous composites and proposes principles that can be extended to comparable systems.

Egan et al. estimated the extent to which the different heat transfer mechanisms contribute to the propagation of a tightly-packed Al/CuO composite, and has been adapted for the Al/I_2O_5/CuO composite system using the data presented in Table 5-3. The amount

of energy required per unit length (E/mm) to sustain propagation was estimated with data from the NIST Webbook by calculating the amount of energy required to raise the temperature of Al (including the Al_2O_3 shell) from room temperature to the ignition temperature of the Al/I_2O_5 mixture (~860 K), the amount of energy required to raise the polymer composites to their decomposition temperature (~683 K) [37], and the amount of energy required to decompose I_2O_5 (~440 J/g measured using TGA/DSC, see Figure 5-10). We assume that 10% of the mass of I_2O_5 was actually water [31]. Since the Al/CuO ignition temperature (~1050 K) is higher than that for Al/I_2O_5, it was assumed local regions would ignite first, leading to ignition of neighboring Al/CuO and therefore the ignition temperature of Al/I_2O_5 was used for all cases [26].

Using the parameters in Table 5-3, we find that a 2 mm-diameter packed tube would require ~1.9 J/mm to sustain propagation for each of the samples – approximately 90% of the amount of energy required to ignite a printed Al/CuO burn stick with the same characteristics [26]. One expects that higher reaction temperature and reduction in reactive sintering would favor sustained combustion in the Al/I_2O_5 system, but we observe the opposite effects. To investigate the root causes of this observation, we employ a heat transfer analysis for the various contributing factors that drive propagation, analogous to Egan et al. A summary of the data discussed below is shown in Figure 5-4.

5.5.1 Conduction Heat Transfer Estimates

Heat transfer from conduction was estimated using the same methods discussed in Egan et al. with slight modifications to the heat flux based on thermal measurements

performed and estimated values of thermal conductivity. Thermal maps presented in Figure 5-2a show a temperature drop of ~1500 K over a 200 μm distance, therefore the thermal gradient was estimated to be 7.5 x 10^6 K/m for all of the samples. The thermal conductivity for the composite was estimated to be ~1.2 W/mK based on a study by Zhou et al. where the thermal conductivity of Al/PVDF composites was measured as a function of volume fraction [38]. It is important to note that the thermal conductivity of the composite material is much lower than that of pure Al because of thermal boundary resistance at the interface between Al particles and the polymer matrix [38]. Additionally, the area over which the heat could be transferred in the condensed medium was corrected using a 67% porosity estimate. Thus, from the measured thermal gradient and estimated material properties, the maximum heat flux from conduction should be < ~9 W (Equation 5-11). This energy must be conducted in the amount of time that it takes for the reaction front to propagate a given distance, which in our case is less than 10 cm/s. Using this criterion, heat transfer via conduction only contributes ~0.09 J/mm – i.e. less than 5% of what would be theoretically required. We expect this to be an upper estimate, given that sample porosity will only lower the conductive heat flux. Therefore, we conclude that thermal conductivity is at best a minor heat flux source.

5.5.2 Radiation Heat Transfer Estimates

Radiative heat transfer from hot particles back to the surface was estimated by assuming that the reaction would have peak temperatures at the isobaric adiabatic flame temperature and that particles generated from the reaction had an ε=0.8 [39]. Given the

small area of condensed material being heated, this yielded a power of ~9-10 W (Equation 5-4), however, the propagation rate of the material once again limited the amount of time that the radiation would be able to occur. The energy contribution from radiation was therefore only ~0.10 J/mm – approximately 5% of the energy required.

5.5.3 Convective Heat Transfer Estimates

Convective heat transfer in the system was assumed to have perfect efficiency driven by the transfer of energy from hot gases to the unreacted material. The amount of gas generated per unit length of material was determined by calculating how much I_2 and O_2 gas could be produced from the I_2O_5 present in that length, and assuming that only these gases contributed to convective heat transfer.

Interestingly, the large quantity of gas generated during reaction is able to theoretically contribute ~3.2 J/mm of reactant – more than 170% of what is required for the mixture to sustain propagation (Equation 5-5). This result suggests that, given a confined volume where all of the energy generated by the gas could be transferred back into the system (such as a pressure cell or burn tube), the Al/I_2O_5 system would consistently be able to combust, however it is not a valid assumption for the system we are considering. For the constant pressure, open-environment burn stick experiments, the hot gas generated will also be driven away from the direction of propagation, as observed experimentally [11].

As an estimate for the amount of mass, and therefore energy, that would be transferred toward the propagating front, we assume that the mass transfer roughly scales

with porosity of the sample in accordance with Darcy's Law. If the pressure drop across the entire sample was equivalent to the pressure drop at lengths far away from the front, then the ratio of forward flow would scale as shown in Equation 5-1 where Φ is porosity, Q_f is forward flow, and Q_{tot} is total flow. We estimated our samples to be 67% porous, therefore our fraction of forward flow is ~40% of the total flow [29]. We then used this ratio to estimate the percentage of the theoretical heat transfer would be contributed toward propagation. This leads to an energy contribution from convection of ~1.2-1.3 J/mm – approximately 60-70% of the energy required.

$$\frac{Q_f}{Q_{tot}} = \frac{\Phi}{1+\Phi} \tag{5-1}$$

5.5.4 Metal Vapor Condensation Estimates

A major contributor to the heat transfer for propagation in Egan et al. was the condensation of metal vapors produced from the reaction. Equilibrium calculations performed in CHEETAH estimate the amount of condensable metal vapor in each mixture, other than Al, since oxidation is primarily expected to occur in the molten state. However, the amount of metal vapor that was allowed to condense was scaled using the same factor as was used in the convective heat transfer estimate since the vapor would flow with the other generated gases.

A major distinction between the analysis presented here and those in Egan et al. is the condition under which equilibrium calculations are performed. Since the experiment being modeled here is an open environment burn stick, equilibrium values for Cu vapor

concentration correspond to constant pressure conditions. Egan et al. employed a constant volume condition since burn tube experiments are effectively a constant volume system [26]. The change to a constant pressure system actually favors the formation of Cu in the vapor due to the volume expansion despite the lower adiabatic temperature [32]. For thoroughness, we have recalculated the Al/CuO case using values from a constant pressure equilibrium concentration of Cu and have presented the results in Figure 5-11 [40].

In the case of pure Al/I_2O_5, the lack of energy transfer from metal condensation dramatically impacts the amount of energy being transferred back to the unreacted material. Equilibrium calculations for the Al/I_2O_5/CuO find that ~0.5 mol and ~2.7 mol Cu vapor were produced per kg of reactant in the 5% and 25% CuO cases, respectively. Using heat capacity, heat of vaporization, heat of formation for Cu (NIST webbook), the Darcy Law correction to mass transfer (described above) and estimating that the vapor is cooling down from the isobaric adiabatic flame temperatures to the ignition temperature, ~0.38 J/mm (20% of required) and ~1.95 J/mm (99% of required) could be transferred to unreacted material for the 5% and 25% CuO cases, respectively (Equation 5-6).

It is important to consider the role that metal vapor condensation plays in propagation since the small particle condensates are clearly evident in the final product morphology of samples that had CuO. We can also justify that this heat would be transferred in a relevant time scale since Jacob et al. showed that the combined nucleation and cooling time of metal vapor is on the order of microseconds [36]. This suggests that even small additions of oxidizer with a condensable metal vapor dramatically reduces the reliance on advection for sustainable combustion and could even be eliminated. These

calculations are consistent with the observation that CuO additives are necessary in order for Al/ I_2O_5 high loading systems to propagate.

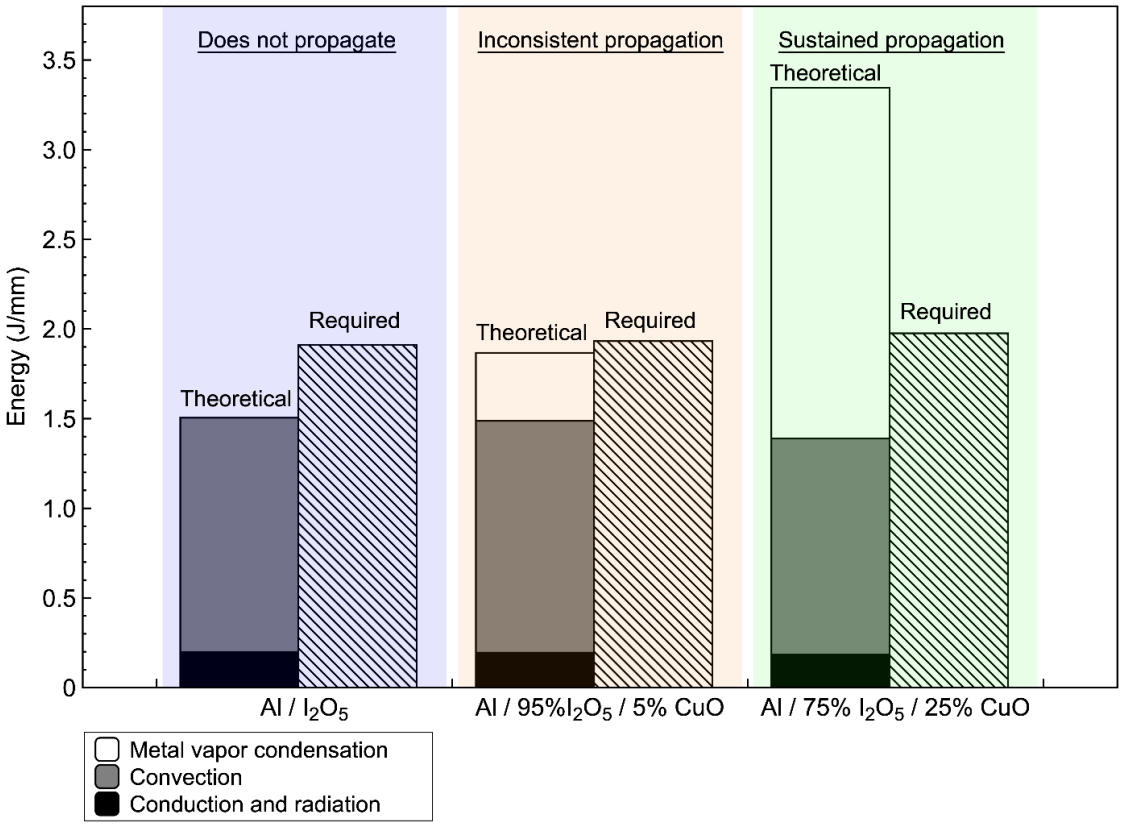

Figure 5-4. *Estimated values for the theoretical energy transfer and the amount of energy required to sustain combustion for different mixtures of Al/I_2O_5/CuO.*

5.5.5 Advective Heat Transfer

Advective heat transfer of hot particles to unreacted areas is very evident in the high-speed microscopy shown in Figure 5-2. Egan et. al simply estimated the amount of advective heat transfer based on the heat that could be recovered from molten Al and Cu

particles, however, we are able to use the high-speed pyrometry/microscopy apparatus to estimate the amount of energy that is transferred.

The energy content of each particle (E_p) is estimated by Equation 5-2 where the thermophysical properties (density: ρ_p, heat capacity: C_p) of the particle are assumed to be that for Al_2O_3 and the particle volume (V_p) can be calculated from the final particle size found in post-forensic SEM (~1-5μm). Assuming that the particle cools from the measured particle temperature (~3000 K) to the ignition temperature, each particle carries ~0.1 μJ (assuming a 2.5 μm-diameter particle). We can then estimate the number of particles that need to be generated per unit length of material by dividing the energy gap by E_p. The number of particles required to make up the energy deficit, assuming that convection makes no contribution to the energy transported and all of the condensed metal vapor is transferred back to the film, is ~4.4 x 10^6 particles/mm and ~7.2 x 10^5 particles/mm for Al/I_2O_5 and Al/95% I_2O_5/5% CuO composites, respectively. Thus a 5% addition of Cu results in an 83% reduction in required particle advection and highlights the importance of metal vapor condensation on reactive material propagation.

$$E_p = \rho_p V_p C_p (\mathrm{T_{ad}} - \mathrm{T_{ign}}) \tag{5-2}$$

The simple analysis illustrates the fine balance between the different modes of heat transfer for propagation in solid combustible materials. In scenarios where reliable propagation is critical, such as a stable burn of a solid propellant or delivery of a biocide,

small additions of an oxidizer with a condensable metal vapor could be the difference between guaranteed performance and critical failure.

5.6 Conclusions

Reactive sintering can negatively impact reactions in energetic composites prepared with nanoparticles since the loss of nanostructure can decrease burn rates and prematurely arrest reactions. Iodine pentoxide is an ideal oxidizer to reduce the amount of reactive sintering since the overwhelming gas generation will effectively atomize any sintering particles and it has immediate applications as a biocidal additive. When investigating high-loading Al/I_2O_5 films, the burn sticks were unable to propagate. Small additions of CuO (5-25%) to the Al/I_2O_5 mixture increased reliability in propagation with CuO content. High-speed pyrometry and microscopy were used to estimate advective heat transfer in the system and post-products showed only minor variation in the degree of reactive sintering with CuO addition. A simple energy balance performed to estimate the composite's reliance on advective heat transfer for propagation found that the elimination of condensing metal vapor (Cu from CuO) dramatically increased this dependency. It is proposed that small additions of CuO, resulting in a condensable product vapor, can effectively eliminate the reliance on heat transfer via advection enabling a more consistent propagation. These results highlight the fine balance between different heat transfer mechanisms that drive propagation in reactive materials.

5.7 Supplemental Information

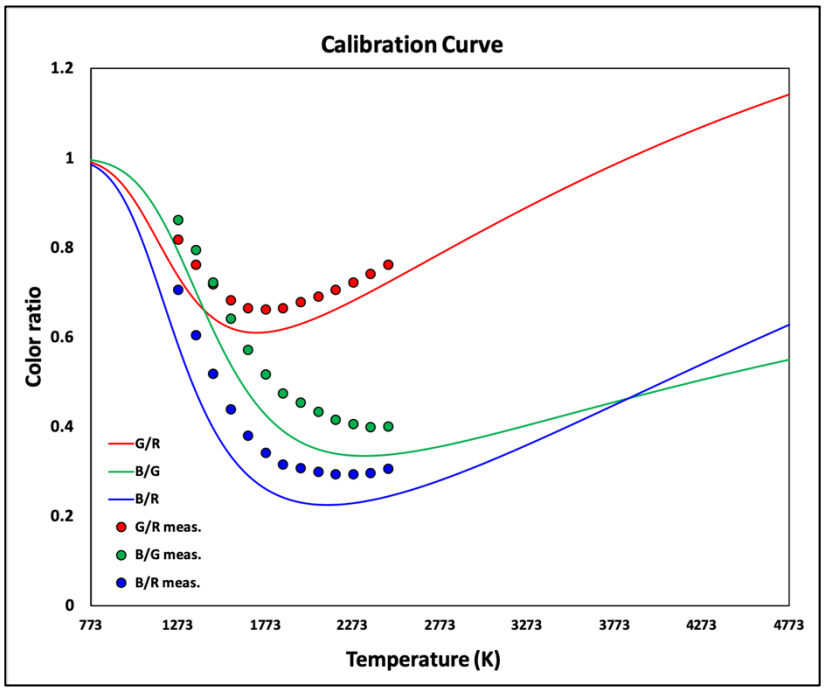

Figure 5-5. *Theoretical color channel ratios vs. temperature for the Phantom VEO710L and measured color ratios for the camera and lens assembly.*

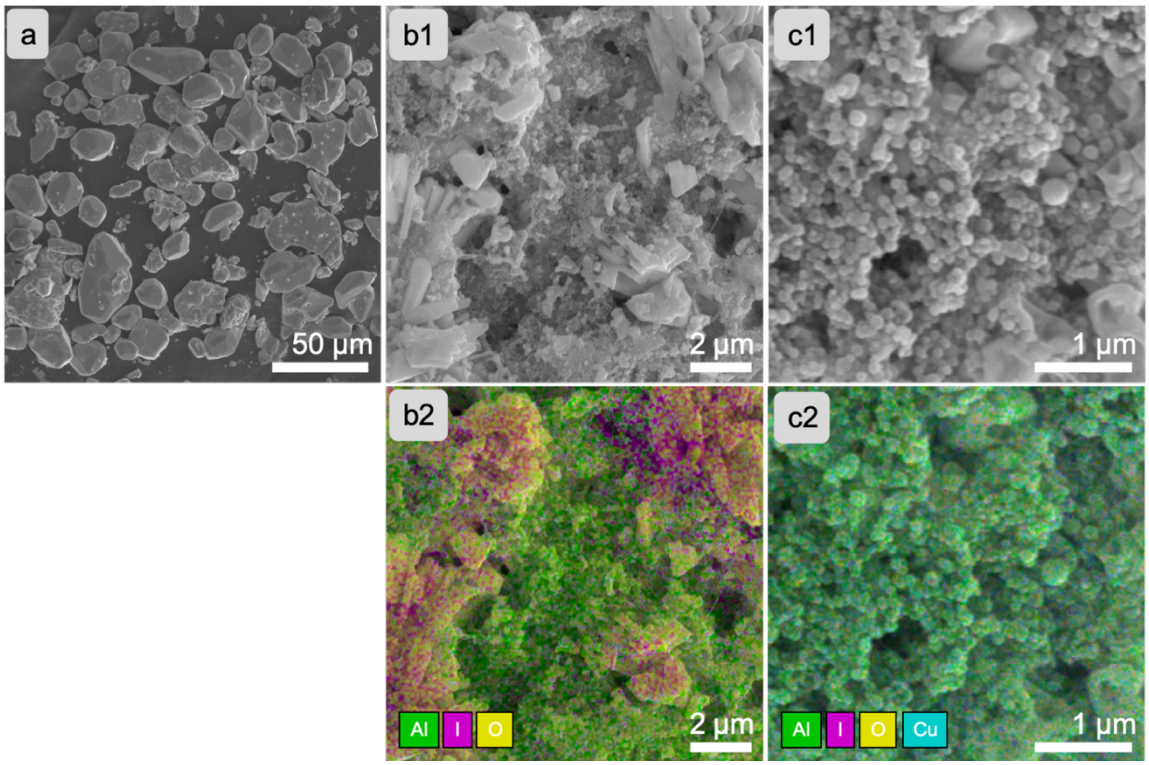

Figure 5-6. *(a) Commercially purchased I_2O_5 crystals. (b1) SEM image of the Al/I_2O_5 high loading burn stick and (b2) corresponding element map for the sample. (c1) SEM Image of the Al/75% I_2O_5/ 25% CuO high loading burn stick and (c2) corresponding element map for the sample.*

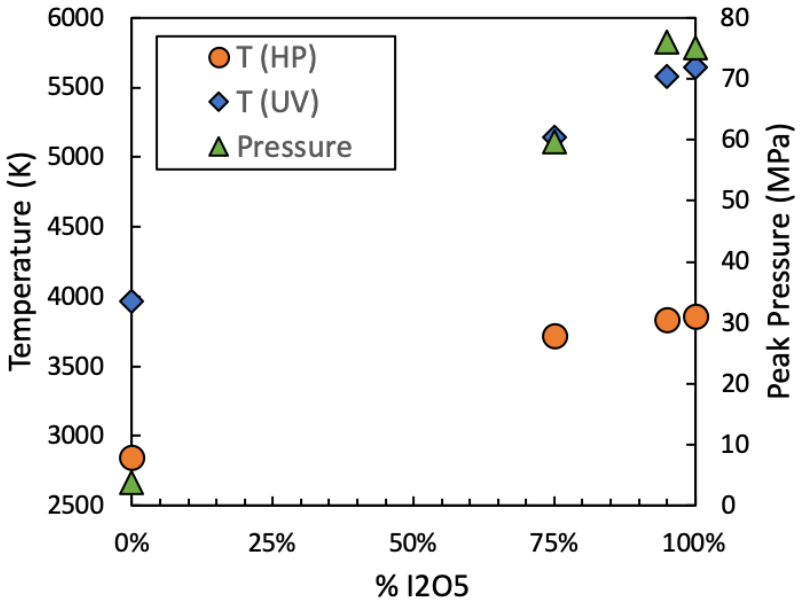

Figure 5-7. *Constant pressure (T HP) and constant volume (T UV) adiabatic flame temperature and equilibrium pressure for constant volume combustion. Constant volume calculations assume a 6% theoretical maximum density.*

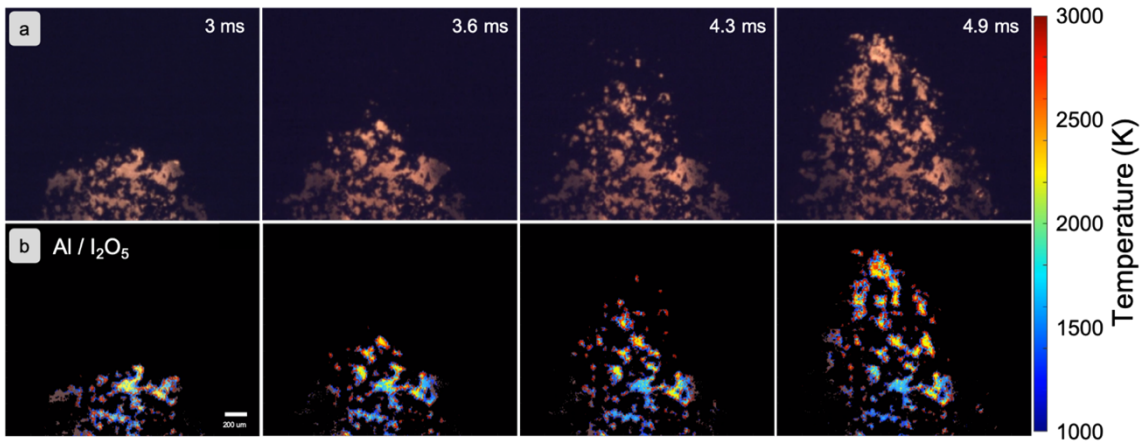

Figure 5-8. *(a) High-speed microscopy images for the Al/I_2O_5 sample and (b) corresponding temperature maps as calculated by color ratio pyrometry.*

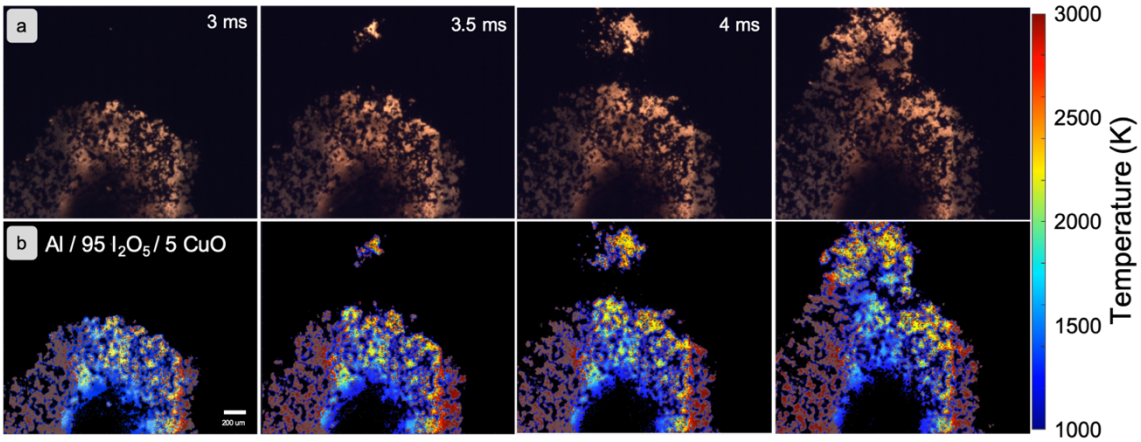

Figure 5-9. *(a) High-speed microscopy images for the Al/95% I_2O5/CuO sample and (b) corresponding temperature maps as calculated by color ratio pyrometry.*

Table 5-2. *Oxygen release temperatures for different oxidizers as measured using temperature-jump time-of-flight mass spectrometry.*

Material	**O_2 release T (°C)**
I_2O_5	421
I_2O_5/CuO	476
CuO	693

Table 5-3. *Parameters for estimating heat transfer requirements in Al/I_2O_5 system for propagation.*

Material System	wt.% Polymer	Tube Diam.	% TMD	Ign. T	Mass/mm	E/mm
Al / I_2O_5	4% PVDF, 6% HPMC	2 mm	33%	863 K	0.43 mg/mm	1.91 J/mm
Al / 95% I_2O_5 / 5% CuO	4% PVDF, 6% HPMC	2 mm	33%	863 K	0.44 mg/mm	1.93 J/mm
Al / 75% I_2O_5 / 25% CuO	4% PVDF, 6% HPMC	2 mm	33%	863 K	0.46 mg/mm	1.98 J/mm

Table 5-4. *Measured and theoretical densities of the Al/I_2O_5 composites with calculated porosity values.*

Material System	Measured density (g/cm^3)	Theoretical density (g/cm^3)	Porosity (%)
Al / I_2O_5	1.56	4.12	62
Al / 95% I_2O_5 / 5% CuO	1.63	4.17	61
Al / 75% I_2O_5 / 25% CuO	1.79	4.39	59

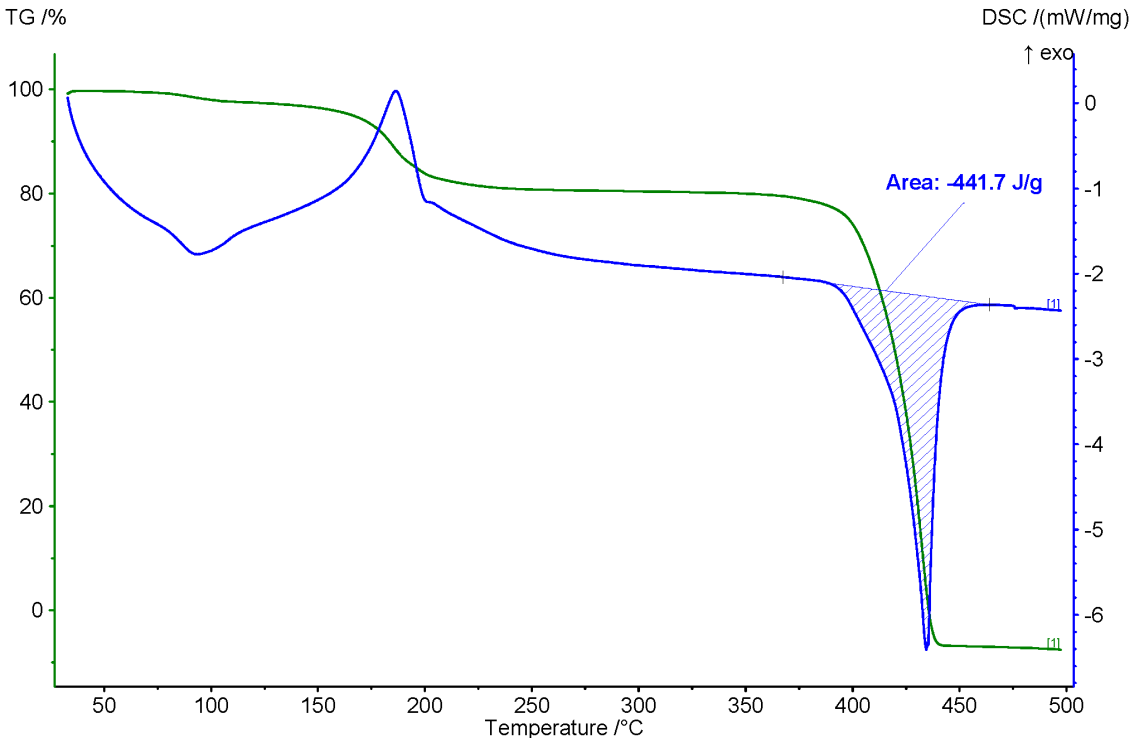

Figure 5-10. *Thermogravimetric analysis/differential scanning calorimetry results for* I_2O_5.

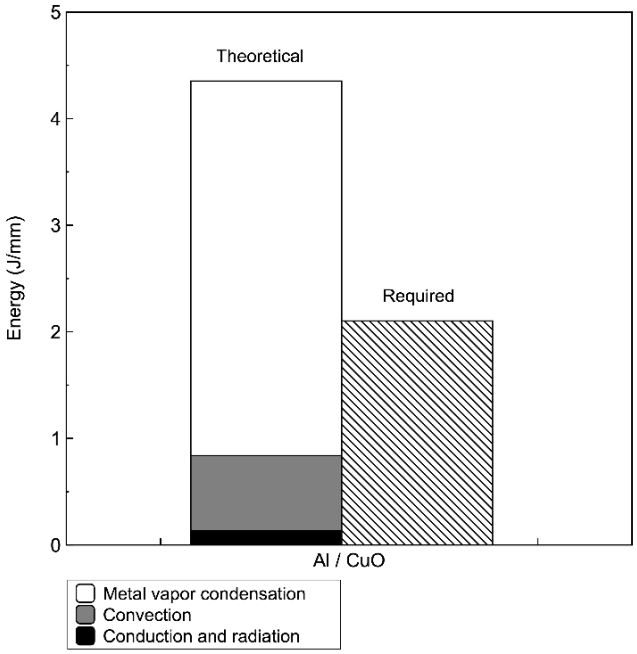

Figure 5-11. *Estimated values for the theoretical energy transfer and the amount of energy required to sustain combustion for Al/CuO using constant pressure equilibrium calculations. Propagation velocity assumed to be 802 m/s [40].*

$$E_{cond} = \frac{kA_{tube}(1-\Phi)}{v_{prop}}\left(\frac{dT}{dx}\right) \quad (5\text{-}3$$

$$E_{rad} = \frac{\sigma\varepsilon(1-\Phi)A_{tube}(T_{AFT}-T_0)}{v_{prop}} \quad (5\text{-}4)$$

$$E_{conv} = \left(\frac{Q_f}{Q_{tot}}\right)\left(\frac{m_{I2}}{L}\int_{T_{ign}}^{T_{AFT}} C_{p,I2}(T)\,dT + \frac{m_{O2}}{L}\int_{T_{ign}}^{T_{AFT}} C_{p,O2}(T)\,dT\right) \quad (5\text{-}5)$$

$$E_{vap} = \left(\frac{Q_f}{Q_{tot}}\right)\frac{m_{sample}}{L}m^*_{Cu}\left(\begin{array}{c}\int_{T_b}^{T_{AFT}} C_{p,Cu}(T)dT + \Delta H_{vap,Cu} + \int_{T_m}^{T_b} C_{p,Cu}(T)dT + \Delta H_{f,Cu} + \\ \int_{T_{ign}}^{T_b} C_{p,Cu}(T)dT\end{array}\right) \quad (5\text{-}6)$$

Table 5-5. *Variables for equations 5.3-5.6.*

Symbol	Name
k	Thermal conductivity (W/mK)
σ	Stefan-Boltzmann constant (W/m^2K^4)
ε	Emissivity
Cp	Heat capacity (J/gK)
ΔH_{vap}	Heat of vaporization (J/g)
ΔH_f	Heat of formation (J/g)
T_{AFT}	Adiabatic flame temperature (K)
T_{ign}	Ignition temperature (K)
T_b	Boiling temperature (K)
T_0	Initial temperature
dT/dx	Thermal gradient (K/m)
m_{sample}	Sample mass (g)
m_{I2}	Mass of I_2 (g)
m_{O2}	Mass of O_2 (g)
m^*_{Cu}	Mass of Cu vapor per kg reactant at equilibrium as calculated using Cheetah (g)
Q_f/Q_{tot}	Ratio of forward mass transfer to total transfer (estimated using Equation 5-1).
Φ	Porosity of sample
v_{prop}	propagation velocity (m/s)
A_{tube}	Cross-sectional area of tube (m^2)
L	Sample length (m)

5.8 References

[1] V.E. Zarko, A.A. Gromov, Energetic Nanomaterials: Synthesis, Characterization, and Application, Elsevier, 2016. https://doi.org/10.1016/C2014-0-01661-9.

[2] E. Lafontaine, M. Comet, Nanothermites, John Wiley & Sons, 2016.

[3] D.D. Dlott, Thinking big (and small) about energetic materials, Mater. Sci. Technol. 22 (2006) 463–473. https://doi.org/10.1179/174328406X83987.

[4] M.R. Zachariah, NanoEnergetics: Hype, reality and future, Propellants, Explos. Pyrotech. 38 (2013) 7. https://doi.org/10.1002/prep.201380131.

[5] K.T. Sullivan, J.D. Kuntz, A.E. Gash, The role of fuel particle size on flame propagation velocity in thermites with a nanoscale oxidizer, Propellants, Explos. Pyrotech. 39 (2014) 407–415. https://doi.org/10.1002/prep.201400020.

[6] D. Sundaram, V. Yang, R.A. Yetter, Metal-based nanoenergetic materials: Synthesis, properties, and applications, Prog. Energy Combust. Sci. 61 (2017) 293–365. https://doi.org/10.1016/j.pecs.2017.02.002.

[7] M.C. Rehwoldt, Y. Yang, H. Wang, S. Holdren, M.R. Zachariah, Ignition of Nanoscale Titanium/Potassium Perchlorate Pyrotechnic Powder: Reaction Mechanism Study, J. Phys. Chem. C. 122 (2018) 10792–10800. https://doi.org/10.1021/acs.jpcc.8b03164.

[8] M. Comet, C. Martin, F. Schnell, D. Spitzer, Nanothermites: A short Review. Factsheet for Experimenters, Present and Future Challenges, Propellants, Explos. Pyrotech. (2018) 1–20. https://doi.org/10.1002/prep.201800095.

[9] K.T. Sullivan, C. Zhu, E.B. Duoss, A.E. Gash, D.B. Kolesky, J.D. Kuntz, J.A. Lewis, C.M. Spadaccini, Controlling Material Reactivity Using Architecture, Adv. Mater. 28 (2016) 1934–1939. https://doi.org/10.1002/adma.201504286.

[10] H. Wang, D.J. Kline, M. Rehwoldt, T. Wu, W. Zhao, X. Wang, M.R. Zachariah, Architecture Can Significantly Alter the Energy Release Rate from Nanocomposite Energetics, ACS Appl. Polym. Mater. 1 (2019) 982–989. https://doi.org/10.1021/acsapm.9b00016.

[11] H. Wang, J. Shen, D.J. Kline, N. Eckman, N.R. Agrawal, T. Wu, P. Wang, M.R. Zachariah, Direct Writing of a 90 wt% Particle Loading Nanothermite, Adv. Mater. 31 (2019) 1–7. https://doi.org/10.1002/adma.201806575.

[12] A.M. Golobic, M.D. Durban, S.E. Fisher, M.D. Grapes, J.M. Ortega, C.M. Spadaccini, E.B. Duoss, A.E. Gash, K.T. Sullivan, Active Mixing of Reactive

Materials for 3D Printing, Adv. Eng. Mater. 1900147 (2019) 1–7. https://doi.org/10.1002/adem.201900147.

[13] L.J. Groven, M.J. Mezger, Printed Energetics: The Path toward Additive Manufacturing of Munitions, in: Energ. Mater., CRC Press, 2017: pp. 115–128.

[14] H. Wang, D.J. Kline, M. Rehwoldt, M.R. Zachariah, Ignition and Combustion Characterization of Ca(IO3)2-based Pyrotechnic Composites with B, Al, and Ti, Propellants, Explos. Pyrotech. 43 (2018) 977–985. https://doi.org/10.1002/prep.201800041.

[15] T. Wu, X. Wang, P.Y. Zavalij, J.B. DeLisio, H. Wang, M.R. Zachariah, Performance of iodine oxides/iodic acids as oxidizers in thermite systems, Combust. Flame. 191 (2018) 335–342. https://doi.org/10.1016/j.combustflame.2018.01.017.

[16] S. Wang, M. Schoenitz, S.A. Grinshpun, E.L. Dreizin, Biocidal effectiveness of combustion products of reactive materials : a phenomenological model, J. Aerosol Sci. (2017) 1–6. https://doi.org/10.1016/j.jaerosci.2017.11.007.

[17] D.K. Smith, D.K. Unruh, C.-C. Wu, M.L. Pantoya, Replacing the Al 2 O 3 Shell on Al Particles with an Oxidizing Salt, Aluminum Iodate Hexahydrate. Part I: Reactivity, J. Phys. Chem. C. (2017) acs.jpcc.7b05803. https://doi.org/10.1021/acs.jpcc.7b05803.

[18] J.L. Gottfried, D.K. Smith, C. Wu, M.L. Pantoya, Improving the Explosive Performance of Aluminum Nanoparticles with Aluminum Iodate Hexahydrate (AIH), Sci. Rep. (2018) 1–12. https://doi.org/10.1038/s41598-018-26390-9.

[19] H. Wang, S. Holdren, M.R. Zachariah, Preparation and combustion of laminated iodine containing aluminum/polyvinylidene fluoride composites, Combust. Flame. 197 (2018) 120–126. https://doi.org/10.1016/j.combustflame.2018.05.016.

[20] M.A. Hobosyan, K.S. Martirosyan, Iodine Pentoxide Nano-rods for High Density Energetic Materials, Propellants, Explos. Pyrotech. 42 (2017) 506–513. https://doi.org/10.1002/prep.201600220.

[21] W. Zhao, X. Wang, H. Wang, T. Wu, D.J. Kline, S. Holdren, M. Rehwoldt, H. Ren, M.R. Zachariah, Titanium enhanced ignition and combustion of nano-Al/I2O5 composites, Combust. Flame. (2019).

[22] P. Chakraborty, M.R. Zachariah, Do nanoenergetic particles remain nano-sized during combustion?, Combust. Flame. 161 (2014) 1408–1416. https://doi.org/10.1016/j.combustflame.2013.10.017.

[23] K.T. Sullivan, N.W. Piekiel, C. Wu, S. Chowdhury, S.T. Kelly, T.C. Hufnagel, K.

Fezzaa, M.R. Zachariah, Reactive sintering: An important component in the combustion of nanocomposite thermites, Combust. Flame. 159 (2012) 2–15. https://doi.org/10.1016/j.combustflame.2011.07.015.

[24] R.J. Jacob, D.J. Kline, M.R. Zachariah, High speed 2-dimensional temperature measurements of nanothermite composites: Probing thermal vs. Gas generation effects, J. Appl. Phys. 123 (2018). https://doi.org/10.1063/1.5021890.

[25] H. Wang, D.J. Kline, M.R. Zachariah, In-operando high-speed microscopy and thermometry of reaction propagation and sintering in a nanocomposite, Nat. Commun. 10 (2019). https://doi.org/10.1038/s41467-019-10843-4.

[26] G.C. Egan, M.R. Zachariah, Commentary on the heat transfer mechanisms controlling propagation in nanothermites, Combust. Flame. 162 (2015) 2959–2961. https://doi.org/10.1016/j.combustflame.2015.04.013.

[27] MathWorks, Image Processing Toolbox, (2019).

[28] G. Jian, S. Chowdhury, J. Feng, M.R. Zachariah, The ignition and combustion study of nano-al and iodine pentoxide thermite, in: 8th US Natl. Combust. Meet. 2013, 2013.

[29] G.D. Scott, D.M. Kilgour, The density of random close packing of spheres, J. Phys. D. Appl. Phys. 2 (1969) 863–866. https://doi.org/10.1088/0022-3727/2/6/311.

[30] C.D. Zangmeister, J.G. Radney, L.T. Dockery, J.T. Young, X. Ma, R. You, M.R. Zachariah, Packing density of rigid aggregates is independent of scale, Proc. Natl. Acad. Sci. U. S. A. 111 (2014) 9037–9041. https://doi.org/10.1073/pnas.1403768111.

[31] D.K. Smith, M.L. Pantoya, J.S. Parkey, M. Kesmez, The water-iodine oxide system: A revised mechanism for hydration and dehydration, RSC Adv. 7 (2017) 10183–10191. https://doi.org/10.1039/c6ra27854j.

[32] S. Bastea, L.E. Fried, K.R. Glaesemann, W.M. Howard, P.C. Sovers, P.A. Vitello, CHEETAH 5.0, User's Manual, Lawrence Livermore Natl. Lab. Livermore, CA. (2006).

[33] K.T. Sullivan, O. Cervantes, J.M. Densmore, J.D. Kuntz, A.E. Gash, J.D. Molitoris, Quantifying Dynamic Processes in Reactive Materials: An Extended Burn Tube Test, Propellants Explos. Pyrotech. 40 (2015) 394–401. https://doi.org/10.1002/prep.201400267.

[34] R. Russell, S. Bless, M. Pantoya, Impact-driven thermite reactions with iodine pentoxide and silver oxide, J. Energ. Mater. 29 (2011) 175–192.

[35] G.C. Egan, T. LaGrange, M.R. Zachariah, Time-Resolved Nanosecond Imaging of Nanoscale Condensed Phase Reaction, J. Phys. Chem. C. 119 (2015) 2792–2797. https://doi.org/10.1021/jp5084746.

[36] R.J. Jacob, G. Jian, P.M. Guerieri, M.R. Zachariah, Energy release pathways in nanothermites follow through the condensed state, Combust. Flame. 162 (2015) 258–264. https://doi.org/10.1016/j.combustflame.2014.07.002.

[37] M.C. Rehwoldt, H. Wang, D.J. Kline, T. Wu, N. Eckman, P. Wang, N.R. Agrawal, M.R. Zachariah, Ignition and combustion analysis of direct write fabricated aluminum/metal oxide/PVDF films, Combust. Flame. 211 (2020) 260–269. https://doi.org/10.1016/j.combustflame.2019.08.023.

[38] W. Zhou, J. Zuo, W. Ren, Thermal conductivity and dielectric properties of Al/PVDF composites, Compos. Part A Appl. Sci. Manuf. 43 (2012) 658–664. https://doi.org/10.1016/j.compositesa.2011.11.024.

[39] J. Kalman, T. Hedman, On the Origin and Use of the Emissivity Approximations for Alumina Particles, Propellants, Explos. Pyrotech. 41 (2016) 793–797. https://doi.org/10.1002/prep.201600109.

[40] V.E. Sanders, B.W. Asay, T.J. Foley, B.C. Tappan, A.N. Pacheco, S.F. Son, Reaction Propagation of Four Nanoscale Energetic Composites (Al/MoO3, Al/WO3, Al/CuO, and B12O3), J. Propuls. Power. 23 (2007) 707–714. https://doi.org/10.2514/1.26089.

6 Dynamic Modulation of Combustion in Al/Zr/C Composites via Localized Microwave Energy

6.1 Introduction

Solid propellants possess unique qualities such as high-energy density, safety and design simplicity which have made them very attractive in the space exploration industry. Currently, critical drawbacks such as an inability to control the thrust of the propellant and the lack of an on-demand stop/restart of propulsion has impeded the use of solid propellants in high-precision orbit insertion technologies where throttling is required. Various approaches have been taken to address the throttability challenge such as mechanical modifications to motor designs, structural changes to propellants, and laser augmentation of combustion, as described in detail in Chapter 1.4. The work described in this thesis, focuses on utilizing microwave energy to modulate combustion in-operando in solid propellants. In order to understand the effect of localized microwave heating on combustion of solid propellants, it was critical to distinguish the influence of secondary mechanisms induced and amplified by microwave stimulation such as ionization of species from the condensed phase microwave heating effects. Excitation and heating of ionized combustion gas products have been shown to greatly influence the behavior of solid propellants under microwave stimulation [1,2]. One way to differentiate condensed phase heating effects in combusting materials is to use materials that propagate primarily without gas generation.

A class of materials that can satisfy this experimental criterion are reactive materials that can undergo a self-propagating, high-temperature synthesis (SHS) reaction. When an activation barrier is overcome, these reactive composites release stored energy to stimulate chemical mixing and synthesis of stable compound phases via gasless combustion [3,4]. Various dielectric and ceramic materials were synthesized via SHS reactions: carbides (TiC, ZrC, Al_3C), borides (TiB, MoB, ZrB_2), nitrides (Mg_3N_2, TiN, SiN) and aluminides (NiAl, CoAl, ZrAl) [3,5]. The combustion wave structure of SHS reaction consists of three main zones: pre-heating, reaction, and product (cooling) zones [6–8]. The pre-heating region is classified as a zone before ignition temperature is reached and any exothermic chemistry occurs in the reactive materials. The reaction zone is accompanied with a high-conversion rate of the reactants to products and is bound between ignition and adiabatic flame temperatures of the combustion reaction. The region after the reaction zone is the product zone which is accompanied by the cooling of the formed products. Ballas et al studied the effect of thermal conductivity on combustion wave structure and propagation rate of SHS reaction. A developed mathematical model revealed that a high ratio (>5) of thermal conductivity of products to reactants leads to thinning of the reaction zone and a steep thermal gradient in the region. This, in turn, concentrates the heat in the unreacted section of the flame front, resulting in faster propagation rates. Similarly, multiple studies showed that an application of a direct current electric field (DC, 10^4 A) provides heat feedback to the propagating front, negating the heat loss effects and increasing the combustion reaction rate [9–11]. The results demonstrated a linear dependence of the propagation rate with the applied DC electric field intensity and

highlighted that Joule heating of the sample during combustion leads to the described effects.

Previous work by Arlington et al demonstrated that a mixture of Al-Zr-C composites can undergo gasless combustion to prepare electrically conductive products. Prepared by reactive ball milling and 3D printed at 98.6 wt.% solids loading, the mixtures undergo alloying reactions to form ZrC intermixed in Al, Zr and Zr_aAl_b with final electrical resistivities ranging from 300 – 1500 μΩ-cm [12]. Once the ignition temperature is achieved, the reaction begins with the melting of Al at ~660°C followed by the following exothermic reactions [13]:

$$Zr\ (solid) + Al\ (liquid) \rightarrow\ Zr_aAl_b(liquid) \tag{6-1}$$

$$Zr_aAl_b(liquid) + C\ (solid) \rightarrow\ Zr_aAl_bC_c(liquid) \tag{6-2}$$

$$Zr_aAl_b(liquid) + C\ (solid) \rightarrow\ ZrC(solid) + Al\ (liquid) \tag{6-3}$$

$$Al\ (liquid) + C(solid) \rightarrow AlC_c\ (liquid) \tag{6-4}$$

Here melted Al undergoes exothermic alloying with Zr to form liquid phase Zr_aAl_b that can further react with C to form $Zr_aAl_bC_c$. Once the saturation point of C concentration is achieved ZrC particles nucleate with Al post-products as shown in Equation 6-3. Additionally, in some cases reaction in Equation 6-4 proceeds and AlC_c can be found in the final synthesized products.

The work described in this thesis attempts to unravel the effect of condensed phase microwave heating on combustion profiles of direct-ink written 2Al/1.2Zr/1C composites. A custom-made monopole antenna set-up was used to stimulate the propagating reaction front via microwave energy at 2.45 GHz. A simultaneous color camera and infrared imaging tools were used to understand the influence of microwave heating on the propagation of the reaction. Post-processing of the color camera images enabled the deconvolution of the effect of microwave stimulus on the combustion front. This work builds a pathway for on-demand regulation of combustion via microwave energy, where it can further be expanded to observe how pulsing and hot spot changes can control the solid propellant performance.

6.2 Experiments/Methods

6.2.1 Ink Fabrication and Printing

For each print, 1.4 mL of dimethylformamide (DMF) was added to 50 mg of cellulose acetate and mixed at 2000 rpm for 2 minutes in a centrifugal mixer (Thinky mixer, USA). Powder of 2Al/1.2Zr/1C was then added at 3600 mg and mixed two times for 2 minutes each at 2000 rpm. The viscous ink was then loaded to a 10 mL syringe connected to a tapered end Luer-Lock 18 gauge nozzle. The high viscosity of the ink and paste like texture required the use of spatula during the transfer of the mixture to the syringe. After transfer to the syringe, the sample was immediately printed to avoid evaporation of the solvent. The printing speed of the nozzle was set to a multiplier 1 and flow rate of F750,

which resulted in an extraction rate of 250 mm/min and a volumetric extrusion rate of 56 mm^3/min.

6.2.2 Material Characterization

Scanning electron microscopy (SEM NNS450) was used to observe the printed microstructures of Al-Zr-C composites after printing. Coupled with electron dispersive analysis (EDS, NNS450), the resulting micrographs revealed the size and distribution of material constituents in the samples. The samples were sputter coated for 60 s with a thin layer of Pt/Pd (Cressington 108 Auto). Additionally, X-ray diffraction (XRD, PANalytical Empyrean Series 2, Cu-Kα source (λ=1.543 Å), step size: 0.013°) analysis was performed to assess the crystallinity of the samples before and after combustion.

6.2.3 High-Speed Thermography

High-speed color camera imaging (Vision Research Miro110) was used to record the combustion event in the samples with and without microwave stimulation. The acquisition rate was set to 500 frames per second (fps) due to the inherently slow propagation rate of the samples. The exposure time was set to 500 µs with the f#16. The set values were maintained for all combustion runs. The acquired videos were further processed via a custom-made MATLAB script to derive spatial and temporal temperature data as described in detail in Chapter 2.1.1 [14]. Infrared thermometry (Telops, FastM3K) was used to record the heating of the samples prior to ignition to account for temperature regions below the high temperature bounds (773 K – 4773 K) imposed by color ratio

pyrometry. The exposure time of the infrared camera was set to 5 µs with the emissivity set to 1. Since infrared data was mainly used to estimate temperature change over time, the emissivity adjustment did not affect the resultant heating rate values (°C/s).

6.3 Results

6.3.1 Material Constituents and Microwave Absorption

The printed composites are primarily comprised of aluminum (Al, 48 at.%) and zirconium (Zr, 29 at.%) metals, with a small fraction of carbon (C, 23 at.%) was also present. The X-ray diffraction analysis shown in Figure 6-1 displays the crystalline phases of the material constituents. Conventionally, conductive particles are regarded as reflective under microwave radiation due to screening of the incident waves within material's skin depth. Yet, previous studies have shown that the microwave absorption of electrical conductors is largely dependent on particle size [15–17]. For micron sized non-magnetic metal particles, absorption at 2.45 GHz is maximized when $particle\ size = 2.51 * skin\ depth$ [15,18]. The total absorption in that case is dominated by the magnetic field, where induced eddy currents in the conductive particles lead to induction heating.

Since the objective of this work is to modulate the reactive material's performance during combustion, it was critical to understand the effect of elevated temperatures on the absorption efficiency of individual components. Computational modeling results presented in Figure 6-1b were developed and performed by Prithwish Biswas. Metals have a decreasing trend of electrical conductivity with temperature increase as calculated from Equation 6-5. According to Drude model, as seen in Equation 6-6, the imaginary part of

the complex permittivity changes with the electrical conductivity of the metal and incident frequency; therefore, rising temperature causes a decrease in the imaginary part of the complex permittivity [19]. This results in a decrease in the total power absorbed in both Al and Zr particles, as shown in Figure 6-1, and lower inductive heating with lower electrical conductivities. The total power absorbed in metals was estimated based on Mie theory calculations used in Chapter 3.3.4, where Equation 3-1 was used to calculate the fraction of absorbed radiation. Contrastingly, carbon flakes are heated by the absorption of incident electric field due to their non-magnetic nature and low electrical conductivity. The dielectric properties of carbon $\varepsilon = 33 + 10i$ were used to estimate the volumetric power absorbed by the constituent (28 GW/m^3).

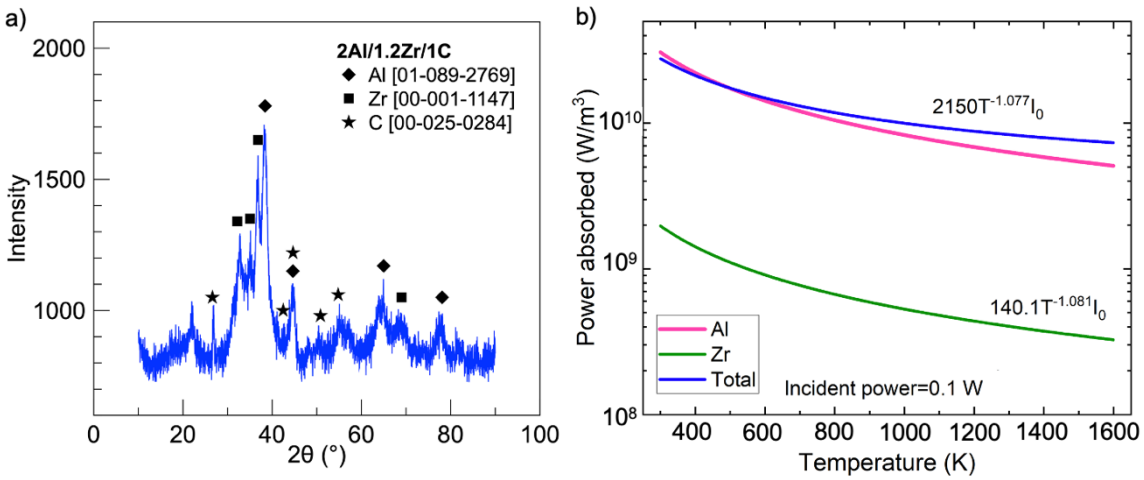

Figure 6-1. *a) X-ray diffraction analysis of 2Al/1.2Zr/C ball-milled powders; b) Mie theory calculation results of absorbed power in 4.4 μm Al and Zr particles and their total absorption.*

$$\frac{1}{\sigma(T)} = \frac{1}{\sigma(T=298)}[1 + A(T - 298)] \quad (6\text{-}5)$$

$$\varepsilon(T) = -\frac{i\sigma(T)}{\omega\varepsilon_0} \quad (6\text{-}6)$$

In the equations above ε is the imaginary part of the permittivity, σ is the electrical conductivity, A is the pre-exponential factor ($4x10^3\ 1/K$), ω is the phase of the incident frequency, ε_0 is the relative permittivity. For all Mie theory calculations that estimate the absorbed power, the real part of permittivity is set to 1.

6.3.2 Microwave Modulation Measurements

The particles were assembled into 2 x 3 mm rectangular structures as shown in Figure 6-2. The nominal size of the ball milled particles, prepared by Dr. Shane Q. Arlington from Weihs Group at John Hopkins University, are ~4.4 μm as shown in Figure 6-2b and summarized elsewhere [12]. The localized microwave set-up described in Chapter 2.3.2 was used to heat the samples under microwave radiation at 150 and 200 W incident power, where the printed sample was placed at a 3 mm vertical distance away from the antenna tip as shown in Figure 6-2b. The samples were ignited via Joule heating by applying an electrical current to the nichrome wire at the opposite end of the antenna. A ~20 mm distance was maintained between the ignition wire and electromagnetic radiation source. The microwave source was powered on manually, shortly followed by the simultaneous trigger of the ignition wire. The baseline propagation of direct-ink written Al-Zr-C composites was registered without microwave energy application.

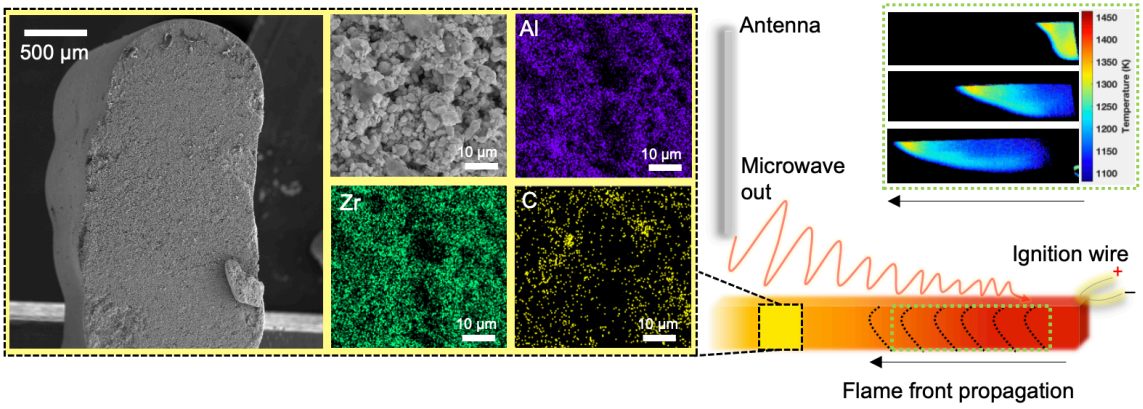

Figure 6-2. *a) Scanning electron micrograph of the printed sample b) zoomed in SEM image of the sample microsctructure and c-e) corresponding electron dispersive spectroscopy maps f) illustrative schematic of the sample propagating under microwave irradiation from monopole antenna source.*

6.3.3 Propagation Rate Measurements

The propagation rate of the composites without microwave application displayed a linear burn rate of 1.7 mm/s. Previous works have shown that the propagation rate varies between 1 – 4 mm/s in Al-Zr-C reactions, where it largely depends on the binder fraction, sample height and heat losses to the substrate [12]. We attribute the baseline propagation rate of 1.7 mm/s to the heat losses to the substrate that is composed of stacked glass slides (18 mm total thickness) placed on the metal surface of the Faraday cage. Previously reported higher values were registered during propagation in argon for samples placed on suspended thin glass substrates (0.2 mm total thickness), which reduced the overall heat losses from the samples and resulted in higher reported burn rate values [13]. Under microwave stimulation the propagation rate increased from a baseline value of 1.7 mm/s

to 2.2 mm/s at an applied power of 84 W/cm^2 and 3.4 mm/s at applied power of 284 W/cm^2. The heat balance equation of the flame front in solid phase combustion depends on reaction rate, heat losses from conduction, radiation and convection as seen on the right-hand side of the Equation 6-7 [6,7,20] below:

$$\rho c_p \frac{dT}{dt} = k\left(\frac{d^2T}{dx^2} + \frac{d^2T}{dy^2}\right) + \rho Q \frac{\partial \eta}{\partial t} - h(T - T_0) - \sigma\varepsilon(T^4 - T_0^4) \qquad (6\text{-}7)$$

where ρ is the reactant's density, c_p is the specific heat capacity, Q is the heat of reaction, $\frac{\partial \eta}{\partial t}$ is the reaction rate, h is the convection heat transfer coefficient, σ is the Stefan-Boltzmann constant, ε is the emissivity. For particles undergoing solid-state reaction, convective and radiative heat losses are typically neglected due to their smaller contribution as compared to conductive heat losses. The rate of reaction propagation (υ) is proportional to the rate of temperature change over time as seen in Equation 6-8 below. When an external microwave stimulus is applied to the sample, additional energy is deposited that results in the increase of the propagation rate as seen in Equation 6-9. As seen in the snapshots of Figure 6-3b-c, the total length of the flame front increases with microwave application as well. To further explore the influence of external microwave stimulus on the flame front profile, it is critical to get temperature data from the acquired propagation videos.

$$\rho c_p \frac{dT}{dt} = \rho c_p \upsilon \Delta T \qquad (6\text{-}8)$$

$$\rho c_p \frac{dT}{dt} = k\left(\frac{d^2T}{dx^2} + \frac{d^2T}{dy^2}\right) + \rho Q \frac{\partial \eta}{\partial t} + Q_{abs} \qquad (6\text{-}9)$$

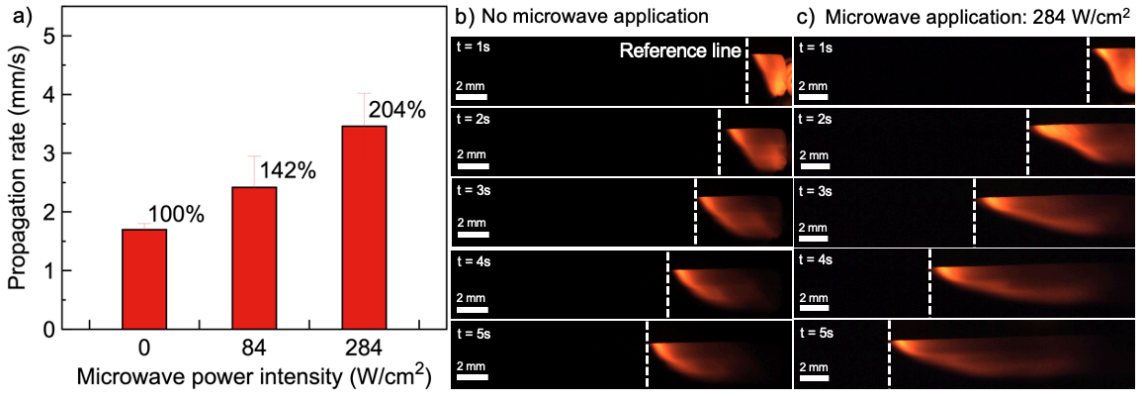

Figure 6-3. *a) Propagation rate as a function of applied microwave energy. Snapshots of the material combustion b) without microwave application and c) with 284 W/cm^2 applied power.*

6.3.4 Temperature Profiles

Color ratio pyrometry analysis showed that the thermal gradient across the sample changes with the application of electromagnetic energy. Axial temperature profiles were plotted as a function of applied microwave energy in Figure 6-4. The total length of the flame front is 7-8 mm without microwave application and increases to ~11 and ~16 mm at 84 and 284 W/cm^2 applied power intensities. As mentioned earlier, the combustion flame front typically consists of three major regions: pre-heating, reaction and cooling zones. In our case, the application of microwave energy extended the width of the reaction zone from 554 µm to 1050 µm at a 284 W/cm^2 applied power intensity. Interestingly, the maximum flame temperatures stayed within the same value range of 1650 – 1700 K, regardless of the

microwave application. This might be due to the low fidelity of the temperature measurements as compared to the temperature changes which are smaller or on par with the established error thresholds (200 K). In the maximum temperature zone, the energy deposition rate from the microwave must be lower compared to the energy input from the reaction. Unchanged maximum temperature values and increased reaction zone length led to the decrease in the detected thermal gradients in the reaction zone region. A substantial decrease in the thermal gradients of the reaction zone are indicative of lower conductive heat loss rates, which contributes to the heat reinforcement to the flame front leading to faster propagation rates. Similarly, the cooling zone of the reaction loses heat slower as opposed to the case without microwave stimulation. The total length of the flame front doubles when the applied power intensity increased from 0 to 284 W/cm^2. These results are counter-intuitive to the conventional understanding of the relation between reaction zone thickness and propagation rates, where high propagation rates are typically associated with thin reaction zones. However, additional microwave stimulus provided to the propagating wave front increases the temperatures of the pre-heating and cooling zones, which decreases the overall contribution of conductive heat losses shown in Equation 6-9. This results in increased propagation velocities with an electromagnetic stimulus provision, while an increased heat feedback from the microwave source results in decrease of the thermal gradients between reacted and unreacted species which results in an increase in the overall thickness of the reaction front.

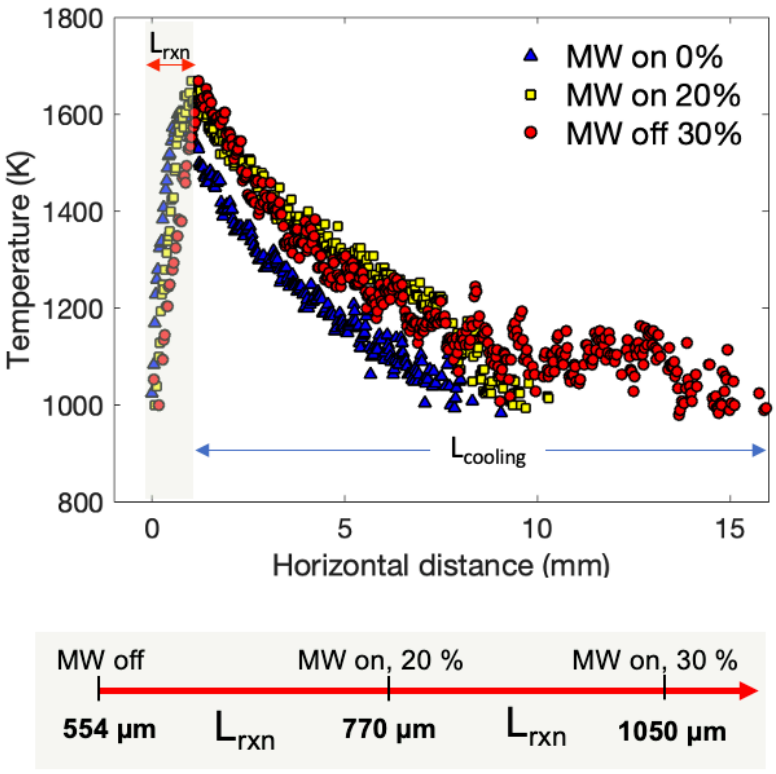

Figure 6-4. *Axial profile of the temperature as a function of applied microwave intensity.*

6.3.5 Reaction Post-Product Analysis

The effect of microwave absorption on chemical reaction pathways was studied based on the X-ray diffraction analysis of the combustion post-product species with and without microwave application. All X-ray diffraction patterns were acquired by Feiyu Xu at Zachariah Group. As seen in Figure 6-5, crystalline phases of Al_3Zr, Al, ZrC, ZrO and ZrO_2 were detected in both samples. The presence of Al_3Zr, Al and ZrC supports the claim that the reactions described in Equations 6-1 and 6-3 occur during the combustion of Al-Zr-C under ambient conditions. However, the detected presence of Al_3Zr also implies that the reaction does not go to completion via full consumption of Zr_xAl_y alloy to form Al and

ZrC. As expected, the oxide species in the post-products indicate that the metal fuel is reacting with ambient oxygen. Additionally, X-ray photoelectron spectroscopy can be performed to investigate the presence of potential amorphous species in the post-products, where the most likely amorphous species is Al_2O_3 due to reaction of Al with ambient oxygen. Similarly, the post-products with microwave application reveal the crystalline signatures of the same species. Notably, the ratio of ZrO_2 to oxygen deficient zirconium oxide, ZrO, is higher in the case of microwave application which might be due to reaction continuation in the hotter cooling zone of the combustion wave as demonstrated in Figure 6-4. Nonetheless, XRD analysis demonstrates that the reaction pathways do not significantly change with microwave application and the same crystalline phase post-products are present in the species with and without external microwave stimulus.

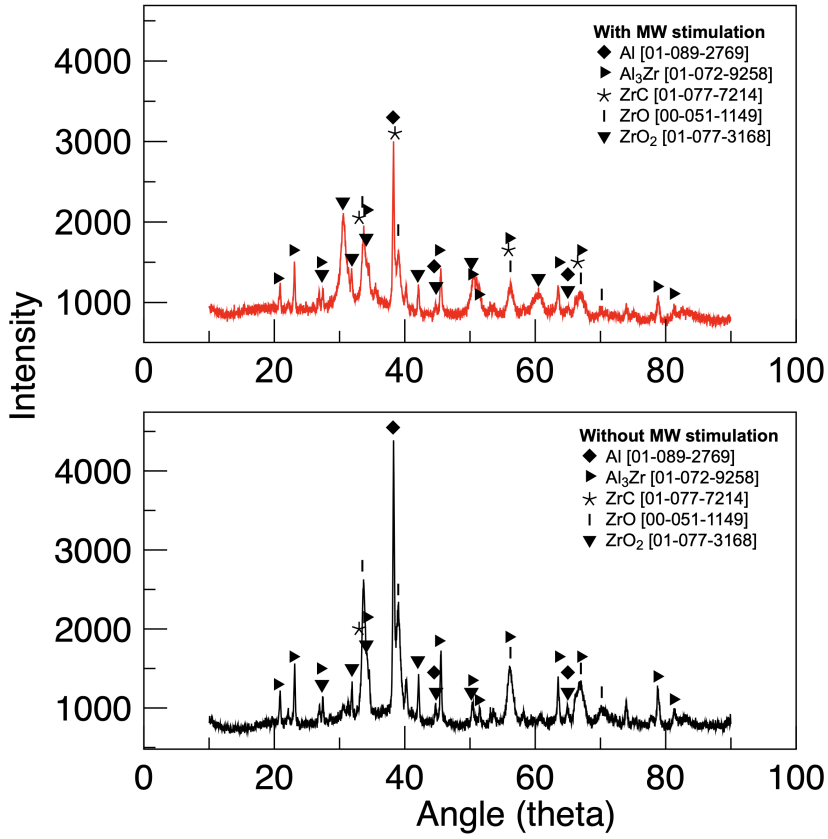

Figure 6-5. *X-ray diffraction patterns of reaction post-products with and without microwave stimulation.*

6.4 Conclusions

In summary, this work builds a pathway towards the controllable, dynamic modulation of solid propellants via microwave energy application. We have demonstrated that energy release rate during combustion of Al-Zr-C can be increased by 204% with microwave energy application and can be tuned to a higher or lower value with a change in applied microwave intensities. The additional energy stimulus negates the effect of conductive heat losses to the product and pre-heat zones, decreasing the thermal gradients

in both zones and increasing their length scales. This work can be further expanded to investigate the effect of on-demand pulsing of the microwave source on the acceleration and waning of the combustion front with applied energy pulses. Additional modeling and numerical analysis can improve our understanding of the intricate effects of microwave hot spots on the heat balance between the reaction enthalpy and heat losses.

6.5 References

[1] S.J. Barkley, K. Zhu, J.E. Lynch, J.B. Michael, T.R. Sippel, Microwave plasma enhancement of multiphase flames: On-demand control of solid propellant burning rate, Combust. Flame. 199 (2019) 14–23. https://doi.org/10.1016/j.combustflame.2018.10.007.

[2] S.J. Barkley, D.K. Kindem, K. Zhu, J.B. Michael, T. Sippel, Dynamic control of composite solid propellant flame spread through microwave eddy current heating of propellant-embedded antennas, AIAA Scitech 2019 Forum. (2019) 1–8. https://doi.org/10.2514/6.2019-1239.

[3] J.F. Crider, Self-Propagating High Temperature Synthesis–-A Soviet Method for Producing Ceramic Materials, (2008) 519–528. https://doi.org/10.1002/9780470318782.ch8.

[4] A.S. Mukasyan, A.S. Rogachev, Discrete reaction waves: Gasless combustion of solid powder mixtures, Prog. Energy Combust. Sci. 34 (2008) 377–416. https://doi.org/10.1016/j.pecs.2007.09.002.

[5] A.G. Merzhanov, The chemistry of self-propagating high-temperature synthesis, (2004) 1779–1786.

[6] M. Lakshmikantha, J.A. Sekhar, Analytical Modeling of the Propagation of a Thermal Reaction Front in Condensed Systems, J. Am. Ceram. Soc. 77 (1994) 202–210. https://doi.org/10.1111/j.1151-2916.1994.tb06978.x.

[7] A.G. Merzhanov, B.I. Khaikin, Theory of combustion waves in homogeneous media, Prog. Energy Combust. Sci. 14 (1988) 1–98. https://doi.org/10.1016/0360-1285(88)90006-8.

[8] A.G. Merzhanov, I.P. Borovinskaya, Historical retrospective of SHS: An autoreview, Int. J. Self-Propagating High-Temperature Synth. 17 (2008) 242–265. https://doi.org/10.3103/s1061386208040079.

[9] V.A. Knyazik, A.G. Merzhanov, V.B. Solomonov, A.S. Shteinberg, Macrokinetics of high-temperature titanium interaction with carbon under electrothermal explosion conditions, Fiz. Goreniya i Vzryva. 21 (1985) 69–73.

[10] A. Feng, Z.A. Munir, The effect of an electric field on self-sustaining combustion synthesis: Part I. modeling studies, Metall. Mater. Trans. B. 26 (1995) 581–586. https://doi.org/10.1007/BF02653878.

[11] A. Makino, Effects of electric field on the SHS flame propagation of the Si-C system, examined by the use of the heterogeneous theory, J. Combust. 2013 (2013)

1–8. https://doi.org/10.1155/2013/752068.

[12] S.Q. Arlington, S.C. Barron, J.B. DeLisio, J.C. Rodriguez, S. Vummidi Lakshman, T.P. Weihs, G.M. Fritz, Multifunctional Reactive Nanocomposites via Direct Ink Writing, Adv. Mater. Technol. 6 (2021) 1–7. https://doi.org/10.1002/admt.202001115.

[13] D.J. Kline, M.C. Rehwoldt, J.B. DeLisio, S.C. Barron, H. Wang, Z. Alibay, J.C. Rodriguez, G.M. Fritz, M.R. Zachariah, In-operando thermophysical properties and kinetics measurements of Al-Zr-C composites, Combust. Flame. 228 (2021) 250–258. https://doi.org/10.1016/j.combustflame.2020.12.045.

[14] R.J. Jacob, D.J. Kline, M.R. Zachariah, High speed 2-dimensional temperature measurements of nanothermite composites: Probing thermal vs. Gas generation effects, J. Appl. Phys. 123 (2018). https://doi.org/10.1063/1.5021890.

[15] A. Porch, D. Slocombe, P.P. Edwards, Microwave absorption in powders of small conducting particles for heating applications, Phys. Chem. Chem. Phys. 15 (2013) 2757–2763. https://doi.org/10.1039/c2cp43310a.

[16] K.I. Rybakov, V.E. Semenov, S. V. Egorov, A.G. Eremeev, I. V. Plotnikov, Y. V. Bykov, Microwave heating of conductive powder materials, J. Appl. Phys. 99 (2006) 023506. https://doi.org/10.1063/1.2159078.

[17] P. Biswas, D.J. Kline, M. Rehwoldt, T. Wu, W. Zhao, X. Wang, M.R. Zachariah, Microwave absorption by small dielectric and semi-conductor coated metal particles, ACS Appl. Polym. Mater. 1 (2019) 982–989. https://doi.org/10.1021/acsapm.9b00016.

[18] P. Biswas, G.W. Mulholland, M.C. Rehwoldt, D.J. Kline, M.R. Zachariah, Microwave absorption by small dielectric and semi-conductor coated metal particles, J. Quant. Spectrosc. Radiat. Transf. 247 (2020) 106938. https://doi.org/10.1016/j.jqsrt.2020.106938.

[19] C.F. Bohren, D.R. Huffman, Absorption and Scattering of Light by Small Particles, 1998. https://doi.org/10.1002/9783527618156.

[20] M. Ballas, H. Song, O.J. Ilegbusi, Effect of thermal conductivity on reaction front propagation during combustion synthesis of intermetalics, J. Mater. Sci. 41 (2006) 4169–4177. https://doi.org/10.1007/s10853-006-6751-0.

7 Summary and Future Work

7.1 Summary

The research findings in this dissertation can categorized into three parts where (I) instrumentation for characterization and stimulation was carefully designed to study the effect of microwave energy excitation on energetic materials, (II) microwave combustion onset mechanisms of reactive nanocomposites were investigated and novel formulations were engineered to control ignition in solid propellants, and (III) the influence of heat transfer mechanisms on the propagation of nanoenergetics were studied and reactive systems with microwave controlled energy release pathways were designed. The efforts presented in this dissertation build a promising path toward safe, consistent and precise energy release of solid propellants by means of electromagnetic stimulation at 2.45 GHz.

Chapter 2 is dedicated to the description of all instrumentation which was used in this dissertation to either ignite, combust, or characterize energetic composites by electromagnetic radiation at 2.45 GHz. The working theory and component design of two critical tools which were designed, built, and routinely calibrated to achieve the research goals outlined in the introduction, the single frequency microwave cavity and the high-power monopole antenna set-up, were described in detail. Additionally, high-speed temperature imaging tools such as infrared thermometry and color ratio pyrometry used to characterize the performance of microwave stimulated energetic materials were also described.

After all relevant ignition and characterization instrumentation was introduced and described, the mechanisms driving microwave ignition of energetic materials were

experimentally studied in Chapter 3. The effect of applied power intensity, susceptor concentration, microwave absorption efficiency, heat losses and reaction kinetics were experimentally and computationally analyzed on a nanoscale, 3D printed titanium/polyvinyledene fluoride (nTi/PVDF) system which was microwave sensitive. It was revealed that two major regimes govern the ignition of nTi/PVDF under microwave stimulation: (I) a power dependent and (II) a power independent regime, where the former changes the time to microwave ignition and heating rates of materials and the latter is limited by the reaction kinetics of nTi ignition.

In chapter 4, research efforts were broadened to explore the engineering of nanothermites with microwave sensitive oxidizing agents. Nanoscale manganese oxide (MnO_x) was studied as a microwave sensitive candidate material for ignition with nanoscale aluminum (nAl). High-speed infrared thermometry demonstrated that direct-ink written MnO_x can be rapidly heated at rates ~10^4 °C/s under EM radiation at 2.45 GHz without addition of inert microwave susceptors. Different loadings of nAl were 3D printed with MnOx to study the effect of susceptor concentration on the microwave heating of nAl based composites. Subsequent, computational modeling based on the dielectric and thermo-physical properties of these materials showed that electric field absorption is responsible for ~96% of the heating of nAl/MnOx and the oxidizer absorbs 99% of the incident radiation and transfers the heat to neighboring Al nanoparticles.

In chapter 5, the influence of heat transfer mechanisms such as radiation, conduction, convection, metal vapor condensation and particle advection on the combustion of nAl/I_2O_5 propellants was investigated via microscopic high-speed color

camera imaging. Experimental measurements on temperature, particle advection speed, and macroscopic burn rate of the 3D printed nanocomposites made it possible to estimate the contribution of each heat transfer mechanism on nAl/I_2O_5 combustion performance, where it was found that the propellant combustion under constant pressure cannot be sustained due to insufficient energy contributions from these mechanisms. However, the energy deficit was overcome by supplementing nanoscale CuO at small mass fractions (<25 wt.%) in nAl/I_2O_5 composites, where CuO provided a surplus of energy via metal vapor condensation. The results demonstrated that the reliability of solid propellant combustion can be enhanced by simple estimates of the heat transfer mechanisms and corresponding fractional changes to the formulations.

To explore alternative methods to control the combustion performance of energetic materials beyond fabrication techniques, the effect of microwave stimulation on propagating composites was studied in Chapter 6. The experimental results showed that by the simple tunning of microwave power intensity, the energy release rate of Al-Zr-C composites can be increased or decreased by up to 204%. The additional energy stimulus negates the effect of conductive heat losses to the product and pre-heat zones, decreasing the thermal gradients in both zones and increasing their length scales.

The findings in this dissertation can be further expanded into the following three proposed projects.

7.2 Recommendations For Future Work

7.2.1 Tuning Reactivity and Ignition of Energetic Materials via Oxidizer Morphology: From Nanowires To Spheres

Previous studies have shown that particles with high aspect ratios can easily form percolating networks that can assist heat transfer during combustion and thus enhance energy release rates of energetic materials. Concurrently, it has been shown that MnO_2 nanowires are microwave susceptible and can potentially absorb more incident microwave radiation due to their high-aspect ratio morphology. Chapter 4 demonstrated that spherical MnO_2/Mn_2O_3 nanoparticles can drive and control ignition of nAl under microwave stimulation. In future work, composites which consist of constituents possessing properties that enable more efficient heat transfer and microwave susceptibility should be investigated to design innovating microwave sensitive energetic systems.

7.2.2 Microwave Ignition Modulation via Ammonium Perchlorate Addition

Ammonium perchlorate (AP) is a powerful gas producing oxidizer that is often used with hydroxyl-terminated polybutadiene (HTPB) fuel binder for high energy combustion applications or as an additive to reduce reactive sintering effects when studied in nAl-based thermites. By itself, AP can decompose exothermically to produce perchlorate gas. Various catalysts were studied to facilitate exothermic decomposition of AP, where interestingly, MnO2 was shown to decrease the temperature onset for AP decomposition. The addition of a powerful gas generating oxidizer such as AP can enhance the energetic performance

of nAl/MnOx thermites. In future work, the triple effect of MnOx as catalyst, oxidizer and microwave sensitizer should be investigated using the designed microwave cavity set up described in Chapter 2 of this dissertation.

7.2.3 On Demand Microwave Augmentation of Combustion at Millisecond Scale

Stimulation via microwave energy also provides the capability of pulsing the outgoing electromagnetic signal. Millisecond scale-controlled changes to microwave pulse can enable future investigations on the effect of on/off energy deposition to the combusting wave front. Future work should investigate the time required for various SHS reactant's flame front to equilibrate or get disturbed by localized microwave energy. Efforts along this path could shed light on the working mechanisms on the wave front acceleration and deceleration via applied pulsed microwave energy.